NASA Contractor Report 185252

An Investigation into the Numerical Prediction of Boundary Layer Transition Using the K.Y. Chien Turbulence Model

Craig A. Stephens and Michael E. Crawford
The University of Texas at Austin
Austin, Texas

June 1990

Prepared for
Lewis Research Center
Under Grant NAG3-864

National Aeronautics and
Space Administration

Table of Contents

Nomenclature

English Letter Symbols

A = empirical model constant for Schmidt's PTM transition model

B = empirical model constant for Schmidt's PTM transition model

c = specific heat at constant pressure

c_j = work - energy conversion constant

Cf = local friction coefficient, $\tau_w / (\rho_e U_e^2)$

C_J = work - energy conversion constant

C_μ = empirical constant for turbulent viscosity calculation

C_1 = empirical constant for TDR transport equation

C_2 = empirical constant for TDR transport equation

D = low-Reynolds number term for TKE equation

E = low-Reynolds number term for TDR equation

f_μ = damping function used in turbulent viscosity calculation

f_1 = damping function for TDR transport equation

f_2 = damping function for TDR transport equation

g_c = force - mass conversion constant

$\hat{I}^*$ = instantaneous stagnation enthalpy

I^* = mean stagnation enthalpy

$i^{*\prime}$ = fluctuating stagnation enthalpy

k = turbulent kinetic energy (TKE), $0.5\left(\overline{u'^2}+\overline{v'^2}+\overline{w'^2}\right)$, or laminar (molecular) thermal conductivity

k^+ = nondimensional turbulent kinetic energy, k/u_τ^2

k_t = turbulent thermal conductivity

P = thermodynamic pressure

Pr = Prandtl number

Pr_t = turbulent Prandtl number

Pr_{eff} = effective Prandtl number, see Eq. (2.33)

$\hat{q}$ = molecular heat flux

q'' = molecular heat flux per unit area

Re_m = momentum Reynolds number, $U_e\delta_2/\nu$

Re_t = turbulent Reynolds number, $k^2/(\nu\hat{\varepsilon})$

Re_x = x-Reynolds number, $U_e x/\nu$

Re_τ = local Reynolds number, $(u_\tau y)/\nu = y^+$

s = turbine blade wetted surface distance

St = Stanton number, $h/(U_e\rho c)$

S_k = Summation of the TKE equation source terms, see Eq. (4.8)

S_ε = Summation of the TDR equation source terms, see Eq. (4.9)

S_k^+ = Nondimensional S_k, $S_k\nu/u_\tau^4$

S_ε^+ = Nondimensional S_ε, $S_\varepsilon\nu^2/u_\tau^6$

T = temperature

Tu = turbulence intensity, $1/U_e\left(1/3\left(\overline{u'u'} + \overline{v'v'} + \overline{w'w'}\right)\right)^{0.5}$

$\tilde{U}$ = instantaneous streamwise velocity component (x-direction)

U = mean streamwise velocity component (x-direction)

u' = fluctuating streamwise velocity component (x-direction)

u_τ = shear velocity, $[(g_c\tau_w)/\rho_w]^{0.5}$

$\tilde{V}$ = instantaneous cross-stream velocity component (y-direction)

V = mean cross-stream velocity component (y-direction)

v' = fluctuating cross-stream velocity component (y-direction)

x = streamwise coordinate

y = cross-stream coordinate

y^+ = nondimensional y-distance from a wall for turbulent shear layers

Greek Letter Symbols

α = molecular thermal diffusivity, or empirical model constant for The University of Texas transition model

β = empirical model constant for The University of Texas transition model

Δ = thickness of thermal boundary layer

δ = thickness of momentum boundary layer

δ_2 = momentum thickness of the boundary layer

δ_{ki} = kronecker delta

ε = nonisotropic turbulent dissipation rate, $-\mu\overline{S_{ij}S_{ij}}$

$\hat{\varepsilon}$ = isotropic turbulent dissipation rate (TDR), $-\mu\overline{\partial_y u \partial_y u}$

ε_H = eddy diffusivity for heat transfer

ε_M = eddy diffusivity for momentum

ε^+ = nondimensional turbulent dissipation rate, $\varepsilon\nu/u_\tau^4$

μ = dynamic viscosity

μ_t = turbulent viscosity

μ_{eff} = effective viscosity, $\mu + \mu_t$

ν = kinematic viscosity

ν_t = turbulent viscosity, μ_t / ρ

ρ = fluid density

σ_ε = empirical constant for the TDR transport equation

σ_k = empirical constant for the TKE transport equation

σ_{ki} = stress tensor

Subscripts

C = critical value

e = freestream location

E = end of transition

f = far-field location

S = start of transition

w = wall location

Chapter 1

Literature Review

1.0 Introduction

Gas turbine engine design has changed drastically in recent years in the quest to improve engine efficiency and increase power output levels. The development of a more efficient gas turbine is directly linked to an increase in the turbine inlet temperature. As the gas turbine inlet temperature rises, so does the turbine efficiency and power output. However, there is a penalty for increasing the inlet temperature, namely the ability to protect the turbine blades from the high temperature environment. This issue becomes an important design consideration.

Accurate prediction of the gas side heat transfer between the hot mainstream gases and the turbine blade surface has proved to be difficult and unreliable. Prediction of the developing boundary layer from the blade stagnation point, to a developing laminar boundary layer, through transition, and finally to a fully turbulent boundary layer is integral to predicting the blade heat transfer. High heating rates on a gas turbine blade occur in the stagnation region and at the end of the transition region. Since engineers design the shape of turbine blades and the resulting stagnation point location, the thermal protection required in this region can be assessed. On the other hand, the complex nature of the transition process and the failure of mathematical models to simulate this process often leads to an over-design of the thermal protection needed by the turbine blade.

The original objective of this thesis was to assess two transition models using a two-dimensional boundary layer code, TEXSTAN. In particular, the research was to focus on transition models developed at the University of Minnesota and The University of Texas at Austin as applied to the K. Y. Chien [1982] two-

equation turbulence model to assess their transition simulation capabilities. This research also focuses on the initial and boundary condition characteristics required to accurately simulate transition. The results of this research have led to identification of a major shortcoming in the use of the basic K. Y. Chien turbulence model for low-Reynolds number flows.

1.1 Gas Turbine Environment and Numerical Simulation Difficulties

This section is an overview of the environmental conditions modeled by numerical simulations that calculate the heat transfer distribution on turbine blades. The quest for improved turbine efficiency has pushed the turbine inlet temperatures past the melting point of turbine blade materials, resulting in a need to design adequate blade cooling systems based on accurate turbine blade heat transfer distributions. The building of experimental turbine blades to measure heat transfer distributions has become so costly and time consuming that a need for accurate numerical modeling of turbine blade heat transfer has become a must. With improvements in numerical schemes and computational ability, the need for experimental measurements will decrease; however, current agreement between experimental and numerical heat transfer predictions on turbine blades has not been consistent, especially in the transition region of the blades.

Figure 1.1 shows a schematic of the basic components for a propulsion gas turbine engine. Air enters the gas turbine and is compressed by an axial flow compressor, which increases the air pressure. At the end of this process, the air enters a combustion chamber where fuel is injected and burned at essentially constant pressure. The products of combustion are then diluted to control the gas temperature and then expanded through a turbine. Here change in the axial momentum of the combustion gases is converted to a torque on the turbine rotor, hence the fluid work is extracted through the rotor to drive the compressor. Turbine inlet gas tem-

peratures from the combustion chamber are typically on the order of 2500°F (1370°C) and at a pressure of 15 - 25 atmospheres. The combustion gases are in a highly turbulent state with the turbulence levels being in the range of 10% to 20% or more.

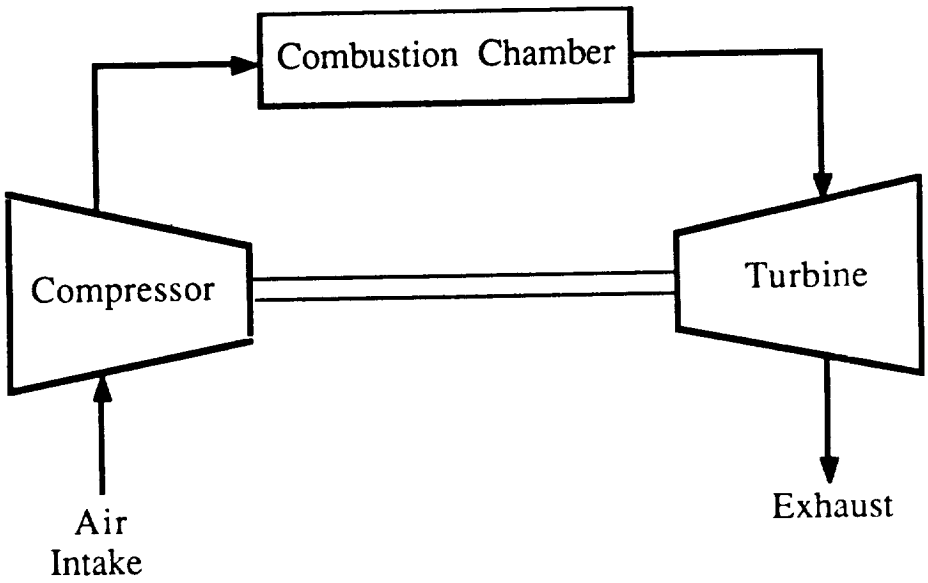

Figure 1.1. Schematic of a gas turbine engine.

The turbine section consists of one or more stages, each containing a row of stationary turbine blades, called stators or nozzle guide vanes, and a row of rotating blades, called buckets or rotor blades. Figure 1.2 shows a typical turbine blade. The upper and lower contour of a turbine blade are different; therefore, the flow characteristics around each side of a turbine blade are different. The upper surface of a turbine blade is typically called the "suction" or "convex" surface, because of the higher flow acceleration and resulting lower pressure distribution. The lower surface of a turbine blade is typically called the "pressure" or "concave" surface, because of the lower flow acceleration and resulting higher pressure distribution. The incoming flow from the combustion chamber is guided by the first-stage stator to the rotor blades where the flow around the rotor blades produces a torque about the rotor shaft. On each blade there exists a stagnation point where a line drawn

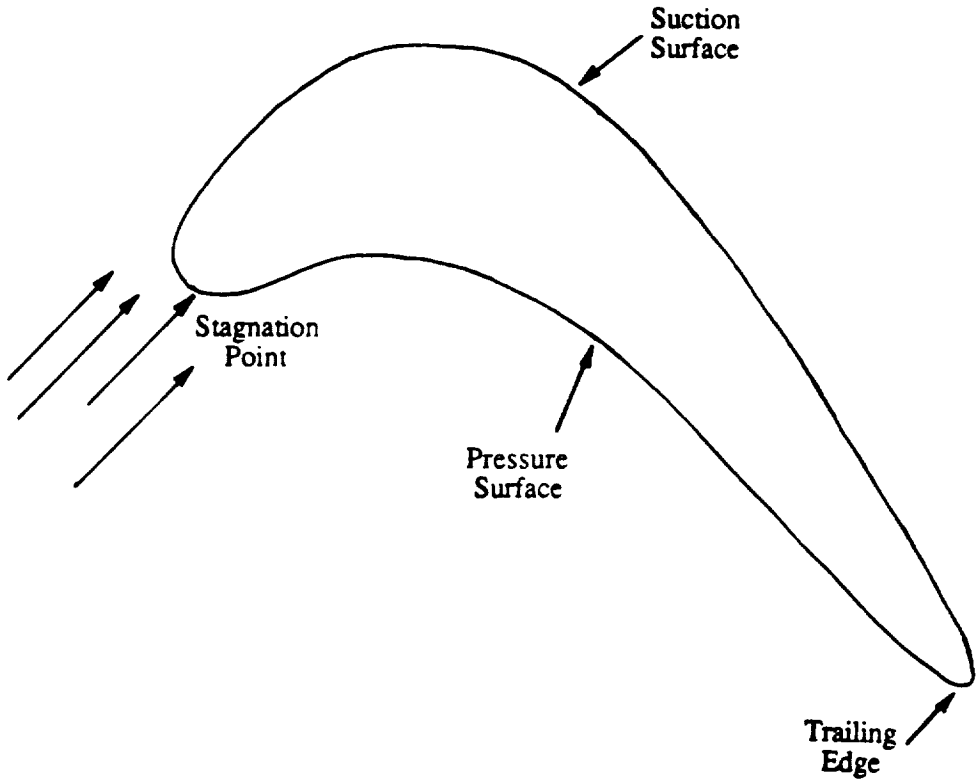

Figure 1.2. Turbine blade nomenclature.

normal to the surface is exactly parallel to the approaching flow. It is from the stagnation point where the thin viscous region, known as the boundary layer, develops and grows over the pressure and suction surfaces. Outside the boundary layer the flow field is considered irrotational and thus inviscid.

The flow field over a turbine blade is complex and three-dimensional in nature. However, the three-dimensional effects may be considered secondary in the midspan region if the blade aspect ratio is not too small. A blade aspect ratio is the ratio of the blade length to the midspan chord and is a measure of the influence endwall and/or tip effects may have on the midspan region. Endwall heat transfer on turbine blades is strongly three-dimensional and not amenable to a two-dimensional numerical simulation. However, with a large aspect ratio, the flow field may be considered two-dimensional over the midspan of the blade.

Boundary layer development on a typical turbine blade is influenced by many mechanisms, and their effects on turbine heat transfer distribution are often not fully understood. Some of the mechanisms which influence boundary layer development include:

(1) laminar, transitional, and turbulent flows
(2) high freestream turbulence
(3) effects of adverse and favorable pressure gradients
(4) stagnation flow with freestream turbulence
(5) curvature effects
(6) body force effects due to blade rotation
(7) variable property effects
(8) surface roughness
(9) endwall effects
(10) flow unsteadiness and periodicity

Extensive research is currently being conducted to determine the role each of the above influences plays in the development of the turbine blade boundary layer. Typical two-dimensional boundary layer computer codes can incorporate models to account for a number of the boundary layer influences listed above. However, despite additional models, acceptable accuracy in boundary layer predictions has not been attained. Discussions by Graham [1979] and Hylton et al. [1983] offer further review of the above influences affecting turbine blade boundary layer development. Tani [1969] provides a discussion on the factors that influence transition.

1.2 Overview of Turbulence Modeling

The purpose of this section is to acquaint the reader to the different methods of numerically modeling turbulent flow. The modeling of transition requires a numerical code to have the capability of modeling both laminar and fully turbulent boundary layer development. The numerical prediction of laminar boundary layer characteristics without disturbances is well documented and is relatively easy to verify. On the other hand, numerical schemes to predict fully turbulent boundary layer characteristics are numerous and the prediction capability of each method is subject to debate. This brief overview of the various turbulence models will help explain the theory behind two-equation turbulence models, which are used in this thesis.

There are a variety of turbulence models with an increase in computational effort and complexity associated with the more general models. Rodi [1982] provides an excellent overview on the different aspects of the various turbulence models. Other reviews of turbulence modeling include Hirata et al. [1982] and Lakshminarayana [1986]. Turbulence models are so abundant that many of them have not been adequately tested against experimental data to determine under which

flow conditions the models may not be accurate. Turbulence models are generally classified as follows according to increasing complexity,

(1) Zero-equation model (e.g. mixing length model or algebraic model)
(2) One-equation model (e.g. the k model)
(3) Two-equation model (e.g. the k-ε model)
(4) Full Reynolds stress (FRS) model
(5) Algebraic Reynolds stress (ARS) model
(6) Large eddy simulation (LES) model
(7) Direct simulation

Despite the advances of directly solving the time-dependent full Navier-Stokes equations or solving the equations using a LES model, the only economically feasible way to solve high Reynolds number turbulent flow problems with complex geometry is the use of statistically averaged equations governing the mean-flow quantities [Rodi, 1982].

The governing equations describing the turbulent boundary layer are presented in Chapter 2, but for discussion purposes the basic numerical approach for most turbulent boundary layer computer codes is to solve the time-averaged governing equations. When the two-dimensional instantaneous x-momentum boundary layer equation is time-averaged, two new convective terms arise, $\rho\overline{u'u'}$ and $\rho\overline{u'v'}$. These are called turbulent Reynolds stresses. The first term, a normal Reynolds stress, is either considered negligible or lumped with the pressure gradient. The second term, appearing as a y-gradient, is moved from the convective side of the equation to the diffusive side where it adds to the viscous shear stress. The presence of the turbulent Reynolds stress is an additional unknown leading to the turbulence closure problem. A turbulence model is needed to describe the Reynolds stress before the boundary layer equations may be solved.

The Boussinesq [1877] assumption is traditionally used to relate the turbulent stresses to the mean velocity gradient through the use of a turbulent viscosity, called mean field closure (MFC),

$$-\overline{u'v'} = \nu_t \frac{\partial U}{\partial y}, \tag{1.1}$$

where the proportionality constant, ν_t, is called the turbulent viscosity. The turbulent viscosity is not a fluid property, but depends on the turbulence in the flow and hence is a function of position and upstream history of the flow development. It is apparent from equation (1.1) that the closure problem reduces to describing the turbulence viscosity.

The oldest and simplest MFC model was developed by Prandtl [1925] and termed a zero-equation turbulence model. Prandtl proposed that the turbulent viscosity distribution may be calculated by relating ν_t to the local mean velocity gradient

$$\nu_t = l_m^2 \left| \frac{\partial U}{\partial y} \right|, \tag{1.2}$$

where l_m is the mixing length. Prandtl reasoned that in the near-wall region the only significant length dimension is the distance from the wall, and thus it is reasonable to assume l_m is proportional to y. However, very near a wall, l_m changes in a non-linear manner, and far away from the wall, l_m becomes independent of y.

One popular model for describing l_m is the Van Driest model described in Kays and Crawford [1980]. The Van Driest model describes the single unknown parameter, l_m, over the flow field by the following empirical formulas,

$$l_m = \kappa y \left(1 - \exp\left(- \frac{y^+}{A^+} \right) \right) \qquad \text{for } 0.0 < y^+ \leq \frac{\lambda \delta}{\kappa} \tag{1.3}$$

and

$$l_m = \lambda\delta \qquad \text{for } y^+ > \frac{\lambda\delta}{\kappa}, \tag{1.4}$$

where κ is the Von Karman constant equal to 0.41, A^+ is the Van Driest damping function equal to 25.0 for zero pressure gradients, λ is the outer layer constant equal to 0.085, and δ is the boundary layer thickness. There exists a large amount of experimental data gathered which may be used to empirically obtain l_m.

For all its simplicity, the zero-equation turbulence model has some disadvantages. First, the zero-equation model assumes the flow is in local equilibrium, that is, at each point in the flow the turbulent energy is dissipated at the same rate it is produced. As a result, there cannot be any influence of turbulence production on other parts of the flow or at earlier times. This means the zero-equation model cannot account for the transport and history effects of turbulence. The second problem of zero-equation models is that buoyancy, rotation, or streamline curvature effects must be defined by a mixing length distribution, other than specified by equations (1.3) and (1.4), which are often difficult to develop. This applies equally to complex turbulent flows. Even with these limitations, the zero-equation turbulence model is used quite often to approximate a turbulent flow field.

To obtain more general turbulence models that account for history and transport effects, higher-order turbulence models were developed, such as one- and two-equation models. These higher order turbulence models solve additional transport equations for turbulence quantities. The additional transport equations all adhere to the same basic form linking convection of the quantity under consideration to laminar and turbulent diffusion and to the positive and negative source of the quantities.

$$\text{Convection} = \text{Diffusion} + \text{Sources}. \tag{1.5}$$

These additional turbulence quantities are used to improve the prediction of the turbulent viscosity.

The one-equation turbulence model attempts to incorporate the history and transport effects of turbulence. From a dimensional point of view, the turbulent viscosity may be thought of as a combination of a turbulent velocity scale, V_t, characteristic of the fluctuating velocities, and a turbulent length scale, L_t, characteristic of large turbulent eddies

$$\nu_t \propto V_t L_t . \tag{1.6}$$

The one-equation model uses a transport equation to model the velocity scale of the turbulent motion. The velocity scale is defined as $\sqrt{k}$, where k is the kinetic energy of the turbulent motion and is a measure of the intensity of the three-dimensional turbulent fluctuations. The governing equation for k describes the transport of k in a turbulent flow. Utilizing tensor notation with repeated indicies indicating summation, the governing equation for k is written in the form of equation (1.5) as follows

$$\underset{\text{I}}{\frac{Dk}{Dt}} = \underset{\text{II}}{\frac{\partial}{\partial x_i}\left(\frac{\nu_t}{\sigma_k}\frac{\partial k}{\partial x_i}\right)} \underset{\text{III}}{- \overline{u_i u_j}\frac{\partial U_i}{\partial x_j}} \underset{\text{IV}}{- \varepsilon} , \tag{1.7}$$

where I is the convection of k; II is the diffusion of k; III is the production of k, P_k, which represents a positive source term; and IV is the dissipation of k, which represents a negative source term. The rate coefficient (ν_t / σ_k) represents the turbulent diffusion coefficient for the diffusion of k.

In this one-equation model, the turbulent dissipation rate is a measure of the destruction of k and must be specified. The turbulent dissipation rate is defined by dimensional considerations that link it to a turbulence length scale, L

$$\varepsilon = C_D \frac{k^{1.5}}{L}, \tag{1.8}$$

where C_D is an empirical constant of proportionality for high-Reynolds number turbulence. The turbulent viscosity for a one-equation model is then defined following equation (1.6) as

$$\nu_t = C_\mu' \sqrt{k}\, L, \tag{1.9}$$

where C_μ' is the empirical constant of proportionality for high-Reynolds number turbulence. Specification of the turbulent length scale is similar to the mixing length scale defined in equations (1.3) and (1.4). An empirical specification of L works well for simple shear layers as demonstrated by work in Bradshaw et al. [1967] and by Hassid and Poreh [1975].

As with the zero-equation turbulence model, the one-equation turbulence model also has some disadvantages. For complex turbulent shear flows the specification of an empirical function for L is no easier to specify than it is for the mixing length, l_m. The governing transport equation for k (equation 1.7) and the empirical constants, C_D and C_μ', were developed for high-Reynolds number flows where the ratio of ν_t to ν is large. Therefore, in the near-wall region where the local turbulent Reynolds number is low, the constants of the model become functionals. Low-Reynolds number one-equation models have been developed and work well for zero and adverse pressure gradient flows, but generally have problems with strongly accelerated boundary layers. Besides the turbulent velocity scale, the turbulent length scale is also subject to history and transport effects which are not accounted for by the one-equation turbulence model. Due to the aforementioned problems, the recent trend has been to use two-equation turbulence models that calculate a length scale from another turbulent transport equation.

The two-equation turbulence model utilizes transport equations for the velocity and length or time scales of turbulent motion to account for history and transport effects of turbulence. A popular two-equation model is the k-ε turbulence model, in which the length scale is constructed from a combination of k and ε. The turbulent length scale for k-ε models is defined by dimensional considerations as

$$L = \frac{k^{1.5}}{\varepsilon}. \tag{1.10}$$

This length scale is used in conjunction with equation (1.6) to calculate the turbulent viscosity at any point in the boundary layer. Thus the second differential transport equation is that for ε.

Other classes of two-equation models exist in which the second variable is fluctuating vorticity (often termed k-ω^2 turbulence models) or some other turbulence variable. The ability to relate the turbulent dissipation rate to vorticity is not discussed in this section, but examples of k-ω^2 models include Saffman [1970], Saffman and Wilcox [1974], Wilcox and Traci [1976], and Wilcox and Rubesin [1980].

A two-equation k-ε model uses equation (1.7) to calculate the velocity scale of the boundary layer. The dissipation, ε, is calculated using a differential transport equation defined as

$$\underset{\text{I}}{\frac{D\varepsilon}{Dt}} = \underset{\text{II}}{\frac{\partial}{\partial x_i}\left(\frac{\nu_t}{\sigma_\varepsilon}\frac{\partial \varepsilon}{\partial x_i}\right)} + \underset{\text{III}}{C_1 \frac{\varepsilon}{k} P_k} - \underset{\text{IV}}{C_2 \frac{\varepsilon^2}{k}}, \tag{1.11}$$

where I is the convection of ε; II is the diffusion of ε; III is the production of ε, which represents a positive source term; and IV is the dissipation of ε, which represents a negative source term. The rate coefficient ($\nu_t / \sigma_\varepsilon$) represents the turbulent

diffusion coefficient for the diffusion of ε, while C_1 and C_2 are turbulent model constants.

The terms in equation (1.11) are similar to the terms of equation (1.7). Equations (1.7) and (1.11) constitute the high-Reynolds number (HRN) form of the two-equation models and thus require the use of wall functions to calculate through the buffer and viscous sublayers in the near-wall region. Jones and Launder [1972, 1973] proposed a low-Reynolds number (LRN) form of k-ε turbulence model that allowed continuous numerical calculations from the freestream down to the wall. The Jones and Launder LRN two-equation turbulence model has additional terms on the right-hand side of equations (1.7) and (1.11) to allow the ε wall boundary condition to be set to zero and to improve the match between the numerical peak level of turbulent kinetic energy and experiment. Since Jones and Launder's original proposal, a large variety of LRN two-equation turbulence models have been presented in the open literature. Examples of the different LRN two-equation models include Launder and Sharma [1974], Reynolds [1976], Lam and Bremhorst [1981], K. Y. Chien [1982], and Nagano and Hishida [1987]. In an attempt to evaluate the performance of several two-equation models, Patel et al. [1985] systematically examined eight two-equation models for their prediction capability over a variety of flows. They concluded that the two-equation models of Launder and Sharma [1974], K. Y. Chien [1982], Lam and Bremhorst [1981], and Wilcox and Rubesin [1980] performed better than the other models for the turbulent flows considered.

One limitation to the k-ε turbulence model is the assumption that the turbulent viscosity is isotropic, implying the Reynolds stresses are uniform in all directions. Relating the Reynolds stresses to one velocity scale and length scale for all directions is a weakness of the two-equation model. In complex turbulent shear flows, the individual Reynolds stresses develop quite differently depending on the location in the flow. The turbulence models discussed so far can not account for the nonisotropic nature of Reynolds stresses. To account for the different devel-

opment of each Reynolds stress, a transport equation for each component of the Reynolds stress tensor may be formulated. This is the foundation for a Reynolds stress turbulence model.

In general, there are six components of Reynolds stress, defined in tensor notation as $\rho\overline{u_i'u_j'}$. Turbulence models that solve transport equations for each component of the Reynolds stress tensor without approximations are called full Reynolds stress (FRS) models or second-moment closure schemes. The transport equation for each Reynolds stress component in tensor notation [Markatos, 1987] may be written as

$$\frac{D\overline{u_iu_j}}{Dt} = P_{ij} + \Pi_{ij} + D_{ij} - \varepsilon_{ij}\,, \tag{1.12}$$

where P_{ij} is the Reynolds stress production tensor; Π_{ij} is the pressure strain "redistribution tensor;" D_{ij} is the diffusion tensor; and ε_{ij} is the viscous dissipation tensor. Launder [1984] provides a very detailed derivation for equation (1.12) and the use of FRS models in general. In using a FRS model, a constitutive equation for calculating the turbulent Reynolds stresses is not required because the Reynolds stresses are directly solved by the set of equations similar to equation (1.12). One difficulty in using a FRS model is the lack of information concerning the functional forms of the various terms of equation (1.12). This lack of information is prevalent in the near-wall region, the boundary conditions, and the initial profiles for each Reynolds stress component. FRS models are rather complex and computationally expensive, therefore they are not well suited for practical applications.

The solution to each Reynolds stress transport equation is not easy and requires considerable computer time and expense. However, it would be desirable to simplify the Reynolds stress equations as much as possible for computation capability, but still retain accurate predictions. For this reason, the algebraic Reynolds stress (ARS) model was developed to reduce the differential transport equations for Reynolds stress into algebraic expressions that still retain the characteristics of the

differential terms. The convection and diffusion terms make the transport equations differential equations, hence when these terms are eliminated by model approximations, the differential equations can be converted into algebraic expressions. Rodi [1976] proposed the transport of $\overline{u_i'u_j'}$ as proportional to the transport of k with the proportionality factor being the ratio $\overline{u_i'u_j'}/k$, which is not considered a constant. By assuming $\overline{u_i'u_j'}$ proportional to k, the source terms of the Reynolds stress transport equations become proportional to the source terms of the k-equation. The actual ARS model equation and a detailed discussion on ARS modeling are presented by Rodi [1980] and Lakshminarayana [1986]. Since k and ε appear in the ARS model equations, a k-ε turbulence model must be solved in order to complete the model. It may be considered that the algebraic expressions of the ARS model coupled with the k and ε equations form an extended k-ε model. ARS models simulate the turbulent stresses more realistically because the isotropic stress assumption, associated with two-equation models, has been eliminated and each Reynolds stress may be calculated based on the local conditions. The ARS model is computationally inexpensive and can directly account for the effects of buoyancy, rotation, streamline curvature, nonisotropic strain fields, and wall-damping influences directly instead of through modeling.

One type of turbulence model that has just recently begun to produce significant results are large-eddy simulation (LES) models. These models solve the three-dimensional time-dependent full Navier-Stokes equations for the large-scale turbulence, but use models for the smallest scales, which are difficult to compute at high turbulent Reynolds numbers. In general, higher-order statistical properties, such as Reynolds stress and turbulent heat flux, take longer to numerically reach steady state than lower order terms, such as k and ε. The LES model truncates time-dependent computations at small scales, to ensure a converged solution, and models the smaller scales based on the fact that smaller scales adjust faster to changes in local conditions. Recent work with LES models has been able to simulate the main features of turbulent flow experiments.

The final turbulence prediction method considered is direct simulation. This technique involves the direct solution of the time-dependent full Navier-Stokes equations without the use of any models. Since supercomputers have recently become available, direct simulation has begun to make contributions to predicting some flows, but still requires tremendous computational efforts. The simulation capability is restricted to low-Reynolds number flows because for fully developed high-Reynolds number turbulent flow the range of eddy sizes, i.e. scales, is too great to be calculated on any computer.

1.3 Overview of Numerical Transition Studies

This section outlines various numerical transition studies from the open literature that report prediction of heat transfer and friction distributions for various geometries. The use of zero-equation and one-equation turbulence models to simulate transition is briefly outlined. However, the major emphasis is on the use of the two-equation turbulence model to predict boundary layer transition.

One of the first investigations into describing the onset of transition was conducted by Emmons [1953]. While observing flow in a water-table, Emmons noted the creation of tiny spots of turbulent flow emanating from point sources in an otherwise laminar boundary layer. The turbulent spots grew as they were swept downstream and eventually coalesced into a fully turbulent boundary layer. From these observations, Emmons proposed that transitions from laminar to turbulent flow occur through the creation, growth, and coalescence of turbulent spots. Therefore, at any location downstream of a point source the flow will be intermittently turbulent; that is, the location will be laminar except during the time which a turbulent spot is convected over it. Emmons analytically described transition as a random phenomena, which can be described by a probability function specifying the fraction of time that the flow at each point is turbulent. This probability func-

tion is called the intermittency factor, γ, which represents the fraction of time any point spends in turbulent flow. Riley and Gad-el-Hak [1985] have compiled an outline of the present knowledge of turbulent spots including detailed flow-visualization.

Dhawan and Narasimha [1958] developed an expression for a universal intermittency distribution for transitional flow based on Emmons' work. Several transition models, called intermittency models, have been developed from Dhawan and Narasimha's universal intermittency expression. Basically, an intermittency model modifies the magnitude of the turbulent viscosity (i.e. $\mu_{eff} = \mu + \gamma\mu_t$) from a fully laminar flow ($\gamma = 0$) to a fully turbulent flow ($\gamma = 1$). By modifying the turbulent viscosity, the intermittency model controls the path of the transition process. To use an intermittency model other empirical correlations must be used to estimate the starting location of transition and the length of the transition region. Intermittency models have been used with zero-equation to two-equation turbulence models in an attempt to simulate transition; however, the resulting predictions are only as accurate as the correlations for the start and end of transition and the ability of the intermittency function to describe the path of transition.

McDonald and Fish [1973] used a one-equation turbulence model to investigate the effects of surface roughness and freestream turbulence on the location and extent of transition from a laminar to fully turbulent boundary layer. A damping function was used to control the growth of the mixing length in the viscous sublayer, which in turn controlled transition. McDonald and Fish obtained excellent numerical comparison of the heat transfer distribution with experimental data for flat plate flow with zero pressure gradient. Their comparison of numerical heat transfer distributions for a turbine airfoil were reasonable given the limited experimental information for their model development.

The goal of Forest [1977] was to develop a numerical procedure for design purposes to predict transitional boundary layers occurring on turbomachinery

blades. Because of the simplicity and low computational time, Forest used the Patankar and Spalding [1970] numerical code with an intermittency model coupled with a zero-equation turbulence model. His numerical predictions for the shape factor, momentum thickness, and heat transfer distributions were in good agreement with experimental flat plate zero pressure gradient data. In calculating the heat transfer distribution for a relaminarization boundary layer, Forest noted a lag in his numerical calculations when compared to experimental data. The comparison of the heat transfer distributions for a turbine cascade was reasonable. On the suction surface the overall predictions were good but lacking in the transition region. On the pressure surface the competing effects of the high freestream turbulence (promoting transition) and high acceleration (delaying transition) produced long regions of transitional flow which resulted in poor heat transfer predictions.

The goal of Hylton et al. [1983] was to asses the capability of available modeling techniques to predict turbine airfoil heat transfer by acquiring experimental data for numerical comparisons and improve the numerical techniques. They used three sets of open literature data to determine which numerical model they would focus on for improvements. The boundary layer models investigated were an integral method, a finite-difference method with a zero-equation model [Crawford and Kays, 1976], and the same finite-difference method with a Jones and Launder [1973] two-equation model. The transition model for the integral method consisted of an instantaneous transition from laminar to turbulent flow at a critical momentum Reynolds number. Both finite-difference models used an intermittency model to simulate transition. Based on comparison with open literature turbine data, the finite-difference model with the zero-equation turbulence model was selected for further study. Hylton et al. cited the transition models as the weak element in the overall modeling of turbine blade heat transfer; the simple intermittency models led to poor predictions. Hylton et al. conducted a thorough investigation into the calculation ability of several transition start models, transition length models, transition path models, and zero-equation turbulent viscosity models to simulate heat transfer distributions. They concluded that the available intermittency

models lead to generally poor predictions on both the suction and pressure surfaces. The principal failure of these models was that the numerical transition completed more rapidly than experimental measurements indicated. As a result, Hylton et al. developed a zero-equation turbulence model that modified the turbulent viscosity based on the freestream turbulence level. The resulting transition calculations were based on the "natural transition" capability of the zero-equation model. The researchers also proposed a methodology for calculating good initial profiles and boundary conditions in order to enhance accurate heat transfer results.

Other investigations into the use of zero-equation turbulence models coupled with an intermittency model to numerically predict turbine blade heat transfer distributions include the work of Roberts and Brown [1984] and Gaugler [1985]. Park and Simon [1987] is an excellent reference for the use of zero-equation models to predict transitional boundary layer heat transfer. The relative success of zero- and one-equation turbulence models to simulate transition has created interest in determining the ability of higher order turbulence models to predict transition.

Launder and Spalding [1974] were among the first researchers to publish work related to the use of k-ε turbulence models to simulate transition. Launder and Spalding published the numerical transition predictions of Priddin [1975] for the gas turbine blade data of Turner [1971]. Priddin is credited with demonstrating the ability of the k-ε numerical procedure to simulate transition of external boundary layers. Launder and Spalding noted the effect of high freestream turbulence on turbine blade transition predictions. For high freestream turbulence intensities, i.e. Tu, (Tu ~ 6.0%), the blade was nearly completely turbulent. For intermediate turbulence levels (Tu ~ 2.0%), the blade was laminar until the 40% chord location, then became turbulent. At low turbulence levels (Tu < 0.4%), the blade remained laminar. Priddin did not use a transition model; therefore, Launder and Spalding believed the low-Reynolds number k-ε turbulence models have their own built in "transition criteria." Priddin's numerical calculations were started near the stagnation point of the blade, resulting in laminar initial profiles. No other details about

the numerical procedure, specifically the creation of the initial profiles, were provided.

Wilcox [1975] used the Saffman [1972] k-ω^2 turbulence model to examine the effects of freestream turbulence levels on the simulation of transition for incompressible flat plate boundary layers. Wilcox simulated transition by modifying two empirical constants of the k-ω^2 governing turbulence equations as a function of the turbulent Reynolds number ($Re_t = k/\omega\nu$). Wilcox denoted the x-Reynolds number for the start of transition, Re_x^t, as the point where C_f is observed to deviate from the laminar value by more than 5%. Below the critical value of Re_x^t, Wilcox noted little or no amplification in turbulent kinetic energy (TKE), which signified the existence of a laminar boundary layer. However, when Re_x approached Re_x^t, an abrupt increase in TKE was observed, followed by an asymptotic approach to a value characteristic of fully turbulent flow. Wilcox identified the transitional regime as the range over which TKE increases from its initially low level to a much higher value in the turbulent regime. The transitional regime could also be identified from the numerical boundary layer characteristics by locating an abrupt change in the momentum thickness, shape factor, local friction coefficient, or Stanton number. Wilcox also noted similar results to Launder and Spalding, namely that an increase in freestream turbulence level caused the x-location for the start of transition to move upstream.

Dutoya and Michard [1981] used the Jones and Launder [1973] low-Reynolds number k-ε turbulence model to examine a developing turbine blade boundary layer and the resulting heat transfer distribution. Two model constants for the ε-equation were numerically optimized to simultaneously fit existing data for decay of isotropic turbulence, equilibrium turbulent boundary layer along a flat plate, and the onset of transition. Dutoya and Michard essentially used a standard k-ε turbulence model with two of the model constants adjusted to simulate transition. The initial profiles for all dependent variables were based on a Blasius velocity profile. Dutoya and Michard stated that the starting calculations were conducted

at $Re_x = 10^3$, but could be defined for $Re_x < 10^4$ (meaning shorter computer run times) without affecting the calculations. The numerical friction coefficient distribution for flow over an adiabatic flat plate were similar to other studies. Dutoya and Michard observed a rapid rise in the TKE profile at the onset of transition, similar to Wilcox [1975], and their comparison of the calculated displacement thickness Reynolds number data at the onset of transition matched the experimental data of McDonald and Fish [1973]. Good heat transfer predictions were obtained for flow along the suction side of a turbine blade, but the calculation trend on the pressure surface was to relaminarize the flow, which did not match experiment. Dutoya and Michard believed their program could not account for the complex nature of the transition process, but believed their method was a convenient way of calculating a boundary layer from near the stagnation point, through transition, to fully turbulent flow at a low computational cost.

Daniels and Browne [1981] evaluated five numerical programs to determine their heat transfer prediction capability for simulating the experimental gas turbine data of Daniels [1978]. The various turbulence models of the five codes varied from zero-equation turbulence models to a $k\text{-}\omega^2$ turbulence model. The various transition models of the five codes varied from an empirical input of experimental transition location data, to the transition correlations of Forest [1977], and to the transition model of McDonald and Fish [1973]. The comparisons of the numerical results with Daniels' experimental data showed general agreement in the laminar leading edge region and for the fully turbulent region on the blade suction surface. The numerical predictions were poor for the entire blade pressure side due to the complex flow field, and in the transition region on the suction side. Daniels and Browne concluded that with the limited data available, no distinct advantages were seen for using a more complicated two-equation turbulence model over the simple mixing length model to calculate turbine blade heat transfer on the turbine blade suction surface. The major difficulties of all the methods examined were the prediction of transition and the effect of freestream turbulence on the laminar boundary layer.

Arad et al. [1982] used the two-equation turbulence model of Ng [1971] with the low-Reynolds number functions of Wolfshtein [1970] to numerically predict transition from laminar to turbulent flow for a compressible axisymmetric boundary layer around a body of revolution. No transition model was used with the two-equation model; instead, transition was initiated by the diffusion of TKE and length scale into the boundary layer from the freestream. This type of model employs the "natural transition" capability of a two-equation turbulence model. The numerical predictions for transition Reynolds number based on displacement thickness, $Re_{\delta t}$, agreed reasonably well with the data of McDonald and Fish [1973]. Arad et al. noted that as the freestream length scale decreased (meaning an increase in freestream dissipation rate), $Re_{\delta t}$ increased, and as the freestream length scale increased (meaning a decrease in freestream dissipation rate), $Re_{\delta t}$ decreased. As expected, if the freestream length scale increases, more TKE will diffuse into the boundary layer promoting "natural transition" at a lower $Re_{\delta t}$. No discussion on the transition length, initial profile sensitivity, or initial starting location was provided. There was also no mention by Arad et al. concerning calculations for flows with pressure gradients.

Hylton et al. [1983], as mentioned earlier, examined the use of the Jones and Launder [1973] low-Reynolds number turbulence model in the STAN5 [Crawford and Kays, 1976] two-dimensional boundary layer code to predict the heat transfer distribution associated with their experimental turbine blade data and other open literature data. An intermittency model was used to simulate transition with the two-equation model. Hylton et al. realized that two-equation models had a "built in" transition model (which produces "natural transition") but they were attempting to see if the intermittency could be used to augment the "natural transition" of the two-equation model. They did not numerically predict any flow transition when using the two-equation model to simulate turbine blade heat transfer, due mostly to a numerical suppression of the inward diffusion of TKE from the outer boundary layer region. They did attempt to examine a combined high-Reynolds

number and low-Reynolds number turbulence model to open literature data but unreliable heat transfer predictions caused them to pursue a zero-equation turbulence model approach.

Wang et al. [1985] applied the low-Reynolds number two-equation model of Jones and Launder [1973] in the STAN5 [Crawford and Kays, 1976] boundary layer code to examine the turbine blade heat transfer measurements of Hylton et al. [1983] and Turner [1971]. No transition model was specified. Wang et al. believed that the difficulty encountered with two-equation models could be attributed to improper initial profiles and boundary conditions for TKE and turbulent dissipation rate (TDR) in the airfoil leading edge region. A two-zone model was developed to calculate the dissipation of TKE and TDR in the freestream boundary layer for the stagnation region. In the first zone, the freestream TKE and TDR boundary conditions do not dissipate until a "critical velocity" is reached. In the second zone, at the critical velocity point, the freestream TKE and TDR boundary conditions are allowed to dissipate. The critical velocity for the turbine blade pressure and suction surfaces are different because of the different flow fields around the leading edge. Friction coefficient data for flat plate zero pressure gradient simulations was presented but no comparison was made with experimental data. For turbine blade simulations, the heat transfer calculations of Wang et al. agreed reasonably well with experimental data. On the suction surface of the blade, the heat transfer predictions were high in the transitional and turbulent region. On the pressure surface, the general trends in the experimental data were matched.

Rodi and Scheuerer [1985a, 1985b] coupled the low-Reynolds number model of Lam and Bremhorst [1981] together with an empirical method for prescribing initial profiles for TKE and TDR to control transition and numerically predict the heat transfer measurements of Blair and Werle [1980, 1981] and Daniels and Browne [1981]. Transition prediction methods coupled with two-equation turbulence models up to this point have modeled transition by controlling the TKE and TDR freestream boundary conditions, resulting in a control of the diffusion rate of

the turbulence quantities from the freestream. Rodi and Scheuerer believed empirical information must also be supplied in the initial turbulent profiles in order to obtain satisfactory transition predictions. They conducted a sensitivity analysis of the transition calculations to prescribed initial and boundary conditions. Their results yielded an method for obtaining TKE and TDR initial profiles that improved transition predictions. An empirical coefficient, a_1, used to define the TDR initial profile, was calibrated against the flat plate data of Blair and Werle to match the numerically predicted transition Reynolds number to the experimental data. A graph of a_1 versus turbulence freestream turbulence intensity was formulated from the calibration tests. This a_1 constant was used to adjust the initial TDR profile which in turn adjusted the numerical transition predictions. In modeling the data of Daniels and Browne, Rodi and Scheuerer obtained good predictions for the suction surface heat transfer with discrepancies occurring only in the transition region where the numerical method calculated a shorter transition length than experimentally measured. On the pressure surface, Rodi and Scheuerer obtained excellent heat transfer predictions.

Zerkle and Lounsbury [1987] applied the initial profiles proposed by Rodi and Scheuerer [1985a] and the Lam and Bremhorst [1981] turbulence model in their version of STAN5 [Crawford and Kays, 1976] to examine the heat transfer of Blair and Werle [1980] and several turbine blade cascades. Overall, the numerical results matched the experimental data reasonably well except in the transition region.

Recent work by Schmidt [1987] has been an extensive investigation on predicting boundary layer transition with two-equation turbulence models. Schmidt's work was two-fold. First, he investigated the basic "mechanics" of turbulent flow predictions with two-equation models to document their behavior before attempting to model more complex flows. Second, he proposed a transition model used to control the path of transition resulting in more accurate predictions in the transition region. Schmidt conducted a thorough investigation into the effects the TKE and

TDR initial profiles of Rodi and Scheuerer have on transition and described guidelines for their use. Schmidt evaluated the numerical characteristics of the Lam and Bremhorst [1981] and Launder and Sharma [1974] two-equation models. In the process, he discovered and put forth corrections to slight numerical instabilities in the models. As discussed by Wilcox [1975], transition may be identified by an abrupt increase in the boundary layer TKE. Schmidt proposed a method for simulating the path of transition by controlling the growth rate of the production of TKE in the boundary layer. The proposed model controlled the time rate-of-change of the production of TKE which is converted to spatial coordinates through the local convection velocity. This model was termed a production term modification model or PTM model. The transition model parameters were calibrated against the experimental work of Abu-Ghannam and Shaw [1980] to allow the model to modify the production of TKE based on the local freestream turbulence level. The comparison of Schmidt's numerical heat transfer predictions with the experimental flat plate data of Blair and Werle [1980,1981] and Rued and Wittig [1984] along with the turbine blade data of Daniels and Browne [1981] and Hylton et al. [1983] produced very good results even in the transition region. The unique aspect of Schmidt's transition model is its flexibility and ease with which it may be implemented into any two-equation turbulence model.

Johnson [1987] developed a spatially-based transition model, similar in form to Schmidt's transition model, and coupled it with the K. Y. Chien [1982] two-equation turbulence model in TEXSTAN (described in Section 1.5). Johnson calibrated the transition model constants against the flat plate transition data of Blair and Werle [1980, 1981], then compared various experimental gas turbine blade heat transfer distributions to his numerical heat transfer calculations. The numerical calculations of the heat transfer distributions for the Blair and Werle data generally matched, even in the transition region. The comparison of Johnson's numerical heat transfer predictions with the various cylinder flows and turbine blade heat transfer data demonstrated difficulty in the transition region for the suction surfaces and consistent under-prediction of the pressure surface heat transfer. Johnson

attributed some of the possible numerical error on inadequate specification of the far-field velocity and turbulence intensity for some of the experimental data sets.

Sullivan [1988] investigated the use of the K. Y. Chien two-equation model coupled with two different transition models in TEXSTAN to simulate the experimental heat transfer data for flat plate and circular cylinder flow. Sullivan examined the use of an intermittency model and the PTM model developed by Schmidt. Sullivan obtained good results for the experimental heat transfer distribution for both flow fields using the PTM model but some discrepancies in predicting the start of transition for the cylinder flow were present.

A review of the literature indicates that the low-Reynolds number two-equation turbulence model has the potential for modeling the qualitative aspects of flow transition. However, there are two important criteria that must be met before the modeling of transition can possibly be attained. First, the prediction of transition will only be as good as the turbulence model used with it. Therefore, a detailed knowledge of the prediction capability of the turbulence model for laminar boundary layers is just as important as in fully turbulent boundary layers. Second, the specification of "physically" correct boundary and initial conditions are important because the "natural transition" capability of two-equation turbulence model, as well as any transition model, will be influenced by unrealistic starting conditions. Only when these two criteria are met, can the prediction capability of a transition model be evaluated and improved.

1.4 Overview of Experimental Transition Studies

The purpose of this section is to outline available experimental transition studies from the open literature that detail enough flow field information to allow numerical transition model behavior to be assessed. Information about the behavior of proposed transition models can not be completely assessed because some ex-

perimental data in the open literature do not provide enough information about the freestream turbulence quantities. Hylton et al. [1983] discussed the importance of boundary and initial conditions on the numerical prediction of turbine blade heat transfer distributions. As discussed previously, two-equation turbulence models display a "natural transition" which is a function of the diffusion of TKE and TDR into the boundary layer from the outer region. Therefore, a requirement for accurate transition simulations depends on a knowledge of freestream TKE and TDR distributions from experimental data. At a minimum, the freestream turbulence intensity, Tu_e, must be specified at two locations in order to calculate the initial freestream value of TDR. In general, the more experimental freestream turbulence intensity data available, the more accurate the initial freestream value of TDR may be calculated.

In the literature review conducted by Schmidt [1988], an outline of experimental data available in the open literature containing enough information about experimental freestream turbulence levels was presented. Schmidt determined the experimental data of Blair and Werle [1980, 1981, 1983a and 1983b], Reud and Wittig [1985], and Wang et al. [1985] are currently the only experimental data available that provide enough freestream turbulence data to accurately calculate TKE and TDR initial conditions.

Blair and Werle [1980, 1981, 1983a, 1983b] investigated the laminar to turbulent transition occurring over a heated flat plate subjected to various freestream turbulence intensities and pressure gradients. The objectives of their study were to accurately determine the magnitude the effects of freestream turbulence has on turbulent boundary layer heat transfer and to provide a thoroughly documented set of experimental data for use in improving the analytical modeling of this phenomena. The experimental tests consisted of both zero pressure gradient flow and constant acceleration flow. The total wall-to-freestream temperature difference was approximately 15 K. The range of freestream turbulence intensities for the test cases were approximately 0.25% to 7%, generated by four different turbulence generat-

ing grids upstream of a contraction in the test section. The freestream velocity was 30.3 m/s and the test section pressure was ambient. Blair and Werle measured all three normal components of the Reynolds stress, the Stanton number distribution, and the freestream turbulence intensity for the entire length of the test section.

Reud and Wittig [1984] obtained experimental data on the effects of freestream turbulence, wall cooling, and strong favorable pressure gradients on the laminar to turbulent boundary layer transition. For these tests the freestream turbulence was generated by grids and provided turbulence intensity levels from 1.6% to 11%. Reud and Wittig measured only the $\overline{u'^2}$ and $\overline{v'^2}$ turbulence components, and the $\overline{w'^2}$ component was assumed to be equal to the $\overline{v'^2}$ component. Turbulence intensity and Stanton number distributions are provided for the entire test section.

Wang et al. [1985] focused on the effect of freestream turbulence intensity on transition. Profiles of velocity, temperature, Reynolds normal stress ($\overline{u'^2}$), and Reynolds shear stress ($\overline{u'v'}$) were measured along with Stanton number and friction coefficient distributions. The turbulence intensity levels investigated were 0.7% and 2.0%.

A special note must be made for the experimental work conducted by Abu-Ghannam and Shaw [1980]. An important relationship in transition modeling is the knowledge of the start and end of transition. Abu-Ghannam and Shaw detailed past experimental efforts for a correlation between momentum thickness Reynolds number and freestream turbulence intensity. With this knowledge and their own experimental work, Abu-Ghannam and Shaw developed correlations to predict the start and end of transition as a function of freestream turbulence intensity for zero and non-zero pressure gradient flows. These correlations are based on many experimental data sets and therefore are not biased to any particular set of experimental results.

1.5 Description of TEXSTAN

This section outlines the computer code, TEXSTAN, that was used in this study to numerically solve the governing boundary layer equations. TEXSTAN is based on the STAN5 boundary layer program developed by Crawford and Kays [1976]. The finite-difference numerical scheme of TEXSTAN is based on the numerical algorithm by Patankar and Spalding [1970], with additional changes incorporated by Pietrzyk [1985] and Benton [1985].

TEXSTAN solves the steady two-dimensional parabolic differential equations that govern boundary layer flow. This program sequentially solves the momentum equation and any number of diffusion, e.g.. transport, equations, such as stagnation enthalpy, TKE, TDR, and mass concentration governing equations. The equations solved by TEXSTAN are transformed using a nondimensional stream function, then integrated over a finite control volume to obtain finite-difference equations for each grid point in the calculation domain. This discretization technique is known as a control-volume formulation and is described in detail by Patankar [1980]. A number of different source terms may be included in the transport equations. In the momentum equation, buoyancy effects and an axially varying general body force may be considered. In the energy equation, viscous dissipation, internal heat generation, and body force work terms may be included.

TEXSTAN can be used to analyze a variety of flow geometries. An axisymmetric coordinate system is adapted so it may easily be converted to a cartesian coordinate system by setting the radius of curvature to unity. TEXSTAN has the capability of solving both external boundary layer flow for flat plate or axisymmetric bodies of revolution and internal boundary layer flow for circular pipes, parallel planes, or concentric annuli. The external flow capability was used throughout this study.

TEXSTAN has the capability of modeling different boundary conditions. For external flows, the freestream conditions for velocity, stagnation enthalpy, TKE, and TDR are provided as level specifications while the wall conditions may be specified as either a level or flux. The user may specify the initial profiles of the dependent variables from experimental data or the automatic profile generator in TEXSTAN may be used. For this study, a computer code, TEXIPBC, was developed by the author to calculate "physically" correct boundary conditions and initial profiles for transitional studies. An outline of TEXIPBC is discussed in Chapter 3.

Fluid properties may be treated as constant or variable. Constant properties are supplied by the user, while the variable fluid properties are supplied through property subroutines that are essentially tabulated fluid properties. This research used air as the working fluid.

Several different turbulence models are incorporated in TEXSTAN, all of which use the mean field closure approximation. The turbulence models consist of a Prandtl mixing length zero-equation turbulence model and several two-equation k-ϵ turbulence models. Provisions for laminar-to-turbulent transition is available for the Prandtl mixing length model using a critical momentum thickness Reynolds number criteria to adjust the van Driest damping function until the flow is fully turbulent. No transition model is provided for the two-equation turbulence models.

1.6 Thesis Outline

This chapter has described the basic goals of the thesis and provided relevant background information on the modeling of external heat transfer on gas turbines. The environment of the gas turbine has been detailed with emphasis on the characteristics of the flow field that must be numerically modeled. An overview of turbulence modeling was presented to familiarize the reader to various methods used to numerically model turbulence. Relevant numerical investigations from the

open literature for simulating turbine blade heat transfer distributions were presented to detail the performance of past methods and provide insight into the behavior of turbulence modeling. Available experimental data providing important turbulence information required for accurate evaluation of turbulence models was detailed. An outline to the numerical boundary layer code, TEXSTAN, used in this thesis was discussed.

Chapter 2 provides the mathematical derivation of the boundary layer governing equations solved by TEXSTAN. The governing equations consist of the time-averaged momentum and stagnation enthalpy equations along with the k-ε transport equations used for mean field closure. The K. Y. Chien [1982] and Launder and Sharma [1974] two-equation turbulence models are outlined, along with a discussion of the two transition models originally proposed to be investigated by this thesis.

Chapter 3 details the process used by TEXIPBC to generate "physically" correct boundary conditions and initial profiles required for a well-posed numerical simulation. The need for a smooth freestream velocity distribution to calculate and accurate pressure gradient is examined. Two methods for obtaining valid initial TKE and TDR levels for calculating proper decay of the freestream turbulence quantities are presented. Also, a solution to a problem associated with the freestream length scale distribution for the K. Y. Chien [1982] two-equation model is discussed.

Chapter 4 assesses the criteria for the proposed initial TKE and TDR profiles and their effect on the "natural transition" predictions of the K. Y. Chien [1982] two-equation turbulence model. Numerical calibration of the k-equation production modification, last proposed by Schmidt [1987], is developed for the K. Y. Chien turbulence model, along with comparisons of the numerical transition prediction capability with experimental flat plate heat transfer distributions. It is at

this point that the problem associated with using the K. Y. Chien two-equation model for transition studies is detailed.

Chapter 5 provides a summary of the conclusions formulated in this thesis, and a brief discussion of recommendations for future work is presented.

Chapter 2

Mathematical Description of Two-Dimensional Boundary Layer Flow

2.0 Introduction

In fluid flow, the boundary layer is a thin region close to a solid body where vorticity exists and viscous effects are important. Boundary layers over flat surfaces with sharp leading edges start laminar then, due to flow instabilities, transition and become turbulent boundary layers. This process also occurs on a wide variety of surfaces of engineering importance such as heat exchanger fins, airfoils, and nozzles. Various engineering design factors, such as local friction coefficient and heat transfer, may be predicted through the solution of the governing boundary layer equations, provided the pressure distribution over the surface is known. This chapter outlines the governing boundary layer equations that are numerically solved by TEXSTAN for both laminar and fully turbulent flow. These governing equations consist of the time-averaged continuity equation, momentum equation, and stagnation enthalpy equation for flow of a variable property fluid. The turbulent transport equations for two-equation mean field closure are outlined as well as the proposed transition models used in this study.

The basic characteristic of a turbulent flow is that the velocity field is time dependent; however, any attempt to describe the velocity field as a function of time is difficult. A measurement at a point in a steady turbulent flow field yields a velocity that fluctuates in an irregular manner around a steady time-independent velocity (i.e. mean velocity). The fluctuating velocity components are time-dependent. Since the fluctuating components tend to be small relative to the mean velocity, a statistical approach of time-averaging is applied to the time-dependent velocity components, thus allowing the flow to be treated as if it were steady. In other

words, in the context of time-averaging, the mean values are examined over a sufficiently long interval of time that they are considered independent of time. In the equations that follow, a Reynolds decomposition method is used to express the instantaneous dependent quantities (denoted by "~") into mean (denoted by upper case) and fluctuating (denoted by primes) components. As an example, the Reynolds decomposition of the instantaneous streamwise (x-direction) and instantaneous cross-stream (y-direction) velocity components are

$$\tilde{U} = U + u' , \tag{2.1}$$

and

$$\tilde{V} = V + v' . \tag{2.2}$$

Fluid properties are assumed to be variable but without fluctuating components. Therefore, the properties may be expressed as

density: $$\tilde{\rho} = \rho , \tag{2.3}$$

dynamic viscosity: $$\tilde{\mu} = \mu . \tag{2.4}$$

To develop the governing turbulent boundary layer equations, the Reynolds decomposition expressions for the dependent variables are substituted into the instantaneous governing equations, then the equations are averaged over time. The resulting boundary layer equations for turbulent flow contain new terms, such as Reynolds stress and turbulent heat flux terms, that must be modeled using some form of turbulence models.

2.1 Boundary Layer Assumptions

Figure 2.1 is a sketch of the geometry, x-y coordinate system, and basic nomenclature used to describe a boundary layer. Shown in Figure 2.1 is a bound

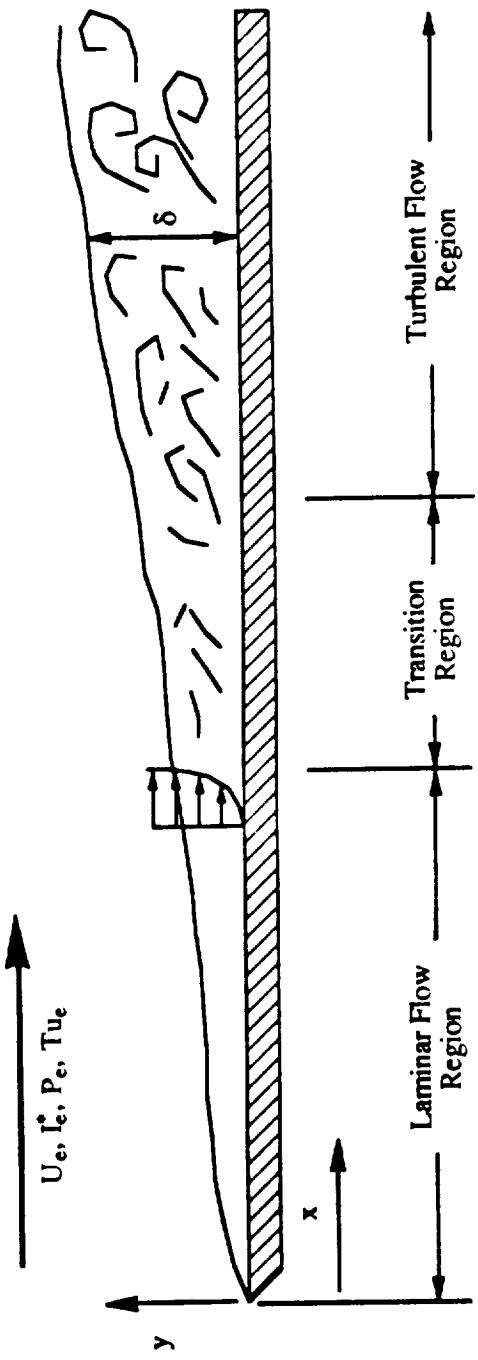

Figure 2.1. Geometry and nomenclature describing a developing boundary layer.

ary layer region where the fluid velocity changes from a freestream value, U_e, to zero at the wall. For y-distances greater then the boundary layer thickness, δ, the flow field vorticity vanishes and the flow is considered inviscid and may be described by Euler equations. On the other hand, the boundary layer region has particular characteristics which allow the full Navier-Stokes equations to be simplified. These simplifying boundary layer characteristics are termed boundary layer assumptions and apply to both the momentum and energy governing equations. This section outlines the assumptions used to develop the boundary layer equations from the full Navier-Stokes equations.

If the boundary layer thickness (δ) is small relative to all other flow dimensions, then the following conditions must hold for a two-dimensional boundary layer

$$\tilde{U} >> \tilde{V} \tag{2.5}$$

and

$$\frac{\partial \tilde{U}}{\partial y} >> \frac{\partial \tilde{U}}{\partial x}, \frac{\partial \tilde{V}}{\partial x}, \frac{\partial \tilde{V}}{\partial y}. \tag{2.6}$$

Consistent with equations (2.5) and (2.6) in which the flow is predominantly in the x-direction, an examination of the y-momentum equation demonstrates that the cross-stream pressure gradient is approximately zero. As a result, the pressure gradient becomes only a function of the x-location

$$\frac{\partial \tilde{P}}{\partial y} \approx 0 \tag{2.7}$$

and

$$\frac{\partial \tilde{P}}{\partial x} = \frac{d\tilde{P}}{dx}. \tag{2.8}$$

Integrating equation (2.7) across the boundary layer proves the pressure normal to the boundary layer is constant and may be assumed equal to the pressure at the

outer edge of the boundary layer. The pressure is said to be "impressed" on the boundary layer by the outer flow [Schlichting, 1979]. The freestream pressure is calculated using an inviscid flow calculation. Equations (2.5) to (2.8) are the boundary layer approximations for the momentum equation.

When there is heat transfer between the fluid and the surface of a body, the temperature changes occur within the thermal boundary layer. As with the momentum boundary layer, the thinness of the thermal boundary layer (Δ) allows the following condition to hold

$$\frac{\partial \widetilde{T}}{\partial y} >> \frac{\partial \widetilde{T}}{\partial x} . \tag{2.9}$$

Equation (2.9) is the boundary layer approximation for the thermal boundary layer. This approximation states the cross-stream temperature gradients are much larger than the streamwise temperature gradients.

2.2 Continuity Equation

The law of conservation of mass states that mass can not be created or destroyed. The instantaneous continuity equation is

$$\frac{\partial \rho}{\partial t} + \frac{\partial (\rho \widetilde{U})}{\partial x} + \frac{\partial (\rho \widetilde{V})}{\partial y} + \frac{\partial (\rho \widetilde{W})}{\partial z} = 0 . \tag{2.10}$$

By time-averaging equation (2.10) using standard averaging rules [Kays and Crawford, 1980], the time-averaged continuity equation is defined as

$$\frac{\partial (\rho U)}{\partial x} + \frac{\partial (\rho V)}{\partial y} + \frac{\partial (\rho W)}{\partial z} = 0 . \tag{2.11}$$

Subtracting equation (2.11) from equation (2.10) yields the fluctuating continuity equation.

$$\frac{\partial(\rho u')}{\partial x} + \frac{\partial(\rho v')}{\partial y} + \frac{\partial(\rho w')}{\partial z} = 0 . \qquad (2.12)$$

Equations (2.11) and (2.12) show that the mean and fluctuating velocity components each separately satisfy the continuity equation. The continuity equation is not solved directly by TEXSTAN due to the variable transformation from primitive velocity variables to a compressible stream function, that is subsequently nondimensionalized.

2.3 Momentum Equation

The law of conservation of momentum states that the net force on a control volume is equal to the time rate-of-change of momentum of the control volume. The instantaneous x-momentum equation for a two-dimensional flow of a variable property fluid with negligible body forces is

$$\frac{\partial(\rho\tilde{U})}{\partial t} + \frac{\partial(\rho\tilde{U}\tilde{U})}{\partial x} + \frac{\partial(\rho\tilde{V}\tilde{U})}{\partial y} = -\frac{dP}{dx} + \frac{\partial}{\partial y}\left(\mu\frac{\partial\tilde{U}}{\partial y}\right). \qquad (2.13)$$

The momentum boundary layer assumptions, equations (2.5) through (2.8), are used in defining equation (2.13). Time-averaging equation (2.13) and applying equation (2.11) yields the mean x-momentum equation

$$\rho U\frac{\partial U}{\partial x} + \rho V\frac{\partial U}{\partial y} = -\frac{dP}{dx} + \frac{\partial}{\partial y}\left(\mu\frac{\partial U}{\partial y} - \rho\overline{u'v'}\right). \qquad (2.14)$$

In equation (2.14), the left-hand terms represent the convective transport of momentum in the boundary layer by the mean flow. The first term on the right-hand side represents a momentum source term, namely the pressure gradient, and the second term on the right-hand side represents the molecular and turbulent diffusion of momentum in the boundary layer.

The turbulent diffusion term in equation (2.14), $-\rho\overline{u'v'}$, is created by the time-averaging of equation (2.13). This new term is called the turbulent Reynolds stress. A companion term arises, the x-gradient of $\rho\overline{u'u'}$, but is neglected commensurate with the boundary layer assumptions. The Reynolds stress is the contribution of turbulent motion to the boundary layer stresses and plays a significant role in the transfer of momentum by turbulent motions. For a two-dimensional boundary layer, $-\rho\overline{u'v'}$ is the dominant Reynolds stress term, except in the viscous sublayer. Examining equation (2.14) shows there are three unknowns, U, V, and $-\rho\overline{u'v'}$, but only two equations, continuity and x-momentum, to solve for the unknowns. This inconsistency of equations to unknowns demonstrates the apparent closure problem in turbulence modeling.

The simplest procedure for solving the closure problem is to develop a constitutive equation to describe the Reynolds stress, and therefore provide a solution for the boundary layer flow. An approximation is defined to evaluate the Reynolds stresses by comparing the turbulent Reynolds stress to the corresponding viscous stresses. The Boussinesq approximation assumes the turbulent stresses act like the viscous stresses and are directly proportional to the mean velocity gradient [Hinze, 1975]. This approximation is called mean field closure (MFC) and can assume several forms

$$-\rho\overline{u'v'} = \rho\varepsilon_M\frac{\partial U}{\partial y} = \rho\nu_t\frac{\partial U}{\partial y} = \mu_t\frac{\partial U}{\partial y}, \qquad (2.15)$$

where ε_M is the eddy diffusivity for momentum and μ_t is the turbulent viscosity.

The eddy diffusivity depends on the turbulence in the flow, hence it is a function of position and not a fluid property. The turbulence closure problem reduces to calculating ε_M. The effective viscosity, μ_{eff}, is defined as the sum of the molecular viscosity and the turbulent viscosity ($\mu_{eff} = \mu + \mu_t$). The mean momentum equation is rewritten by combining the effective viscosity and equations (2.14) and (2.15) to yield

$$\rho U\frac{\partial U}{\partial x} + \rho V\frac{\partial U}{\partial y} = -\frac{\partial P}{\partial x} + \frac{\partial}{\partial y}\left(\mu_{eff}\frac{\partial U}{\partial y} \right). \qquad (2.16)$$

Equation (2.16) is the governing boundary layer momentum equation solved by TEXSTAN for both laminar and turbulent flows in the absence of body forces. When the flow field is laminar and the turbulent viscosity is zero, equation (2.16) becomes the steady laminar boundary layer momentum equation.

As discussed by Rodi [1982], the use of low-Reynolds number two-equation models has become popular because of its ability to model the effects of turbulence history and transport on the velocity and length scale of turbulent motion. The expression of turbulent viscosity for two-equation models in the form of equation (1.6) is

$$\mu_t = \rho C_\mu f_\mu \frac{k^2}{\hat{\varepsilon}}, \qquad (2.17)$$

where k is the turbulent kinetic energy (TKE) of the flow, $\hat{\varepsilon}$ is the isotropic turbulent dissipation rate (TDR) of the flow, C_μ is an empirical constant, and f_μ is a near wall damping function. Equation (2.17) is the essence of two-equation turbulence modeling and may be used in conjunction with equation (2.15) to calculate the Reynolds stress term of the momentum equation. The nonisotropic dissipation rate, ε, can be related to the isotropic dissipation rate by

$$\varepsilon = \hat{\varepsilon} + D \cdot \tag{2.18}$$

In equation (2.18) ε is the nonisotropic dissipation rate, possessing a finite wall value; $\hat{\varepsilon}$ is the isotropic dissipation rate, that is zero at a solid wall; and D is the low-Reynolds number term. The addition of D, discussed later, was proposed by Jones and Launder [1972] to allow the solution of a transport equation for $\hat{\varepsilon}$ rather than ε and still satisfy the finite dissipation rate boundary condition at the wall (i.e. y = 0).

The evolution of the turbulent viscosity in equation (2.17) requires the use of transport equations to describe the evolution of TKE and TDR through the boundary layer. Appendix A provides details on deriving the TKE and TDR transport equations. The final model form of the TKE and TDR transport equations, from Appendix A and following Patel et al. [1985], are

$$\rho U\frac{\partial k}{\partial x} + \rho V\frac{\partial k}{\partial y} = \mu_t\left(\frac{\partial U}{\partial y}\right)^2 + \frac{\partial}{\partial y}\left[\left(\mu + \frac{\mu_t}{\sigma_k}\right)\frac{\partial k}{\partial y}\right] - \left(\rho\hat{\varepsilon} + D\right), \tag{2.19}$$

and

$$\rho U\frac{\partial \hat{\varepsilon}}{\partial x} + \rho V\frac{\partial \hat{\varepsilon}}{\partial y} = C_1 f_1 \frac{\hat{\varepsilon}}{k}\mu_t\left(\frac{\partial U}{\partial y}\right)^2 + \frac{\partial}{\partial y}\left[\left(\mu + \frac{\mu_t}{\sigma_\varepsilon}\right)\frac{\partial \hat{\varepsilon}}{\partial y}\right] - \left[\rho C_2 f_2 \frac{\hat{\varepsilon}^2}{k} + E\right]. \tag{2.20}$$

The TKE and TDR transport equations contain five empirical constants: C_μ, C_1, C_2, σ_k, and σ_ε and three damping functions: f_μ, f_1, and f_2, along with two additional terms D and E.

Equations (2.19) and (2.20) are low-Reynolds number forms of a k-ε turbulence model. Jones and Launder [1972] proposed the use of damping functions f_μ, f_1, and f_2, as functions of the turbulent Reynolds number, $Re_t = k^2/\nu\hat{\varepsilon}$, to modify the values of the C-constants so that calculations may be made through the

buffer and viscous sublayer to the wall. The low-Reynolds number terms (D and E) modify the isotropic behavior of TDR, for near-wall calculations. All k-ε two-equation turbulence models are represented by equations (2.19) and (2.20), with the values of the constants, damping functions, and additional terms distinguishing the different two-equation models.

In equation (2.19), the left-hand term represents the convective transport of TKE by the mean flow. The first term on the right-hand side represents the production of TKE and simulates the kinetic energy exchange between the mean flow and the turbulence. Normally this energy exchange involves a loss of mean kinetic energy from the mean flow and a profit in the TKE of the turbulence. The second term on the right-hand side is diffusional, i.e. a transport term whose integral over the boundary layer is zero, and it represents the redistribution of TKE in the boundary layer. This term is composed of both the turbulent diffusion and molecular diffusion of TKE. The third term on the right-hand side represents the viscous dissipation, with the low-Reynolds number term (D) compensating for the zero boundary condition for $\hat{\varepsilon}$.

In equation (2.20), the left-hand term represents the convection of TDR by the mean flow. The first term on the right-hand side represents the production of turbulent dissipation by the mean flow. The second right-hand term represents the molecular and turbulent diffusion of TDR in the boundary layer. The third term of the right-hand side represents the viscous dissipation of TDR, with the low-Reynolds number term (E) included to improve the match of the peak level of TKE with experiment [Jones and Launder, 1972].

2.4 Stagnation Enthalpy Equation

The law of conservation of energy states that the increase in energy within a region is the result of work and heat transfer to the region. The instantaneous boundary layer form of the stagnation enthalpy equation for a variable property fluid without internal heat generation and body force work is

$$\frac{\partial(\rho\tilde{I}^*)}{\partial t} + \frac{\partial(\rho\tilde{U}\tilde{I}^*)}{\partial x} + \frac{\partial(\rho\tilde{V}\tilde{I}^*)}{\partial y} = -\frac{\partial\tilde{q}}{\partial y} + \frac{\partial}{\partial y}\left[\tilde{U}\mu\frac{\partial\tilde{U}}{\partial y}\right], \tag{2.21}$$

where $\tilde{q}$ is the molecular heat flux. The thermal boundary layer assumption, equation (2.9), is used in defining equation (2.21). The molecular heat flux is formulated using Fourier's law of heat conduction as follows

$$\tilde{q} = -k\frac{\partial\tilde{T}}{\partial y}, \tag{2.22}$$

where k is the thermal conductivity and $\tilde{T}$ is the instantaneous static temperature. The thermodynamic equation of state for a perfect gas relates the instantaneous static enthalpy to the instantaneous static temperature as shown

$$d\tilde{I} = c\, d\tilde{T} \tag{2.23}$$

where c is the specific heat at constant pressure. The instantaneous static enthalpy is related to the instantaneous stagnation enthalpy using the following relation

$$\tilde{I} = \tilde{I}^* - \frac{\tilde{U}^2}{2} \tag{2.24}$$

Using equations (2.23) and (2.24), equation (2.22) is recast in terms of the instantaneous stagnation enthalpy as shown

$$\tilde{q} = -\frac{\mu}{Pr}\left(\frac{\partial \tilde{I}^*}{\partial y} - \frac{\partial}{\partial y}\left(\frac{\tilde{U}^2}{2}\right)\right), \tag{2.25}$$

where k/c is equal to μ/Pr. The Prandtl number is used to relates the molecular diffusivity to the thermal diffusivity. Using equation (2.25), equation (2.21) is rewritten as follows

$$\rho U\frac{\partial \tilde{I}^*}{\partial x} + \rho V\frac{\partial \tilde{I}^*}{\partial y} = \frac{\partial}{\partial y}\left[\frac{\mu}{Pr}\frac{\partial \tilde{I}^*}{\partial y}\right] + \frac{\partial}{\partial y}\left[\left(1 - \frac{1}{Pr}\right)\mu\frac{\partial}{\partial y}\left(\frac{\tilde{U}^2}{2}\right)\right]. \tag{2.26}$$

In equation (2.26) the molecular heat flux term has been recast in terms of a gradient in stagnation enthalpy, which leads to the more complex form of the viscous work term.

Time-averaging equation (2.26) and the application of continuity, equation (2.11), yields the mean stagnation enthalpy equation

$$\rho U\frac{\partial I^*}{\partial x} + \rho V\frac{\partial I^*}{\partial y} = \frac{\partial}{\partial y}\left[\frac{\mu}{Pr}\frac{\partial I^*}{\partial y} - \overline{\rho v' i^{*\prime}}\right] + \frac{\partial}{\partial y}\left[\left(1 - \frac{1}{Pr}\right)\mu\frac{\partial}{\partial y}\left(\frac{U^2}{2}\right)\right]. \tag{2.27}$$

In equation (2.27), the left-hand terms represent the convective transport of stagnation enthalpy in the boundary layer by the mean flow. The first term on the right-hand side represents the molecular and turbulent diffusion of stagnation enthalpy in the boundary layer, and the second term on the right-hand side is a source term and represents both a diffusion and dissipation of energy when the term is expanded.

Equation (2.27) contains a new term, $-\overline{\rho v' i^{*\prime}}$, created by the time-averaging of equation (2.26). This new term is called the turbulent heat flux. It is the contribution of turbulent motion to the boundary layer temperature distribution and plays

an important role in the heat transfer due to turbulent motion. The companion term, the x-gradient of $\rho\overline{u'i^{*'}}$, is neglected commensurate with the boundary layer assumptions. As with the momentum equation, there is a closure problem associated with the solution of the stagnation enthalpy equation. The turbulent heat flux is the one undefined term in equation (2.27) and requires a constitutive equation in order to solve the stagnation enthalpy equation.

Before defining the constitutive relation for the turbulent heat flux, an expression for the fluctuating stagnation enthalpy must be defined. The fluctuating stagnation enthalpy can be decomposed into a fluctuating static enthalpy and a velocity term, following Kays and Crawford [1980],

$$i^{*'} \approx i' + Uu' . \tag{2.28}$$

Using equation (2.28), the turbulent heat flux may be approximated as

$$-\rho\overline{v'i^{*'}} \approx -\rho\overline{v'i'} + U\left(-\rho\overline{u'v'}\right) . \tag{2.29}$$

Using a Boussinesq type of mean field closure argument, the turbulent heat flux is assumed proportional to the mean temperature gradient. Therefore, an eddy diffusivity for heat transfer (ε_H) may be defined in the same manner the eddy diffusivity for momentum is defined to relate the Reynolds stress to the mean velocity gradient. The eddy diffusivity model for heat transfer uses the eddy conductivity (k_t) to relate the turbulent heat flux to the mean stagnation enthalpy gradient. Therefore, the eddy diffusivity model for heat transfer, like the momentum counter part , can assume several forms

$$-\rho\overline{v'i'} = \varepsilon_H\frac{\partial I}{\partial y} = \frac{k_t}{c}\frac{\partial}{\partial y}\left[I^* - \frac{U^2}{2}\right] = \frac{\mu_t}{Pr_t}\frac{\partial}{\partial y}\left[I^* - \frac{U^2}{2}\right], \tag{2.30}$$

where Pr_t is the turbulent Prandtl number, formulated as $\mu_t c/k_t$ in analogy to the laminar Prandtl number. The stagnation enthalpy form of the turbulent heat flux is formulated by combining equations (2.30) and (2.15) into (2.29), which yields

$$-\rho\overline{v'i^{*\prime}} = \frac{\mu_t}{Pr_t}\frac{\partial}{\partial y}\left[I^* - \frac{U^2}{2} \right] + \mu_t \frac{\partial}{\partial y}\left(\frac{U^2}{2} \right). \tag{2.31}$$

The laminar (molecular) and turbulent conductivity may be expressed in terms of an effective thermal conductivity (divided by the specific heat, c) as shown

$$\left(\frac{k}{c}\right)_{eff} = \frac{k}{c} + \left(\frac{k}{c}\right)_t . \tag{2.32}$$

Using equation (2.32) and the definition of the effective viscosity (μ_{eff}), the effective Prandtl number, Pr_{eff}, is defined as follows

$$Pr_{eff} = \frac{\mu_{eff}}{\left(\frac{k}{c}\right)_{eff}} = \frac{\mu_{eff}}{\frac{\mu}{Pr} + \frac{\mu_t}{Pr_t}} \tag{2.33}$$

The mean stagnation enthalpy equation is rewritten by combining the effective Prandtl number definition (equation 2.33) and equation (2.31) to yield

$$\rho U\frac{\partial I^*}{\partial x} + \rho V\frac{\partial I^*}{\partial y} = \frac{\partial}{\partial y}\left[\frac{\mu_{eff}}{Pr_{eff}}\frac{\partial I^*}{\partial y} \right] + \frac{\partial}{\partial y}\left[\left(1 - \frac{1}{Pr_{eff}} \right) \mu_{eff} \frac{\partial}{\partial y}\left(\frac{U^2}{2} \right) \right]. \tag{2.34}$$

Equation (2.34) is the governing energy equation solved by TEXSTAN for both laminar and turbulent flows in the absence of thermal heat sources and body force work. For a laminar flow calculation, the turbulent Prandtl number and turbulent viscosity are set to zero, and equation (2.34) becomes the steady laminar equation.

Turbulence modeling with heat transfer requires specification of the turbulent Prandtl number. For fully turbulent high Reynolds number flows, Pr_t is variable between the wall and the freestream, see for instance Kays and Crawford [1980]. For the numerical simulations of transitional flows in this thesis, the turbulent Prandtl number was assumed a constant 0.9.

2.5 Two-Equation Turbulence Models

This investigation focuses on the use of the K. Y. Chien [1982] two-equation low-Reynolds number turbulence model for transition simulations. This section presents the empirical constants and damping functions which constitutes the K. Y. Chien turbulence model. In Chapter 4, the transition predictions of the Launder and Sharma [1974] low-Reynolds number turbulence model are compared to the K. Y. Chien model. Therefore this section also presents the empirical constants and damping functions for the Launder and Sharma turbulence model.

K. Y. Chien [1982] developed a variation to the two-equation, low-Reynolds number turbulence model proposed by Jones and Launder [1972]. The TKE and TDR equations used by Chien are of the form defined by equations (2.19) and (2.20), with the empirical constants, damping functions, and extra terms defined as follows.

Empirical Constants:

$$C_1 = 1.35 \tag{2.35}$$

$$C_2 = 1.8 \tag{2.36}$$

$$C_\mu = 0.09 \tag{2.37}$$

$$\sigma_k = 1.0 \tag{2.38}$$

$$\sigma_\varepsilon = 1.3 \tag{2.39}$$

Damping functions:

$$f_\mu = 1.0 - \exp(-0.0115\, Re_\tau) \tag{2.40}$$

$$f_1 = 1.0 \tag{2.41}$$

$$f_2 = 1.0 - 0.22\exp\left[-\left(\frac{Re_t}{6}\right)^2\right] \tag{2.42}$$

Low-Reynolds Number Terms:

$$D = 2\mu\frac{k}{y^2} \tag{2.43}$$

$$E = -2\mu\frac{\hat{\varepsilon}}{y^2}\exp(-0.5Re_\tau) \tag{2.44}$$

In the equations shown above, $Re_t = k^2/\nu\hat{\varepsilon}$ and $Re_\tau = y^+ = yu_\tau/\nu$.

Launder and Sharma [1974] developed a two-equation turbulence model from the low-Reynolds number turbulence model proposed by Jones and Launder [1972]. The TKE and TDR equations used by Launder and Sharma are of the form defined by equations (2.19) and (2.20), with the empirical constants, damping functions, and extra terms defined as follows.

Empirical Constants:

$$C_1 = 1.44 \tag{2.45}$$

$$C_2 = 1.92 \tag{2.46}$$

$$C_\mu = 0.09 \tag{2.47}$$

$$\sigma_k = 1.0 \tag{2.48}$$

$$\sigma_\varepsilon = 1.3 \tag{2.49}$$

Damping functions:

$$f_\mu = \exp\left[\frac{-3.4}{(1 + Re_t/50)^2}\right] \tag{2.50}$$

$$f_1 = 1.0 \tag{2.51}$$

$$f_2 = 1.0 - 0.3\exp\left[-Re_t^2\right] \tag{2.52}$$

Low-Reynolds Number Terms:

$$D = 2\mu\left(\frac{\partial\sqrt{k}}{\partial y}\right)^2 \tag{2.53}$$

$$E = 2\mu\nu_t\left(\frac{\partial^2 U}{\partial y^2}\right)^2 \tag{2.54}$$

2.6 Transition Models

This section presents an outline of the proposed transition models of Schmidt [1987] and Johnson [1987] that are examined in this thesis. As numerical calculations are marched downstream, TKE is convected and diffused into the boundary layer from the freestream. As the calculations proceed, the production term for the TKE equation ($P_k = \mu_t(\partial U/\partial Y)^2$) becomes significant and in turn increases the local value of TKE. With an increase in TKE, the turbulent viscosity (μ_t) begins to increase (see equation 2.17), which in turn increases P_k, which in

turn feeds the process even more. This nonlinear increase in TKE continues until the laminar boundary layer "naturally transitions" to a fully turbulent boundary layer. The transition process is initially controlled by the diffusion of TKE into the boundary layer from the freestream. This diffusion process may explain why two-equation turbulence models do not predict transition for low freestream turbulence intensity levels, as discussed by Launder and Spalding [1974]. It appears that the diffusion of TKE into the boundary layer and the nonlinear source terms of the TKE and TDR equations are the driving force for transition. These observations lead Schmidt to examine ways to modify the behavior of the production term of the TKE equation during the simulated transition process in order to improve predictions. The slight differences in the two proposed transition models are enhanced by examining the governing transition model equations.

Schmidt proposed a method of simulating transition by controlling the growth rate of TKE in the boundary layer. He felt that the process by which small disturbances are amplified in an unstable boundary layer is time dependent, while the governing equations are in steady state form. The time scale for the production modification would simply be related to the local convective velocity. The proposed PTM model Schmidt developed to control transition is

$$\left[\frac{\partial P_k}{\partial t}\right]_{max} = A^*P_k + B \,, \tag{2.55}$$

where A and B are empirical parameters.

The idea of using two independent parameters in Schmidt's model was to control the start and end of transition. Equation (2.55) can be converted from a time derivative form into a spatial derivative, for use in a boundary layer code, by using the local convective velocity as follows

$$\Delta P_{k,max} = (A^*P_{k,old} + B)\frac{dx}{U} \,, \tag{2.56}$$

where $\Delta P_{k,max}$ is the the maximum allowable change in the production of TKE at the current integration step, $P_{k,old}$ is the level of production of k from the previous integration step, dx is the the integration step size, and U is the local convective velocity at the y-location in the boundary layer.

A detailed outline of the numerical implementation of Schmidt's transition model is not outlined here (for details see Schmidt, 1987) but essentially the model compares ($P_{k,new}$ - $P_{k,old}$) to $\Delta P_{k,max}$ at each computational grid point, then uses the minimum value to calculate $P_{k,new}$ at each point. In examining the model form of the TKE and TDR transport equations, it is noted that the production of dissipation term in equation (2.20) is proportional to the production of TKE term in equation (2.19). Schmidt did not modify the production of TKE term in the TDR transport equation. The empirical constants, A and B, were determined through a set of calibration tests designed to isolate the effects of the PTM model from the effects of the diffusion of freestream TKE. Schmidt provides the calibrated curves for A and B as a function of freestream turbulence intensity for use with the Lam and Bremhorst [1981] and Launder and Sharma [1974] two-equation turbulence models. Schmidt calibrated the A and B curves by adjusting these constants until numerically predicted start and end of transition agreed with the correlations of Abu-Ghannam and Shaw [1980].

Johnson [1987] proposed a method similar to Schmidt to numerically predict transitional flow. Johnson believed the amplification of small disturbances in an unstable boundary is spatially dependent. The method proposed by Johnson for controlling the growth rate of TKE and thus controlling the transition process is

$$\left[\frac{\partial P_k}{\partial x}\right]_{max} = \alpha * P_k \, . \qquad (2.57)$$

From equation (2.57), the maximum change in P_k allowed by the transition model becomes

$$\Delta P_{k,max} = (\alpha^* P_{k,old})\, dx \,. \tag{2.58}$$

The numerical implementation of equation (2.58) is similar to the method used by Schmidt. Johnson used the experimental flat plate zero pressure gradient data of Blair and Werle [1980] to calibrate the empirical constant, α, to match the experimental transition data. Johnson presents a calibration curve for α as a function of freestream turbulence intensity for the K. Y. Chien two-equation model. In the process of further evaluating the performance of Johnson's transition model, several errors were found in the implementation of the original model, which lead to a variation of Johnson's transition model.

The University of Texas transition model uses the theme of Johnson's transition model in conjunction with Schmidt's numerical scheme for calculating the growth rate of TKE. The University of Texas proposed transition model is

$$\left[\frac{\partial P_k}{\partial x}\right]_{max} = \alpha^* P_k + \beta \tag{2.59}$$

where α and β are empirical parameters. In early investigations of Johnson's transition model, it was determined that the β constant is needed in an attempt to adequately control the end of transition. The maximum change in the production of TKE for each computational grid point becomes

$$\Delta P_{k,max} = \left(\alpha^* P_{k,old} + \beta\right) dx \,. \tag{2.60}$$

Again, the implementation of equation (2.60) is similar to the method used by Schmidt.

As mentioned in Chapter 1, the goal of this thesis was to assess the transition prediction capabilities of Schmidt's transition model (equation 2.55) and The

University of Texas transition model (equation 2.59) when used in conjunction with the K. Y. Chien turbulence model. It was hoped that a comparison of the these two transition models against various experimental transition data sets would detail the prediction capability of a temporally or spatially based transition model, focusing on the effect the local convective velocity (see equation 2.56) has on the modeling of the transition process. However, as discussed in Chapter 4, a problem associated with the K. Y. Chien model for low-Reynolds number flows was identified while examining the transition prediction capabilities of Schmidt's transition model. Therefore, due to the low-Reynolds number problem with the K. Y. Chien model, the transition prediction capabilities of The University of Texas transition model are not detailed in this thesis.

Chapter 3

Initial and Boundary Conditions

3.0 Introduction

The partial differential equations describing boundary layer flows are parabolic, which means the downstream transport properties are dependent, at most, on the values of the upstream transport properties. The required conditions to solve a set of parabolic equations are initial profiles for each dependent variable for all y at a specified x-location and boundary conditions at two positions in space for each dependent variable at all x greater than or equal to the initial x-location. The solution of parabolic equations is often carried out using a finite difference "marching technique" where the solution starts at the initial x-location, i.e. the location of the initial profiles, and marches forward in space. Figure 3.1 is an example of the extent of the computational domain defined for a boundary layer flow. The solution accuracy for a set of parabolic equations depends on the initial and boundary conditions.

The initial profiles and boundary conditions defining a valid solution are generated by a computer code called TEXIPBC, developed as part of this thesis, to calculate initial profiles and boundary conditions, for laminar or turbulent boundary layer flows, which are in turn used as input data to TEXSTAN. This chapter details the method used by TEXIPBC to calculate proper initial and boundary conditions to model transitional boundary layer flows.

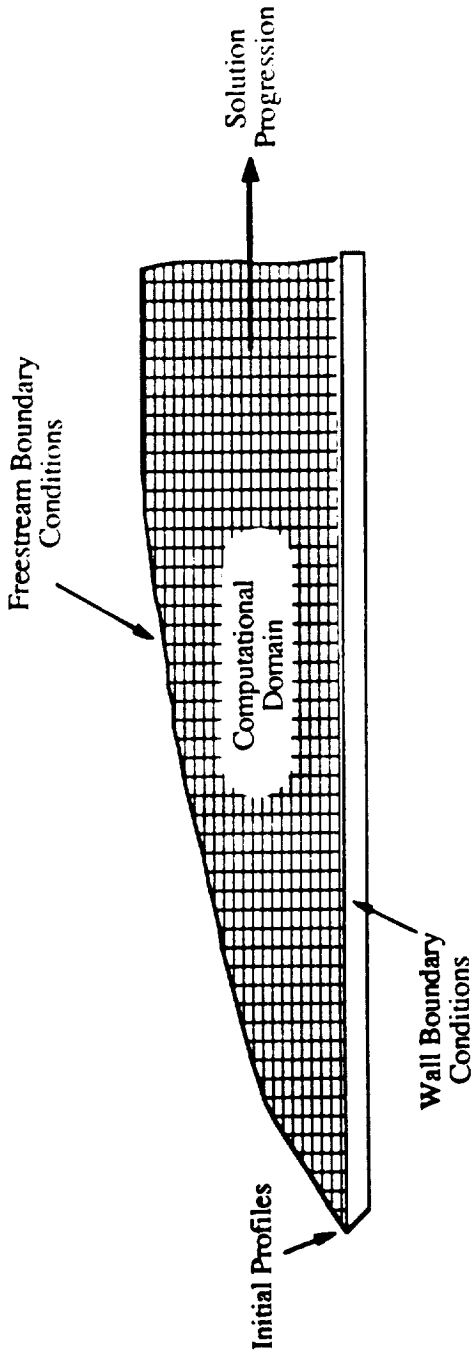

Figure 3.1. Defined computational domain for the numerical solution of parabolic differential equations.

3.1 Initial Profiles

The dependent variables calculated by TEXSTAN are the streamwise velocity (U), the stagnation enthalpy (I^*), the turbulent kinetic energy (k), and the turbulent dissipation rate ($\hat{\epsilon}$). Well-posed initial profiles are essential to assure accurate results near the starting x-location. If incorrect initial profiles are implemented, a solution to the governing equations generally results in an evolution of the profiles into a form that is compatible with the equations and the boundary conditions. However, until the profiles are corrected, the wall shear and heat transfer results will be inaccurate. Furthermore, the profiles that evolve may be significantly different in thickness than were originally specified. This leads to a boundary layer solution to a flow with a different momentum Reynolds number than initially specified. This section defines the method used by TEXIPBC to generate appropriate initial profiles for the dependent variables. As will be shown, the specification of initial profiles for U and I^* are well documented while the profiles for k and $\hat{\epsilon}$ require physical arguments.

3.1.1 Velocity Profiles

If a low-Reynolds number flow flow is considered laminar, the initial velocity profile will be a laminar velocity profile. Consider steady flow without turbulence over a semi-infinite flat plate aligned with the flow, with a constant freestream velocity, U_e, and constant fluid properties. Equations (2.11) and (2.14) may be rewritten as

$$\frac{\partial U}{\partial x} + \frac{\partial V}{\partial y} = 0 \tag{3.1}$$

and

$$U\frac{\partial U}{\partial x} + V\frac{\partial U}{\partial y} = \nu\frac{\partial^2 U}{\partial y^2} - \frac{1}{\rho}\frac{dP}{dx}\,. \tag{3.2}$$

The pressure gradient term of equation (3.2) is expressed in terms of the freestream velocity gradient by examining Euler's equation for flow along a streamline

$$\frac{dP}{\rho_e} = -d\left(\frac{U_e^2}{2}\right). \tag{3.3}$$

Differentiating equation (3.3) with respect to x leads to

$$\frac{dP}{dx} = -\rho_e U_e \frac{dU_e}{dx}. \tag{3.4}$$

The freestream velocity is assumed constant over a flat plate, $dU_e/dx = 0$; therefore equation (3.4) reduces to

$$\frac{dP}{dx} = 0. \tag{3.5}$$

Combining equations (3.5) and (3.2), the momentum equation is rewritten as

$$U\frac{\partial U}{\partial x} + V\frac{\partial U}{\partial y} = \nu\frac{\partial^2 U}{\partial y^2}. \tag{3.6}$$

The boundary conditions for equation (3.1) and (3.6) are

wall boundary condition for U: $U(x,y=0) = 0.0,$ (3.7)

wall boundary condition for V: $V(x,y=0) = 0.0,$ (3.8)

freestream boundary condition for U: $U(x,y\rightarrow\infty) = U_e(x),$ (3.9)

One approach to solving equations (3.1) and (3.6) is to use a similarity transformation which reduces the given partial differential equations to ordinary differential equations that are easier to solve. The use of a similarity parameter implies that the velocity profiles at all x-positions are geometrically similar, differing only by a multiplying factor in the y-direction. One similarity transformation used frequently for boundary layer flows utilizes the Blasius similarity variable

$$\eta = \frac{y\sqrt{U_e}}{\sqrt{2\nu x}} . \tag{3.10}$$

The similarity transformation of equations (3.1) and (3.6) yields the Blasius equation (detailed in Kays and Crawford, 1980), where the prime denotes differentiation with respect to η

$$f''' + ff'' = 0 , \tag{3.11}$$

where, $f''(\eta)$ is the nondimensional wall shear stress; $f'(\eta)$ is the nondimensional velocity; and $f(\eta)$ is the nondimensional stream function. The boundary conditions (3.7) to (3.9) are transformed to

$$f(\eta=0) = 0 , \tag{3.12}$$

$$f'(\eta=0) = 0 , \tag{3.13}$$

$$f'(\eta=\infty) = 1 . \tag{3.14}$$

There is no analytical solution to the Blasius equation, but it may be solved numerically. Using the Runge-Kutta routine provided by White [1974], equation (3.11) is solved in TEXIPBC to provide an initial laminar velocity profile.

In the stagnation-point region, such as for cylinders in cross-flow and turbine blades, and equations (3.1) and (3.2) govern the flow field since the pressure gradient is no longer zero. A Falkner-Skan similarity transformation may be used to transform the partial differential equations of (3.1) and (3.2) into the following ordinary differential equation

$$f''' + ff'' + (1 - f'^2) = 0 . \tag{3.15}$$

Equation (3.15) is subject to the same boundary conditions (equations 3.12 to 3.14) as equation (3.11). TEXIPBC may be used to calculate the initial velocity profile for either a flat plate geometry (equation 3.11) or for a turbine airfoil geometry (equation 3.15).

3.1.2 Stagnation Enthalpy Profiles

The initial stagnation enthalpy profile is based on a direct extension of the similarity solution for velocity profiles. Assume steady flow without turbulence over a semi-infinite flat plate with constant freestream velocity, constant fluid properties, and constant plate surface temperature. A constant plate surface temperature means the thermal boundary layer will develop along with the momentum boundary layer from the leading edge of the plate. The stagnation enthalpy is nondimensionalized as follows to aid in the analysis of the thermal boundary layer

$$\tau = \frac{I^*(x,y) - I^*_w(x,y)}{I^*_e(x,y) - I^*_w(x,y)} , \tag{3.16}$$

where τ is the nondimensional stagnation enthalpy distribution.

The governing equation for stagnation enthalpy neglecting turbulence fluctuations and viscous dissipation is written as follows from equation (2.27)

$$U\frac{\partial I^*}{\partial x} + V\frac{\partial I^*}{\partial y} = \alpha\frac{\partial^2 I^*}{\partial y^2}. \qquad (3.17)$$

Equation (3.17) may be written in nondimensional form using equation (3.16),

$$U\frac{\partial \tau}{\partial x} + V\frac{\partial \tau}{\partial y} = \alpha\frac{\partial^2 \tau}{\partial y^2}. \qquad (3.18)$$

Equation (3.18) is the nondimensional stagnation enthalpy governing equation. Assuming temperature prescribed boundaries, the boundary conditions for equation (3.18) are

$$\text{wall boundary condition for } \tau: \quad \tau(x,y=0) = 0, \qquad (3.19)$$

$$\text{freestream boundary condition for } \tau: \quad \tau(x,y\rightarrow\infty) = 1. \qquad (3.20)$$

Equation (3.18) is similar to equation (3.6), which is the hydrodynamic equivalent to this problem. A similarity transformation for equation (3.18) is developed using the Blasius similarity variable (equation 3.10) and the stream function, Ψ (for details see Kays and Crawford, 1980). After performing the required steps, the transformed nondimensional stagnation enthalpy equation may be expressed as (the primes denote differentiation with respect to η)

$$\tau'' + \mathrm{Pr}\, f\, \tau' = 0, \qquad (3.21)$$

where τ' is the nondimensional temperature gradient, f is the nondimensional stream function, and Pr is the molecular Prandtl number. Equation (3.21) is the ordinary differential equation reduced from the partial differential equation (3.18), which is

the goal of a similarity transformation. The boundary conditions for equation (3.21) are

$$\tau(\eta=0) = 0 , \tag{3.22}$$

$$\tau(\eta=\infty) = 1 . \tag{3.23}$$

To specify the initial stagnation enthalpy profile, equation (3.21) is solved by TEXIPBC using the same Runge-Kutta subroutine developed to calculate the initial velocity profile.

3.1.3 Turbulent Kinetic Energy Profiles

A difficult task in calculating transitional flows is the specification of TKE profiles. There is virtually no experimental data available that details the TKE profile in the presence of high freestream turbulence [Rodi and Scheuerer, 1985a]. Due to the lack of information, most TKE profiles are developed on an ad hoc basis. There are some constraints, however, that the TKE profile must abide by:

(1) The TKE must vanish at the wall (i.e. when y = 0).

(2) The TKE profile must increase as y^2 in the near-wall region based on an asymptotic expansion of the fluctuating velocity components [Patel, et al., 1985].

(3) The TKE profile must asymptotically approach the freestream value of TKE at the boundary layer edge.

With these few constraints, adequate initial TKE profiles can be calculated.

One method for defining a TKE profile which meets all of the above criteria was proposed by Rodi and Scheuerer [1985a, 1985b], which is of the form

$$k(\eta) = k_e \left(\frac{U}{U_e}\right)^2 = k_e (f')^2 \tag{3.24}$$

where,

$$k_e = 1.5 (Tu_e U_e)^2 . \tag{3.25}$$

It is easily seen how equation (3.24) may be used with a Blasius solution to generate a simple TKE profile. From equation (3.24), it is evident that the TKE profile proposed by Rodi and Scheuerer is a monotonic increasing profile. Figure 3.2 shows an example of a general TKE profile generated by equation (3.24). Figure 3.3 demonstrates how the governing equations alter the TKE profile specified by Rodi and Scheuerer's method as soon as the calculations are started. In Figure 3.3, the scaling parameter k/k_{max} has been used to examine the overall shape of the TKE profiles. The change in the TKE profile, in Figure 3.3, from $Re_m = 3.1$ to $Re_m = 20.1$ implies the initial TKE profile is not in "equilibrium" with the specified velocity and TDR profiles as well as the finite-difference form of the K. Y. Chien turbulence model. The change in the initial TKE profile suggests a different method to calculate initial TKE profiles could be used.

An alternate method for creating initial TKE profiles has been proposed by Reshotko [1988] that meets all the required criteria. The initial TKE profile proposed by Reshotko contains a distinct peak in the profile near the wall with an asymptotic trend to the freestream TKE value at the boundary layer edge. The Reshotko TKE profile (see Appendix B for derivation) is defined as

$$k(\eta) = k_e \left[f' + 0.5\eta f''\right]^2 . \tag{3.26}$$

where f' and f'' are defined for a Blasius solution. Figure 3.4 shows a comparison of the Reshotko TKE profile with the Rodi and Scheuerer TKE profile under the same flow conditions. The initial condition criteria stated by Reshotko to define the starting location for the TKE profile is

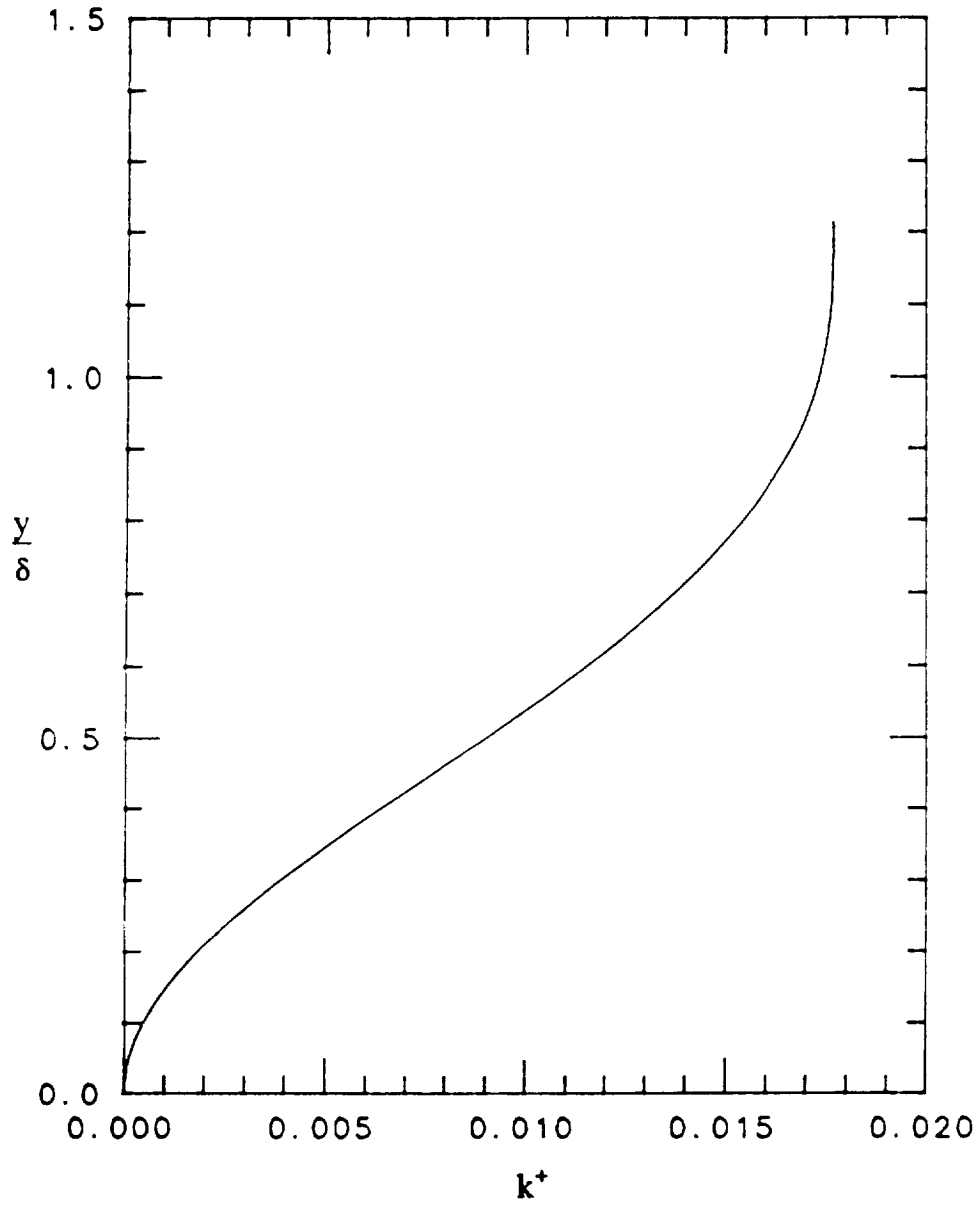

Figure 3.2. Turbulent kinetic energy initial profile based on the method of Rodi and Scheuerer [1985a].

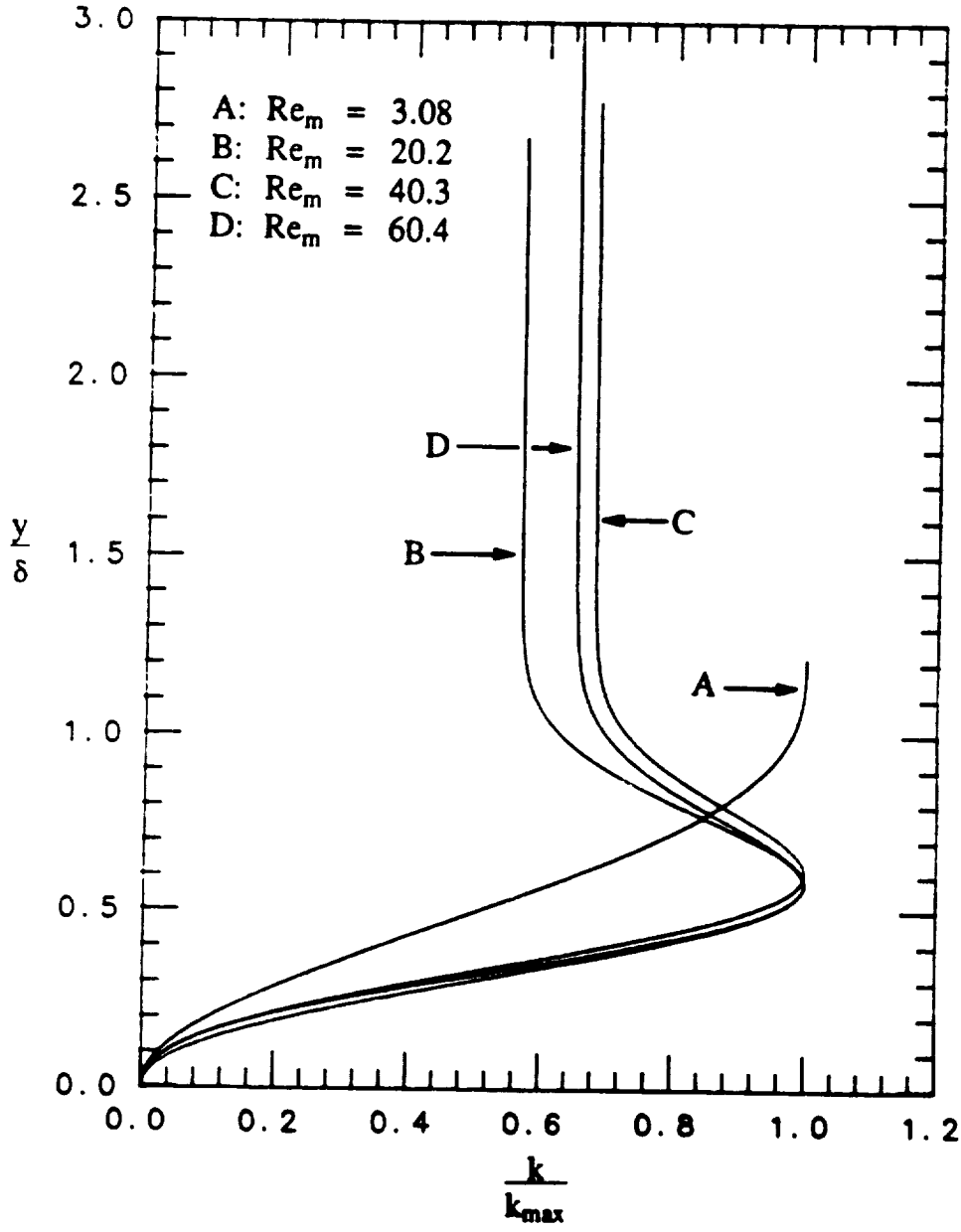

Figure 3.3. Developing turbulent kinetic energy profiles at various momentum Reynolds numbers after the initial profile of Rodi and Scheuerer [1985a].

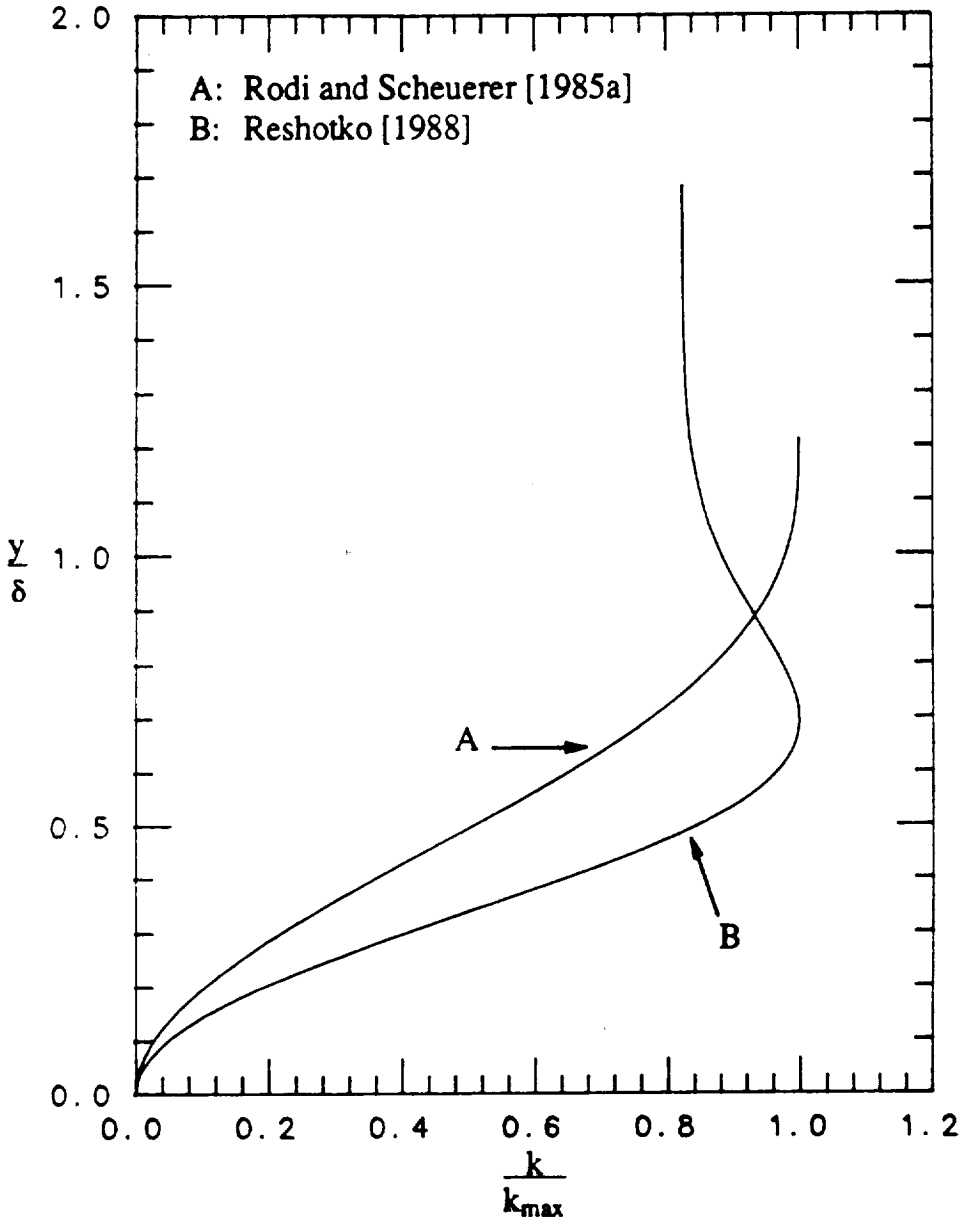

Figure 3.4. Comparison of the Reshotko [1988] initial turbulent kinetic profile to the initial turbulent kinetic energy profile of Rodi and Scheuerer [1985a].

$$Re_x \leq \frac{0.01}{(Tu)^2} . \tag{3.27}$$

Figure 3.5 shows how TKE profiles evolve from the initial TKE profile generated by equation (3.26). Comparing Figures 3.5 and 3.3, demonstrates how the finite-difference solution alters the initial Reshotko TKE profile as compared to the initial Rodi and Scheuerer TKE profile. For the first two profile locations of Figure 3.5 (Re_m = 2.1 and Re_m = 20.3), the Reshotko initial profile does not appear to be altered as much as the Rodi and Scheuerer initial profile. The Reshotko TKE profile appears to be in "equilibrium" with the other dependent profiles as well as the finite-difference equations of the K. Y. Chien turbulence model. Equation (3.26) was incorporated in the Runge-Kutta routine of TEXIPBC to calculate initial TKE profiles.

Examining initial TKE profiles demonstrates that an initial TKE profile that matches the numerical behavior of a K. Y. Chien turbulence model does match the numerical behavior of a Jones and Launder [1972, 1973] type turbulence model at low-Reynolds numbers. For example, the Reshotko TKE profiles used in this study for the K. Y. Chien turbulence model were not numerically compatible with the Launder and Sharma [1974] turbulence model, a derivative of the Jones and Launder [1972, 1973] turbulence model. Instead, the Rodi and Scheuerer initial TKE profiles were more in agreement with the numerics of the Launder and Sharma turbulence model. Therefore, the behavior of the damping functions and the low-Reynolds number terms of any two-equation turbulence model at low-Reynolds numbers dictate the form that the initial TKE profile will assume. Whether the evolved form of TKE profile, subject to the particular turbulence model being used, is correct or not is subject to debate.

One source of information concerning developing turbulent profiles, specifically TKE profiles, is the study of turbulized laminar flow. A developing flat plate boundary layer in the presence of high freestream turbulence levels can be

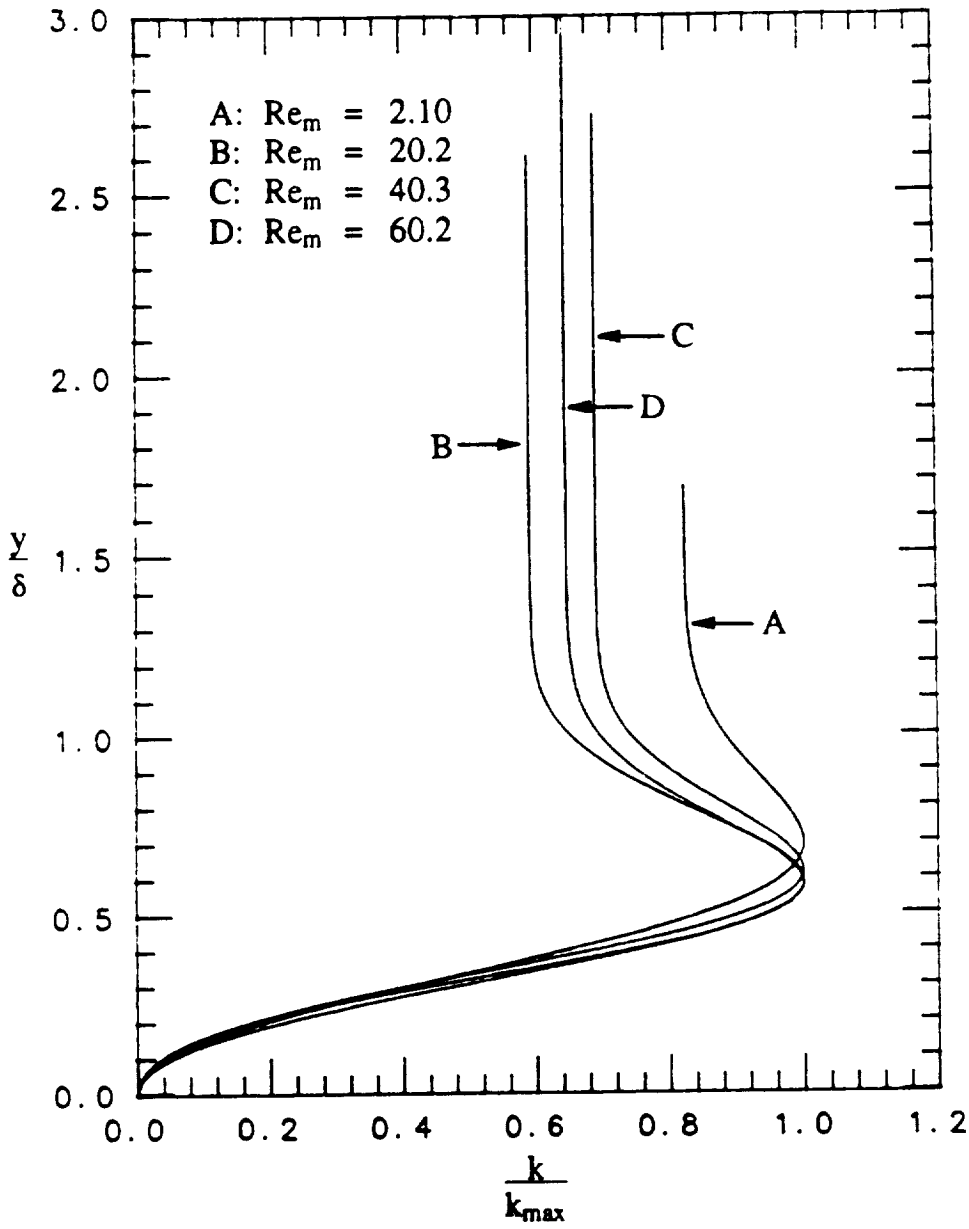

Figure 3.5. Developing turbulent kinetic energy profiles at various momentum Reynolds numbers after the initial profile of Reshotko [1988].

termed "pseudo - laminar", since it differs both from the purely laminar layer and from the turbulent layer at low turbulence [Dyban, et al., 1976]. This "pseudo - laminar" layer is turbulized by the penetration of freestream turbulence into the boundary layer. From research conducted on turbulized laminar boundary layers (Dyban, et al., 1976, Dyban and Epik 1978, and Motulevich, et al., 1984), it is noted that the TKE profile for a turbulized boundary layer does not monotonic increase as shown by the Rodi and Scheuerer TKE profile. Instead the TKE profile has a distinct peak in the profile near the wall and an asymptotic trend to the freestream TKE value at the boundary layer edge like the Reshotko TKE profile. Research into the turbulized laminar boundary layers may provide information that leads to new forms of damping functions and low-Reynolds number terms for two-equation turbulence models to obtain "physically" correct turbulent profiles at low-Reynolds numbers.

3.1.4 Turbulent Dissipation Rate Profiles

Experimental data for calculating a TDR profile does not exist; therefore, more flexibility exists for defining (or misdefining) the initial TDR profile. As with the TKE profile, the TDR profile also has some constraints that must be met before the profile is considered valid.

(1) The TDR profile must asymptotically approach the freestream value of TDR at the boundary layer edge.

(2) Near the wall, the TDR profile must be proportional to y^2 [Patel, et al., 1985] for the K. Y. Chien turbulence model.

The initial TDR profile used in this study assumes the dissipation rate is proportional to the production rate of TKE, as proposed by Rodi and Scheuerer and others

$$\hat{\varepsilon}(\eta) = a_1 k \frac{\partial U}{\partial y}, \tag{3.28}$$

where a_1 is a turbulence structural coefficient, $-\overline{u'v'}/k$. The $\hat{\varepsilon}$-values described by equation (3.28) approach zero at the boundary layer edge; therefore, an additional equation was imposed by Rodi and Scheuerer,

$$\hat{\varepsilon} > \hat{\varepsilon}_e \tag{3.29}$$

where

$$\hat{\varepsilon}_e = \frac{k_e^{1.5}}{L_e}. \tag{3.30}$$

This condition insures that the length scale at any location within the boundary layer does not exceed the freestream length scale, L_e.

Figure 3.6 shows an example of a general TDR profile generated by equation (3.28). In using equation (3.28) in TEXIPBC it was noted that large gradients in $\hat{\varepsilon}$ near the freestream are calculated for certain combinations of $\hat{\varepsilon}_e$ and a_1, namely for a small value of $\hat{\varepsilon}_e$ coupled with a moderate to large value for a_1. Freestream gradients should be avoided for initial profiles because it signifies the edge of that boundary layer has not been properly located. The TKE and TDR shear layer thicknesses are constrained initially to the velocity boundary layer thickness (δ) because δ is the only known shear layer thickness at the start of the calculations.

In summary, equation (3.28) is used from the wall to the peak in the TDR profile, but, to eliminate the creation of freestream gradients, a cubic polynomial was fit between the peak to the freestream TDR level. The cubic polynomials fit both magnitude ($\hat{\varepsilon}_e$ and $\hat{\varepsilon}_{max}$) and slope (zero slope conditions) at both ends of the domain. Figure 3.7 shows, as a comparison, the initial TDR profile calculated from equation (3.28) with and without the cubic polynomial fit to eliminate the freestream gradient for small $\hat{\varepsilon}_e$. Figure 3.8 shows that TEXSTAN does not alter the initial TDR profiles for $y/\delta < 0.5$, however; for $y/\delta > 0.5$ the TDR profile is

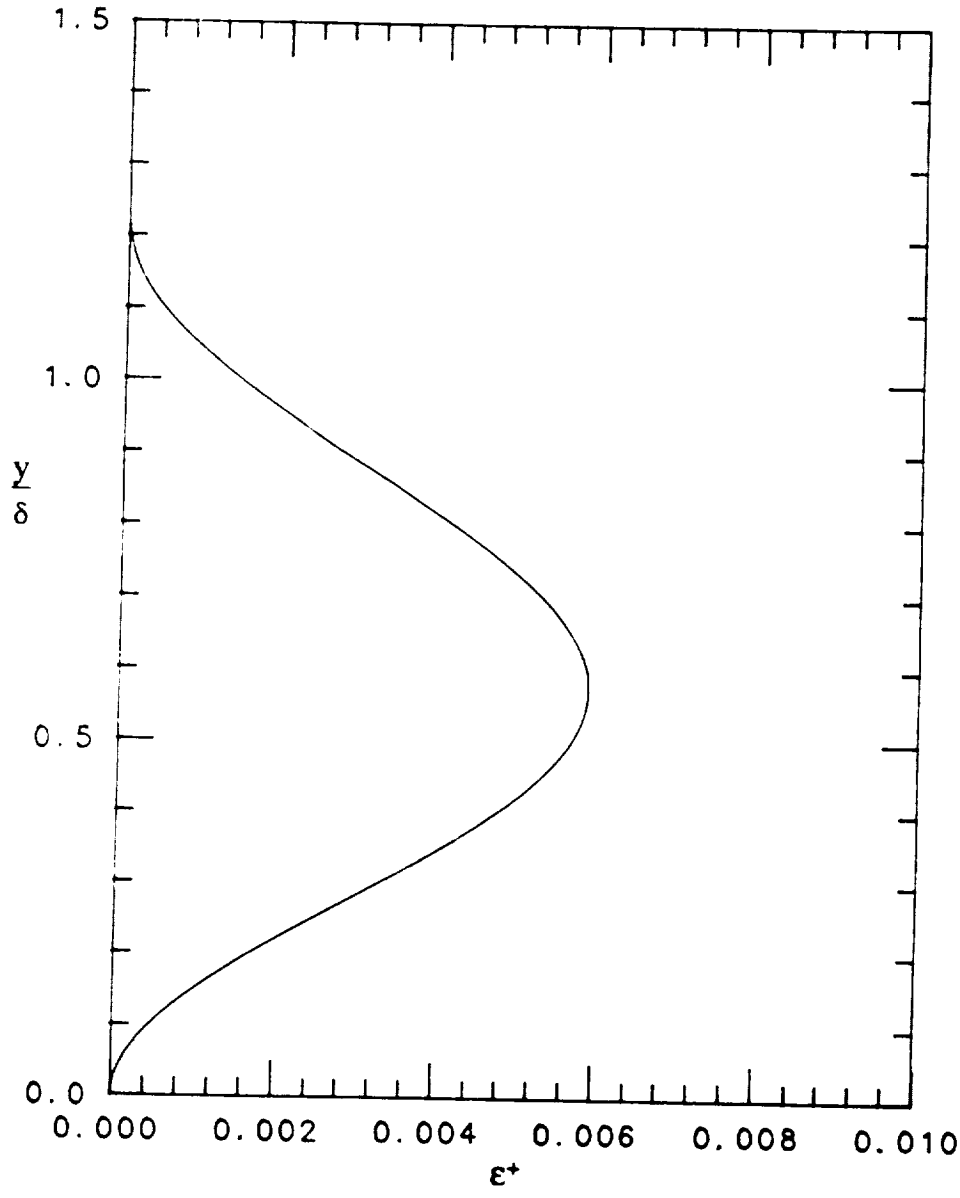

Figure 3.6. Turbulent dissipation rate profile based on the method of Rodi and Scheuerer [1985a].

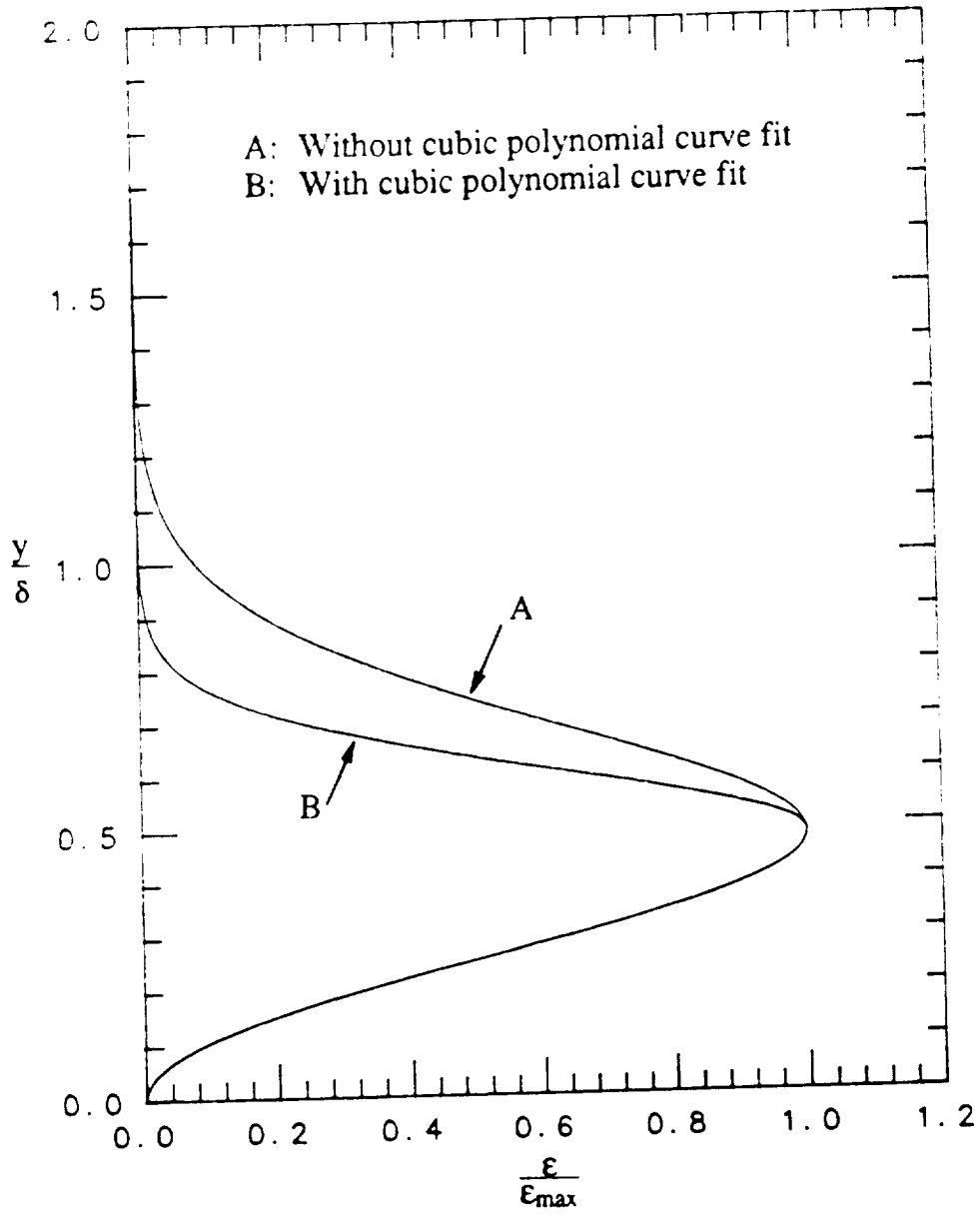

Figure 3.7. Comparison of Rodi and Scheuerer [1985a] initial turbulent dissipation rate profiles with and without a cubic polynomial curve fit to eliminate freestream gradients.

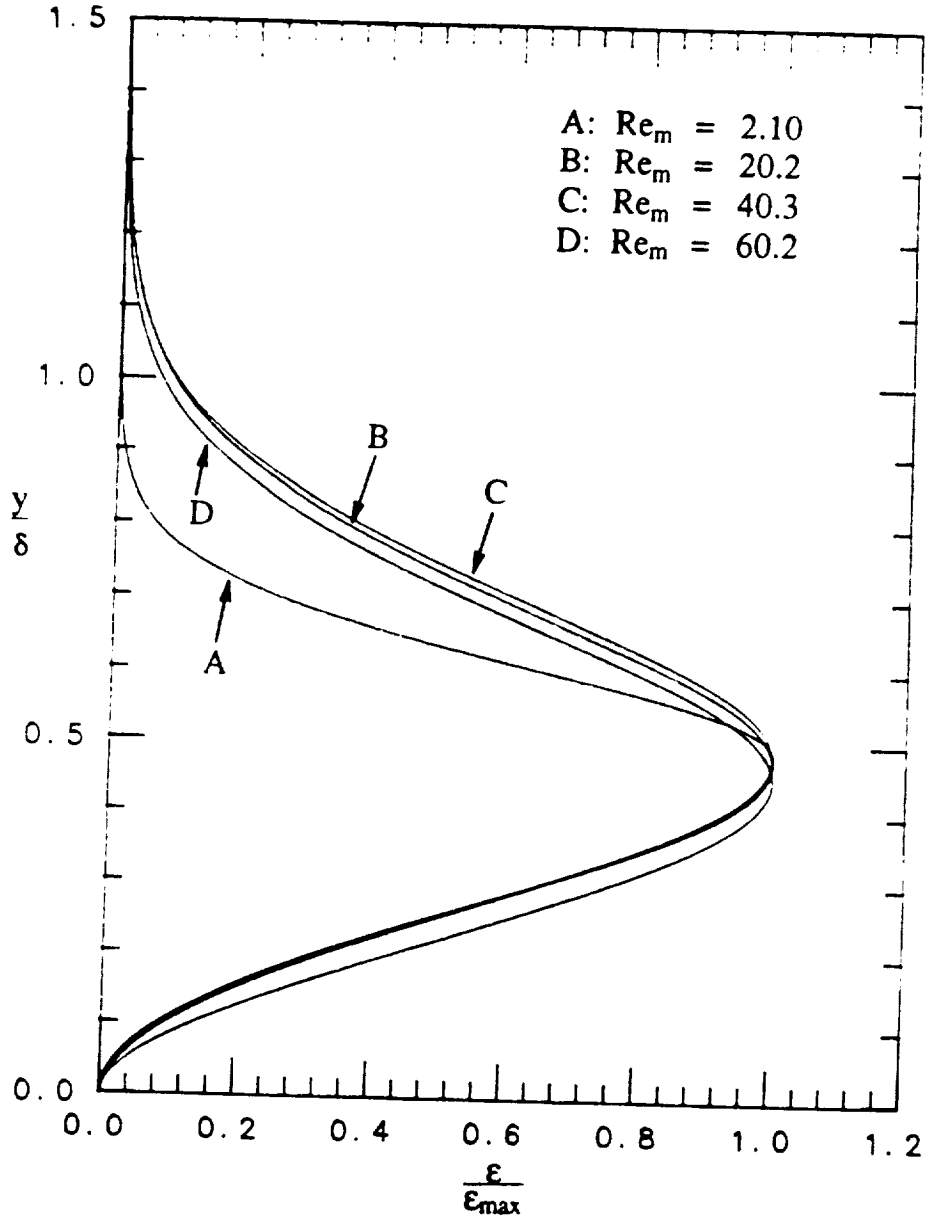

Figure 3.8. Developing turbulent dissipation rate profiles at various momentum Reynolds numbers after the initial profile of Rodi and Scheuerer [1985a] with a cubic polynomial curve fit.

modified since the shear layer thickness for the TDR profile is different than the velocity shear layer thickness. Equations (3.28), equation (3.29), and the cubic polynomial fit are used in TEXIPBC to calculate TDR initial profiles.

3.2 Boundary Conditions

The solution to a set of parabolic equations depends on the boundary conditions at the wall and the freestream locations. As with the initial profiles, boundary conditions must be defined for each of the dependent variables. For TEXSTAN, each of the dependent variable boundary conditions have different effects on the developing boundary layer. The freestream velocity boundary condition defines the freestream pressure gradient, affecting the growth of the boundary layer. The freestream stagnation enthalpy boundary condition is a source for heat transfer between the freestream and the wall. The freestream TKE and TDR boundary conditions define the freestream turbulence affects on the boundary layer, especially in the laminar and transitional regions. This section outlines the methods used by TEXIPBC to calculate the various dependent variable boundary conditions.

3.2.1 Velocity Boundary Conditions

For boundary layer flows with a wall and freestream, the boundary conditions for the momentum equation, assuming no wall mass transfer, are defined by equations (3.7) to (3.9). The velocity boundary condition reduces to a problem of calculating $U_e(x)$. Numerical boundary layer codes typically can not use a raw experimental freestream velocity distribution as a boundary condition because small experimental errors in the discrete velocity measurements greatly influence the calculation of gradients. The importance of a smooth velocity distribution can not be overstated, even though the velocity distribution may appear smooth it does not guarantee the velocity gradient will be smooth. As shown in equation (3.4), the

pressure gradient used in the momentum equation may be expressed as a function of the freestream density, freestream velocity, and freestream velocity gradient. If the input velocity distribution is not smooth, then the velocity gradient calculation will introduce large errors in the pressure gradient calculation, which will affect the solution of the momentum equation.

If derivative values must be calculated, the use of a least-squares polynomial (or spline) fit is recommended to smooth the data before differentiating it [Carnahan, et al., 1969]. This method was used by the author in creating TEXIPBC. Input to TEXIPBC consists of some form of freestream data such as freestream velocity distribution, freestream Mach number distribution, freestream pressure distribution, or freestream pressure coefficient (Cp) distribution. The data, often called loading data, may be either raw experimental data or data from an inviscid Euler solution. The loading data is then processed through a least-squares cubic spline routine, called ICSVKU [IMSL, 1984], to obtain a smooth continuous distribution of loading data. The degree of smoothing of the loading data is a function of the number of knots selected by the user. A knot is a point between which two cubic polynomials are joined. At each knot location the function, its first derivative, and its second derivative are matched. Figure 3.9 shows the matching conditions at each knot location for a simulated spline curve.

The degree of smoothness and acceptable fit to the original data is a function of the number of knots selected and the judgement of the user. The more knots that are used the less smooth the final loading distribution becomes, and conversely, the fewer the knots used the smoother the resulting loading distribution becomes. Appendix C demonstrates the affect the number of knots has on the degree of smoothing for a given loading distribution. From the smoothed loading data, a smooth velocity distribution may be calculated using the far-field stagnation conditions and one-dimensional compressible gas equations. The final smoothed velocity distribution is then used by TEXSTAN as the freestream velocity boundary condition.

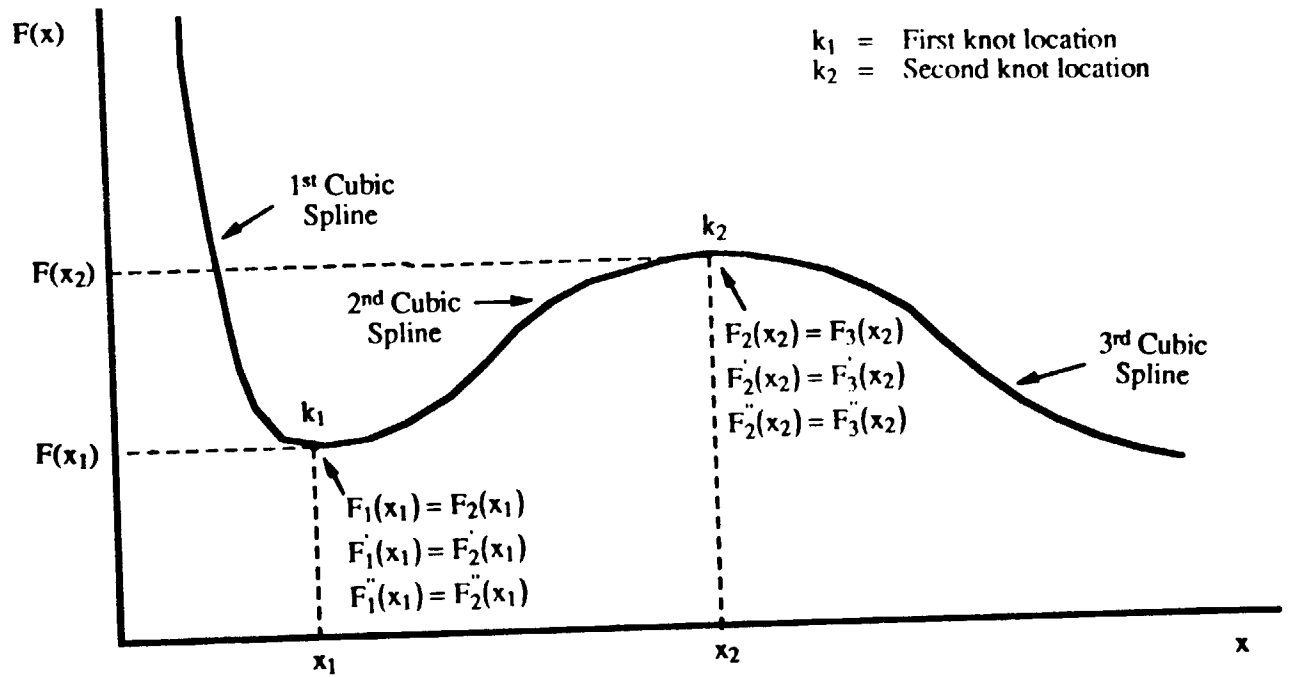

Figure 3.9. Matching conditions at knot locations for a cubic spline curve fit.

An added feature of TEXIPBC is its ability to calculate the pressure gradient in the same manner as TEXSTAN. The smoothed velocity distribution is processed through a "not-a-knot" spline which calculates the velocity gradient and resulting pressure gradient at each boundary condition location. This option in TEXIPBC allows the user to see approximately how TEXSTAN will calculate the pressure gradient without having to actually run TEXSTAN. The "not-a-knot" spline used in TEXIPBC and TEXSTAN requires the second derivative at each endpoint of the curve to be specified. Since, these derivatives are unknown, an extrapolation method is used to estimate the second derivative at the endpoints. This extrapolation method can lead to slight-to-moderate errors in the pressure gradient near the leading and trailing edge of the solution domain even though the input velocity distribution is smooth.

3.2.2 Stagnation Enthalpy Boundary Conditions

The boundary conditions for the stagnation enthalpy equation are as follows

wall boundary condition for I^*: $I^*(x,y=0) = I^*_w(x)$ (3.31)

or,

wall boundary condition for q": $q''(x,y=0) = -\frac{k}{c}\frac{\partial I^*(x,y=0)}{\partial y} = q''_w(x)$ (3.32)

and,

freestream boundary condition for I^*: $I^*(x,y\rightarrow\infty) = I^*_e(x) = \text{constant}$ (3.33)

The wall stagnation enthalpy level or wall heat flux are usually specified from experiment and as a result they are known quantities. The specification of the stagnation enthalpy boundary conditions reduces to a problem of calculating $I^*_e(x)$. The

far-field flow conditions (U_f, T_f, and P_f, etc.) for a given experiment are usually known. Therefore, the far-field static enthalpy is calculated via air property tables or assuming air is a calorically perfect gas and knowing the far-field temperature. From these variables the stagnation enthalpy of the flow can be calculated as

$$I_f^* = I_f + \frac{U_f^2}{2\, g_c\, c_J} = I_e^*(x)\,, \tag{3.34}$$

where g_c and c_J are the force-mass and work-energy conversion constants. By definition, the stagnation enthalpy is constant outside the boundary layer provided there is no entropy generation, i.e. no curved shock waves or chemical reactions in the flow. Hence, the freestream stagnation enthalpy boundary condition will be constant and equal to the far-field stagnation enthalpy. On the other hand, the freestream static enthalpy will change if the freestream velocity varies due to a change in the contour of the body.

3.2.3 Turbulent Kinetic Energy and Turbulent Dissipation Rate Boundary Conditions

The boundary conditions for the TKE and TDR governing equations for the K. Y. Chien two-equation turbulence model are as follows

wall boundary condition for TKE: $k(x,0) = 0.0$ (3.35)

freestream boundary condition for TKE: $k(x,\delta) = k_e(x)$ (3.36)

wall boundary condition for TDR: $\hat{\varepsilon}(x,0) = 0.0$ (3.37)

freestream boundary condition for TDR: $\hat{\varepsilon}(x,\delta) = \hat{\varepsilon}_e(x)$ (3.38)

Assuming all cross-stream gradients vanish as $y \rightarrow \infty$, the governing equations describing the TKE and TDR boundary conditions may be derived from equations (2.19) and (2.20) as follows

$$U_e \frac{dk_e}{dx} = - \hat{\varepsilon}_e - D , \tag{3.39}$$

$$U_e \frac{d\hat{\varepsilon}_e}{dx} = - C_2 f_2 \frac{\hat{\varepsilon}_e^2}{k_e} - E , \tag{3.40}$$

The D and E are the extra low-Reynolds number (LRN) terms defined by equations (2.43) and (2.44). Equations (3.39) and (3.40) are ordinary differential equations because the y-dependence of the variables has been eliminated at the freestream. Specifying k_e and $\hat{\varepsilon}_e$ at the initial boundary condition, i.e. $x = 0$, is sufficient to define k_e and $\hat{\varepsilon}_e$ at all subsequent x-locations by integrating equations (3.39) and (3.40). As a result, TEXSTAN does not require TKE and TDR to be specified at each x-location, instead, accurate initial values for TKE and TDR are the only requirement.

The freestream length scale for a turbulent boundary layer is defined by dimensional arguments as

$$L_e = \frac{k_e^{1.5}}{\hat{\varepsilon}_e} , \tag{3.41}$$

For grid generated turbulence, the freestream length scale should increase with increasing x-distance [Tennekes and Lumley, 1972]. Upon examining equation (3.39) and (3.40) a problem with calculating the freestream TKE and TDR boundary conditions for the K. Y. Chien two-equation turbulence model was discovered. Inserting equations (2.43) and (2.44) into equations (3.39) and (3.40) yields

$$U_e \frac{dk_e}{dx} = -\hat{\varepsilon}_e - 2\frac{\mu_e}{\rho_e}\frac{k_e}{y_e^2} \tag{3.42}$$

and

$$U_e \frac{d\hat{\varepsilon}_e}{dx} = -C_2 f_2 \frac{\hat{\varepsilon}_e^2}{k_e} - 2\mu_e \frac{\hat{\varepsilon}_e}{y_e^2} \exp(-0.5y_e^+) . \tag{3.43}$$

The second term on the right-hand side of both equations (3.42) and (3.43) contain $1/y_e^2$ factors. For transitional studies, the initial profiles are laminar, and as a result, the boundary layer thickness, $\delta = y_e$, is very small. Therefore, in equation (3.42), the LRN term tends to be on the same-order-of-magnitude as the freestream dissipation term. In equation (3.43), the LRN term is several orders-of-magnitude smaller than the freestream dissipation term and has a negligible effect. When equations (3.42) and (3.43) are integrated to obtain k_e and $\hat{\varepsilon}_e$ distributions, k_e tends to decay more rapidly than physically justified due to the affect of the LRN term. The resulting freestream length scale distribution will decrease rather than increase, contradicting the basic length scale behavior for grid generated turbulence. The freestream length scale will eventually increase but not until the flow has been fully turbulent for some distance. The length scale begins to increase because the turbulent boundary layer is thicker than a laminar boundary layer which results in a smaller $1/y_e^2$ factor and correspondingly a smaller LRN term in equation (3.42).

To correct the freestream length scale problem associated with the K. Y. Chien two-equation model, the LRN terms were ignored when calculating the freestream TKE and TDR boundary conditions. Neglecting the low-Reynolds number terms, the K. Y. Chien governing equations for the freestream TKE and TDR distributions become

$$U_e \frac{dk_e}{dx} = -\hat{\varepsilon}_e \tag{3.44}$$

and

$$U_e \frac{d\hat{\varepsilon}_e}{dx} = -C_2 f_2 \frac{\hat{\varepsilon}_e^2}{k_e} . \tag{3.45}$$

Equations (3.44) and (3.45) are not the true governing equations to calculate the freestream TKE and TDR distributions for the K. Y. Chien turbulence model. Therefore, by using equations (3.44) and (3.45) there is a possibility of introducing a discontinuity in the boundary layer length scale distribution. However, calculations for flat plate C_f distributions with and without the LRN terms in the freestream governing equation did not show any variations in the C_f predictions. A freestream discontinuity in the boundary layer length scale distribution does not effect the C_f predictions of TEXSTAN. The length scale distribution for these tests increased with increasing x-distance which demonstrates that the LRN terms in equations (3.42) and (3.43) are not physically realistic when applied at the freestream location. Equations (3.44) and (3.45) are the governing differential equations used in TEXSTAN to calculate the freestream TKE and TDR boundary conditions when using the K. Y. Chien two-equation turbulence model.

Figures 3.10 to 3.12 are plots of the K. Y. Chien turbulence model simulation of the decay of k_e and $\hat{\varepsilon}_e$ along with the freestream length scale, L_e, distribution for the grid 1 ($Tu_{e,i}$ = 1.3%), grid 2 ($Tu_{e,i}$ = 2.6%), and grid 3 ($Tu_{e,i}$ = 6.2%) freestream turbulence level distribution of Blair and Werle's [1980] experimental transition studies. Equations (3.44) and (3.45) were used to calculate the freestream TKE and TDR levels and equation (3.41) was used to calculate the freestream length scale. Figure 3.10 is a plot of k_e versus x for all three grid cases of Blair and Werle along with the numerical simulation for the decay of k_e. As shown in Figure 3.10, $k_{e,i}$ increases and the slope in the decay curve for k_e increases as the freestream turbulence level increases. Figure 3.11 is a plot of $\hat{\varepsilon}_e$ versus x for all three grid cases of Blair and Werle. Figure 3.11 shows how $\hat{\varepsilon}_{e,i}$ has a nonlinear increase as the freestream turbulence level is doubled. Figure 3.12 is a plot of L_e versus x for all three grid cases of Blair and Werle. As discussed before, the freestream length scale should increase as a function of x. Figure 3.12 shows that with the corrections made to equations (3.44) and (3.45) the freestream length scale distribution does increase with increasing x distance.

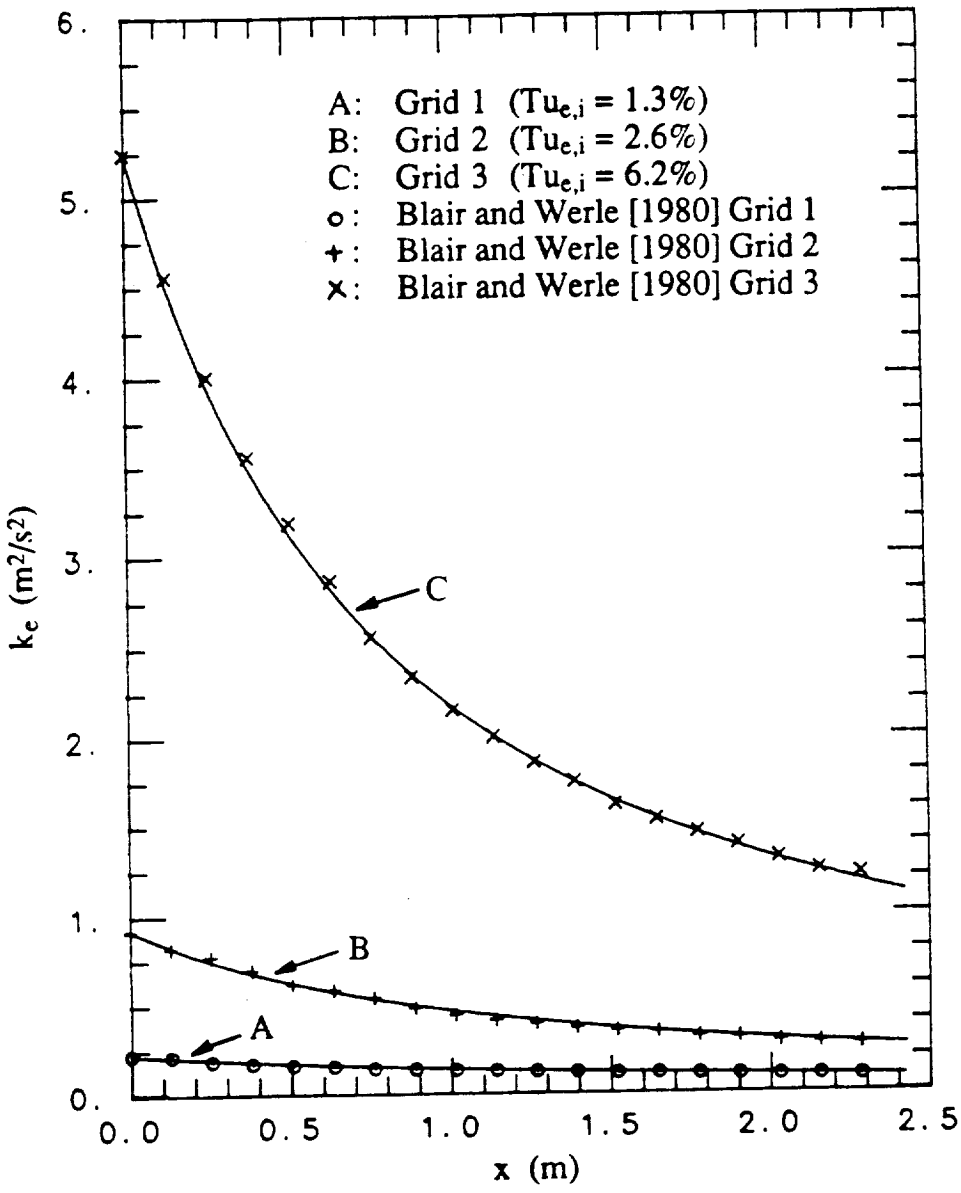

Figure 3.10. Freestream turbulent kinetic energy versus x-distance for the numerical simulation of Blair and Werle's [1980] freestream turbulence level distribution.

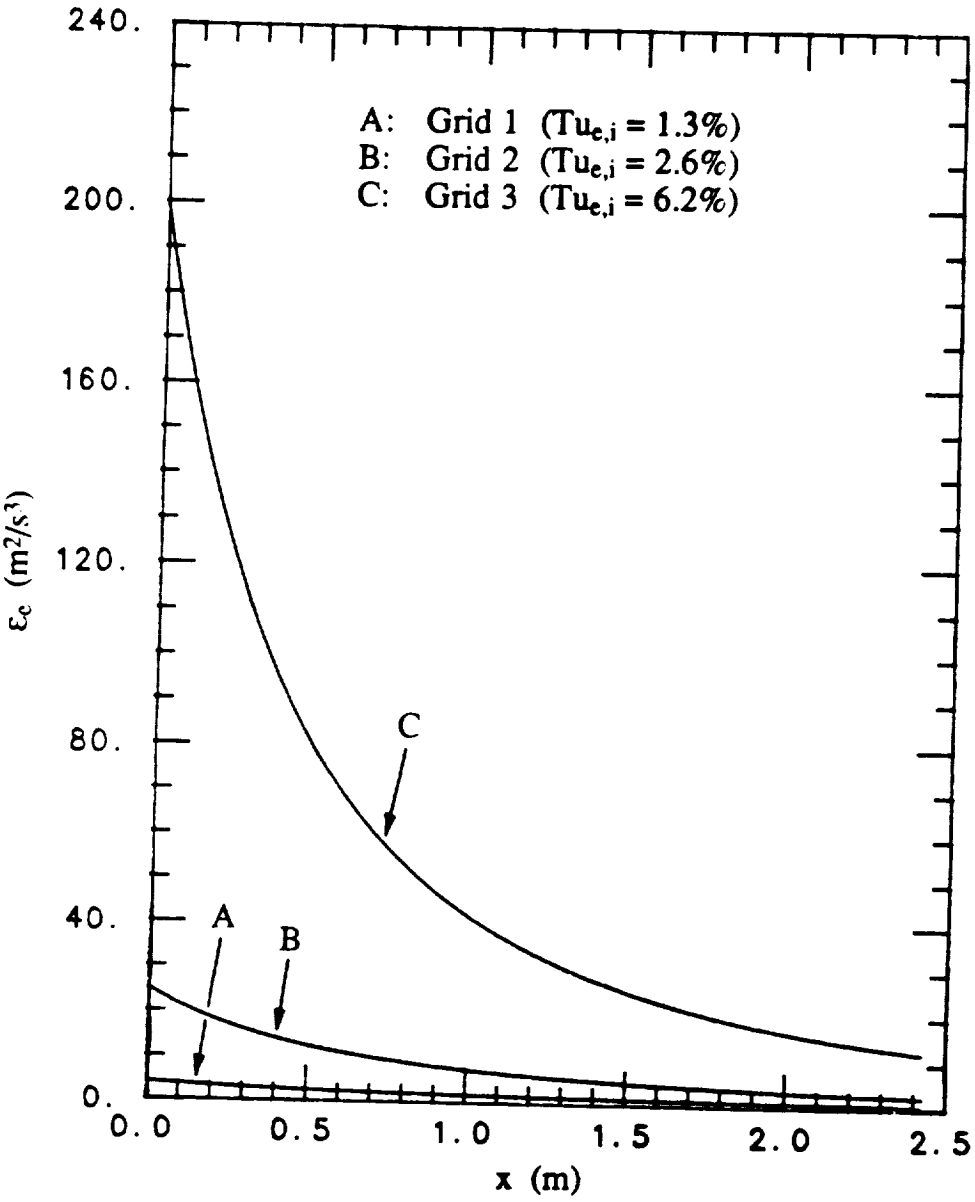

Figure 3.11. Freestream turbulent dissipation rate versus x-distance for the numerical simulation of Blair and Werle's [1980] freestream turbulence level distribution.

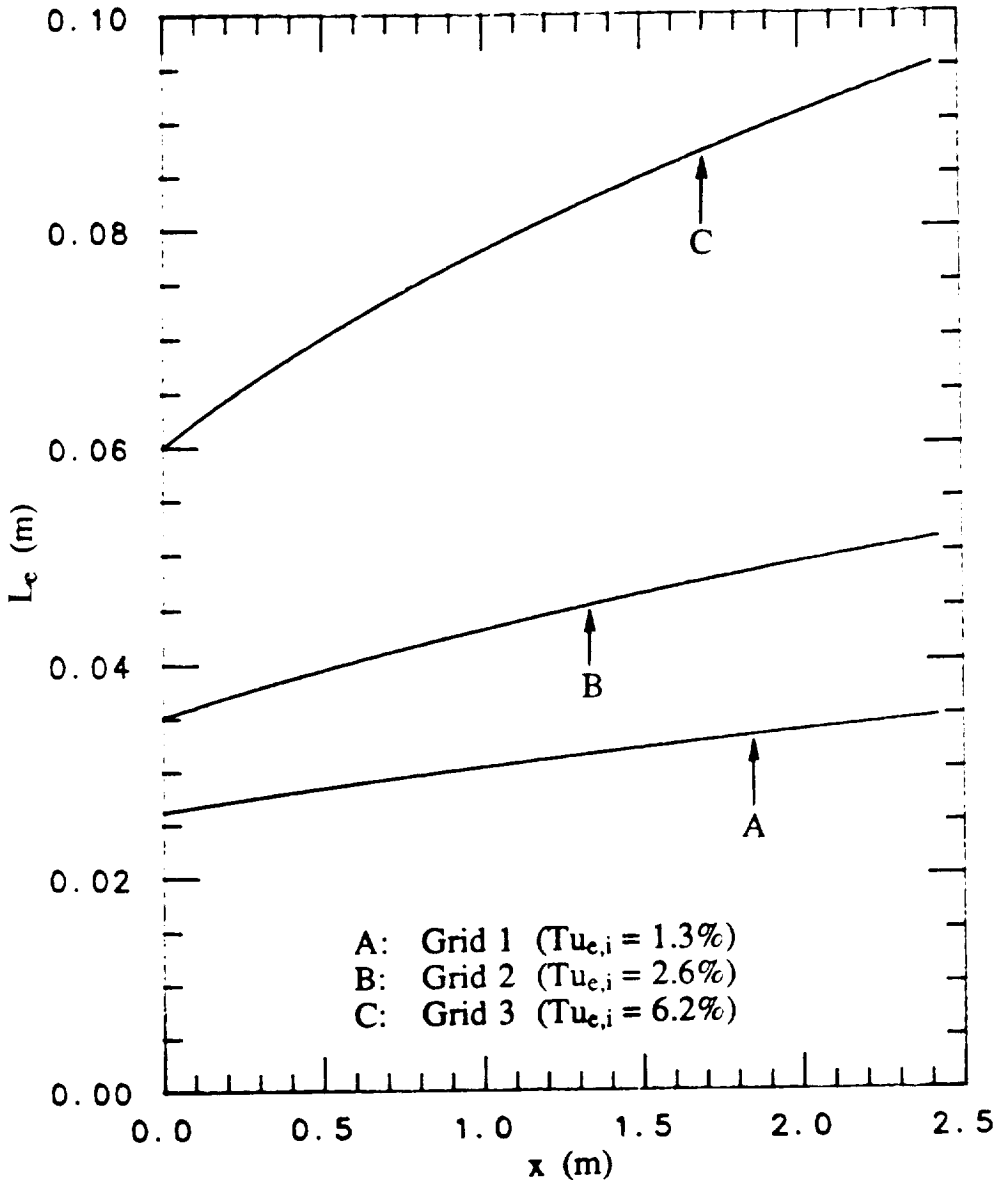

Figure 3.12. Freestream length scale versus x-distance for the numerical simulation of Blair and Werle's [1980] freestream turbulence level distribution.

The most accurate method for obtaining proper values for $k_e(x=0)$ and $\hat{\varepsilon}_e(x=0)$ requires the knowledge of the decay of freestream turbulence provided by experimental results. From the knowledge of the decay of $Tu_e(x)$, equation (3.25) may be used to obtain the corresponding $k_e(x)$ distribution. The difficulty of specifying $\hat{\varepsilon}_e(x=0)$ is solved by simply creating a computer code that integrates equations (3.44) and (3.45) given a value for $k_e(x=0)$ and an initial guess for $\hat{\varepsilon}_e(x=0)$. The resulting numerical $k_e(x)$ distribution may be graphically compared with the experimental $k_e(x)$ distribution to see if the initial guess for $\hat{\varepsilon}_e(x=0)$ results in the proper decay of $k_e(x)$. If the initial $\hat{\varepsilon}_e(x=0)$ value is not correct, another guess for $\hat{\varepsilon}_e(x=0)$ is made and the numerical calculation is conducted again. This process continues until the guess for $\hat{\varepsilon}_e(x=0)$ results in a numerical $k_e(x)$ distribution that matches the experimental $k_e(x)$ decay. As mentioned in Chapter 1, for accurate numerical turbulence modeling, the freestream turbulence level must be specified at a minimum of two locations in order for the initial $\hat{\varepsilon}_e$ boundary condition to be calculated.

For the case when only one value of the freestream turbulence level is known, a method to estimate the correct initial $\hat{\varepsilon}_e$ value has been developed by the author. From the grid generated turbulence studies of Comte-Bellot and Corrsin [1966], it was noted that the longitudinal length scale could be approximated by a power law fit

$$L_e = (x - x_1)^m \tag{3.46}$$

where $m \approx 0.34$ and x_1 is the apparent origin of the length scale growth. A computer code was developed that solved equations (3.44) and (3.45) subject to the given $k_e(x=0)$ and an initial guess for $\hat{\varepsilon}_e(x=0)$. At each x-station of the integration the freestream length scale is calculated according to equation (3.41). Upon completion of the numerical calculation, the slope of the numerical L_e-distribution is compared with the slope, m , measured by Comte-Bellot and Corrsin. If the slopes

do not match, a new guess for $\hat{\varepsilon}_e(x=0)$ is made and the calculations are conducted again. Eventually, a value of $\hat{\varepsilon}_e(x=0)$ is found which allows the slope of the numerical L_e-distribution to match the slope of the power law fit of Comte-Bellot and Corrsin.

Chapter 4

Numerical Simulation of Transition

4.0 Introduction

This chapter compares the simulation capability of Schmidt's proposed transition model, equations (2.55), coupled with the K. Y. Chien two-equation turbulence model. The first section examines the sensitivity of the "natural transition" behavior of the K. Y. Chien model to the initial turbulence profiles. The "natural transition" process is a built-in transition model that all two-equation turbulence models possess to simulate laminar-to-turbulent flow via the diffusion of TKE and TDR from the freestream boundary. A sequence of computational tests were conducted to evaluate the influence that the initial turbulence profiles have on "natural transition", which must be known if the effects of the transition models are to be evaluated. The second section outlines the calibration method used to obtain empirical model constants for the transition models and a comparison between the numerical simulation of Schmidt's PTM transition model, equation (2.55), and the experimental transition studies of Blair and Werle [1980]. From this comparison, a problem associated with the K. Y. Chien two-equation model for transition studies was identified. The third and final section defines the reason why the K. Y. Chien two-equation turbulence model should not be used for transition studies.

4.1 Sensitivity of Starting Conditions on "Natural Transition"

The importance of initial profiles to the prediction of transition has been demonstrated in the work by Rodi and Scheuerer [1985a, 1985b] and Schmidt [1987]. In Rodi and Scheuerer's work, an improvement in transition predictions

was shown with the use of their "physically" realistic k and ε initial profiles. This section examines the following questions, proposed by Schmidt [1987], in an attempt to limit the influence inappropriate initial conditions have on transition predictions,

1. How important to the transition predictions is the exact location at which the calculations are started?
2. How important is the specification of the initial ε profile to the prediction of transition?
3. What are the quantitative differences in the transition predictions when the freestream turbulence varies and how do these predictions compare with known correlations?

The first question addresses problem of where to begin numerical calculations for accurate transition studies. Schmidt [1987] developed a consistent method for determining the starting location for transition studies, and in contrast, for the present work different k and ε initial profiles were used in a different boundary layer computer code. Therefore, a starting criterion for transition calculations must be defined. The second question addresses the lack of information concerning the definition of the ε profile in a laminar boundary layer with high freestream turbulence. The effect that the a_1 structural coefficient for the initial ε profile (equation 3.28) has on the boundary layer calculations is not known. Before the transition models can be evaluated, the importance of well-posed initial turbulence profiles must be assessed. The third question addresses the effect freestream turbulence levels have on the behavior of two-equation "natural transition".

4.1.1 Effect of Starting Location on "Natural Transition"

A set of numerical experiments were conducted to determine the effect that the starting location has on the "natural transition" prediction of the K. Y. Chien

two-equation turbulence model. The following conditions were maintained for the numerical experiments (see Appendix D for details of the numerical parameters)

- Flat plate flow to eliminate curvature effects
- $dP/dx = 0$ by using a constant freestream velocity
- Tu_e = constant = 3.0% by setting $\hat{\varepsilon}_e$ to a small value
- The $\hat{\varepsilon}$-profile structural coefficient, a_1, was maintained at 1.0.

The initial profiles for these numerical tests were generated using equations (3.11), (3.21), (3.26), and (3.28). By setting $a_1 = 1.0$ for this set of test cases, the initial TDR profile did not influence the results and the behavior of the "natural transition" due to the starting location could be examined solely. For these numerical tests, the starting locations examined were for Re_x equal to 10^0, 10^1, 10^2, 10^3, and 10^4. The local friction coefficient, C_f, distribution is used to examine the transition process over the flat plate, since C_f correlations for both laminar and turbulent flow exist and serve as lower and upper bounds for evaluating the transition process.

Figure 4.1 is a plot of the flat plate C_f distribution versus momentum Reynolds number. This figure shows the sensitivity of the transition prediction to the starting location. From Figure 4.1, it is noted that for $Re_x \geq 10^4$ the transition prediction is dependent on the starting location, but for $Re_x \leq 10^3$ the transition prediction is independent of the starting location. Since the Reshotko [illegible] profile criteria, equation (3.27), generates starting profiles at Re_x less than 10^3, the use of this criteria for locating initial profiles will ensure the numerical transition predictions are independent of the starting location. Schmidt [1987] also concluded that the location of the transition became independent of the starting location for $Re_x < 10^3$.

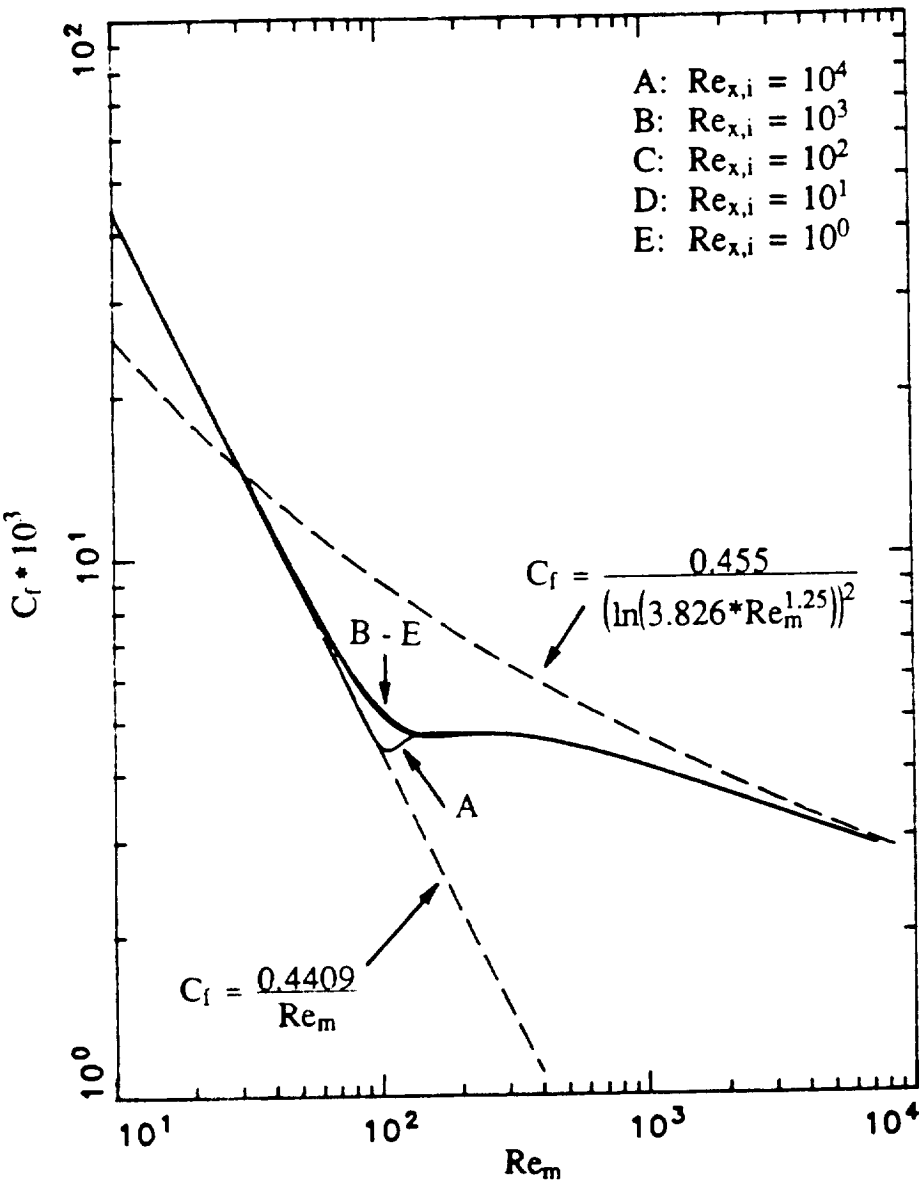

Figure 4.1. Local friction coefficient distribution versus momentum Reynolds number for sensitivity of "natural transition" predictions of the K. Y. Chien turbulence model [1982] to the calculation starting location.

4.1.2 Effect of Turbulent Dissipation Rate Profile on "Natural Transition"

This section examines the effect that the initial TDR profile has on the "natural transition" process of the K. Y. Chien turbulence model. As discussed in Section 3.1.4, the TDR initial profile contains a structural coefficient, a_1, which acts as a scaling parameter. Since no experimental data exists for TDR profiles, it is not known what a_1 should be set to in order to generate accurate initial TDR profiles. To remedy this problem a set of numerical tests were conducted to determine if the "natural transition" process would become independent of the initial TDR profiles for certain values of a_1. For this set of numerical tests the following conditions were maintained (see Appendix D for further details)

- Flat plate flow to eliminate curvature effects
- $dP/dx = 0$ by using a constant freestream velocity
- Tu_e = constant = 3.0% by setting $\hat{\varepsilon}_e$ to a small value
- The starting location is $Re_x = 10^1$ (equation 3.27).

As with the previous sensitivity analysis, the initial profiles for these numerical tests were generated using equations (3.11), (3.21), (3.26), and (3.28). From the previous section, it was determined that setting the starting location to $Re_x \leq 10^3$, will not influence the transition predictions. Different TDR initial profiles were generated by setting a_1 equal to 10^2, 10^1, 10^0, 10^{-1}, and 10^{-2}. The initial TKE and velocity profiles were the same for each simulation, but each TDR initial profile had the same basic shape but were scaled differently due to a_1.

Figure 4.2 is the plot of the C_f distribution versus momentum Reynolds number for each set of initial profiles. As shown in this figure, the transition prediction is independent of a_1 when the calculations are started at $Re_x < 10^3$. This conclusion is consistent with what Schmidt [1987] observed.

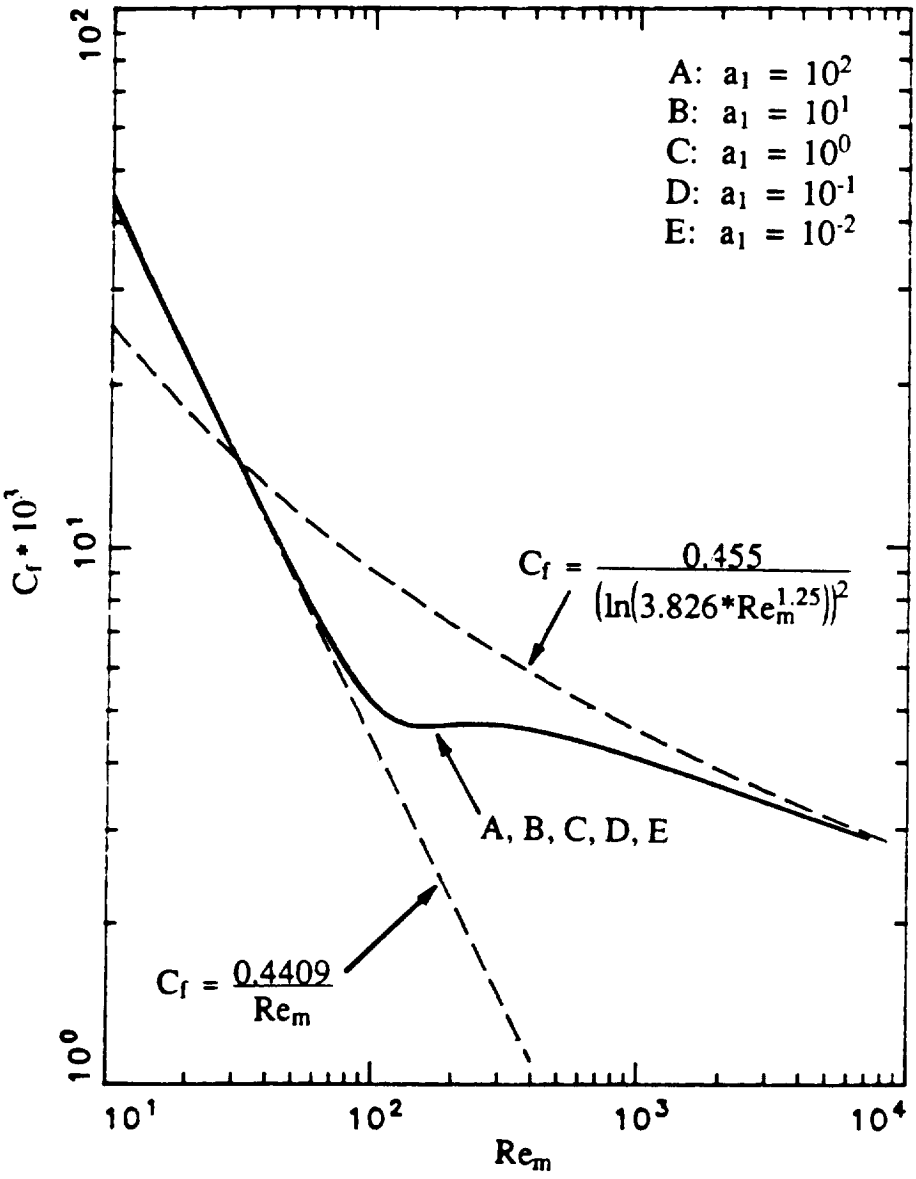

Figure 4.2. Local friction coefficient distribution versus momentum Reynolds number for sensitivity of "natural transition" predictions of the K. Y. Chien turbulence model [1982] to the initial turbulent dissipation rate profile.

The "natural transition" process of two-equation turbulence models is controlled by the transport of k into the boundary layer from the freestream. From the numerical tests conducted so far, it appears that by moving the starting location upstream, the transition prediction becomes independent of the initial profiles; therefore the lack of information concerning the initial profiles for TKE and TDR does not hinder transition modeling. By moving the starting location upstream, the length over which k has an opportunity to diffuse and convect into the boundary layer before reaching any particular downstream location has increased. The results of the previous sensitivity analyses has been to create a criteria for initiating numerical calculations that will not affect the "natural transition" process. With the "natural transition" process unaffected, any proposed transition model may be implemented into TEXSTAN and the resulting modification to the transition prediction may be easily evaluated.

4.1.3 Effect of Freestream Turbulence Level on "Natural Transition"

The effect of freestream turbulence on transition has been discussed by Jones and Launder [1974] and detailed by Schmidt [1987]. As a further examination, this section outlines a set of numerical tests that were conducted to determine the behavior of "natural transition" as computed by the K. Y. Chien two-equation for various freestream turbulence levels. For these numerical tests the following conditions were maintained (see Appendix D for further details)

- Flat plate flow to eliminate curvature effects
- $dP/dx = 0$ by using a constant freestream velocity
- The starting location determined from equation (3.27)
- The $\hat{\varepsilon}$-profile structural coefficient, a_1, was maintained at 1.0.

The initial profiles for these numerical tests were generated using equations (3.11), (3.21), (3.26), and (3.28). The tests were conducted for freestream turbulence levels, Tu_e, ranging from 1.0% to 8.0%. To maintain a constant freestream turbulence intensity, the freestream dissipation rate was set to 0.01.

Figure 4.3 is a plot of the C_f distribution versus momentum Reynolds number for each freestream turbulence level. As expected, the start of transition moves upstream with increasing freestream turbulence level due to the increased diffusion of TKE from the freestream. Also evident in Figure 4.3 is that at higher Tu_e levels (greater than 6.0%) the numerical C_f distribution is above the fully turbulent C_f correlation for large Re_m. The turbulent C_f correlation used in Figure 4.3 is for negligible freestream turbulence; therefore, it should be expected that the numerical C_f distribution be above the correlation at high freestream turbulence levels. Correlations for C_f in the presence of high freestream turbulence do exist but the strong nonlinear dependence of the C_f correlation on the freestream turbulence intensity and the freestream length scale make the C_f correlation difficult to define (see Hancock and Bradshaw, 1983). The turbulent C_f correlation used in Figure 4.3 (along with other figures) may be thought of as a gauge for determining the fully turbulent behavior of a two-equation turbulence model at low freestream turbulence levels. In Figure 4.3, the start and end of transition may be defined by the low and high points in the numerical C_f distributions. For $Tu_e \leq 2.0\%$ the start and end of transition is relatively easy to define; however, for $Tu_e > 2.0\%$ a distinct start and end of transition can not be easily defined because of the shape of the C_f distribution.

Abu-Ghannam and Shaw [1980] developed the following correlations for estimating the start and end of transition for zero pressure gradient flows as a function of the freestream turbulence intensity

$$Re_{m,S} = 163 + \exp(6.91 - 100*Tu_e) \tag{4.1}$$

and

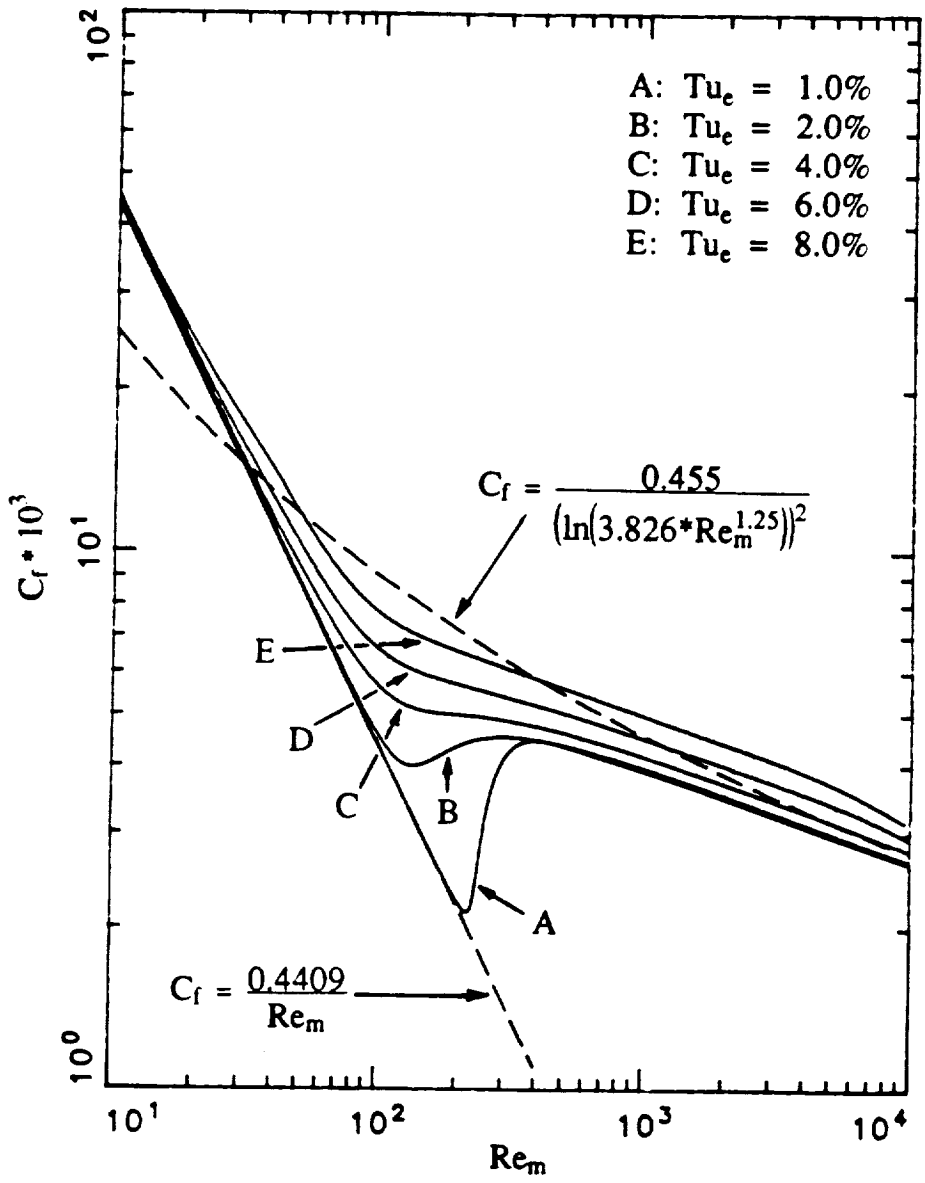

Figure 4.3. Local friction coefficient distribution versus momentum Reynolds number for sensitivity of "natural transition" predictions of the K. Y. Chien turbulence model [1982] to freestream turbulence levels.

$$Re_{m,E} = 2.667 * Re_{m,S} \quad (4.2)$$

where $Re_{m,S}$ is the momentum Reynolds number for the start of transition and $Re_{m,E}$ is the momentum Reynolds number for the end of transition. Figures 4.4 and 4.5 are plots of the start and end momentum Reynolds number as a function of freestream turbulence intensity for the test cases described above. As shown in Figures 4.4 and 4.5, the start and end momentum Reynolds number could only be defined for the test cases with $Tu_e \leq 2.0\%$. For the other test cases a definitive start and end could not be defined. From Figure 4.4, the onset of transition has the correct trend but it is consistently earlier than specified by the Abu-Ghannam and Shaw correlation. In Figure 4.5, the correct trend is also observed, but as with the start, the end of transition is consistently predicted early. Also noted from Figures 4.4 and 4.5 is that as the freestream turbulence level increases, the transition length decreases but the numerical transition length is consistently shorter than the experimental transition lengths of Abu-Ghannam and Shaw.

In summary, this section has investigated the effect that the initial turbulent profiles have on the "natural transition" predictions of the K. Y. Chien two-equation turbulence model. It was shown that "natural transition" is sensitive to the starting location of the initial profiles for $Re_x = 10^4$. The reason for this dependance has to do with the fact that the "natural transition" capability of two-equation turbulence models is a function of the diffusion and conduction of TKE into the boundary layer from the freestream, which of course is a function of the distance over which the boundary layer has developed. However, the K. Y. Chien turbulence model is not sensitive to the starting location for $Re_x \leq 10^3$. The C_f distribution was shown to have no dependance on the structural coefficient of the dissipation profile as long as the initial profile begins at $Re_x \leq 10^3$. The independence of the "natural transition" behavior to the scale of the initial $\hat{\varepsilon}$-profile is a benefit since there is no experimental data available to calculate initial $\hat{\varepsilon}$-profiles. The "natural transition" behavior of the K. Y. Chien turbulence model was shown to have the

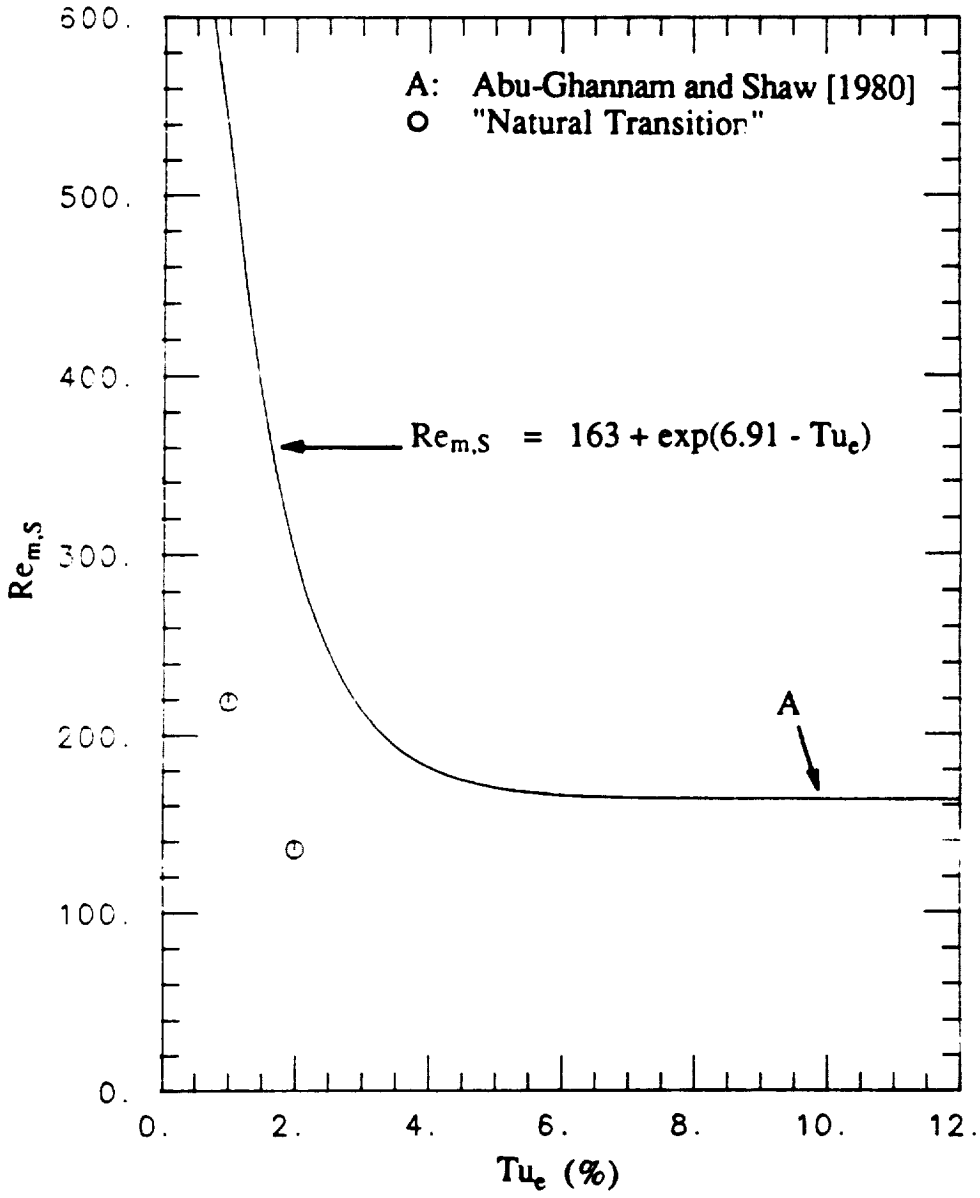

Figure 4.4. Comparison of the numerical start of transition based on momentum Reynolds number for K. Y. Chien [1982] "natural transition" and the experimental correlations of Abu-Ghannam and Shaw [1980].

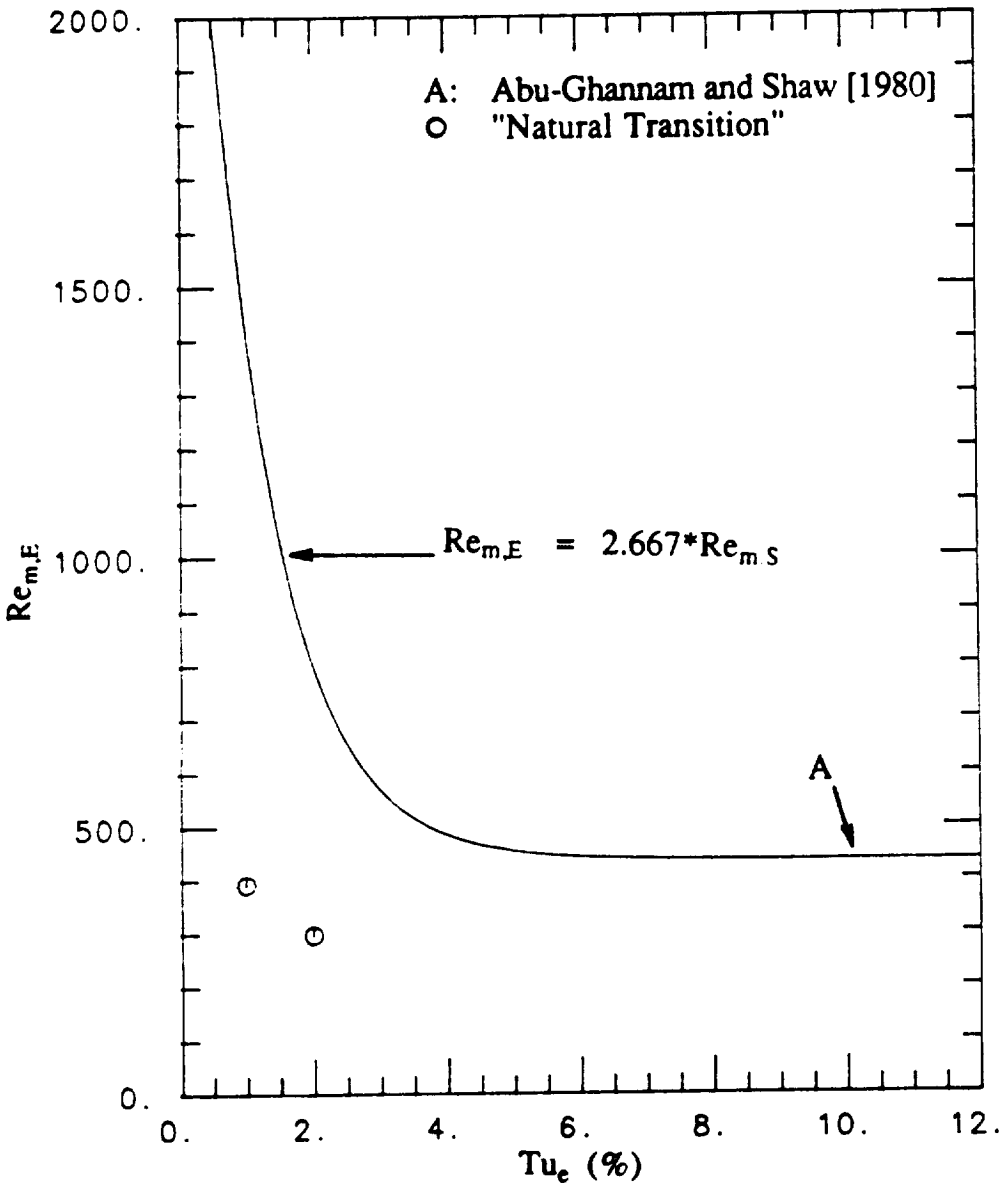

Figure 4.5. Comparison of the numerical end of transition based on momentum Reynolds number for K. Y. Chien [1982] "natural transition" and the experimental correlations of Abu-Ghannam and Shaw [1980].

correct trends when compared to the data of Abu-Ghannam and Shaw, but the start, end, and length of transition was consistently shorter than for experimental measurements.

4.2 Numerical Simulations Using Schmidt's PTM Transition Model

The purpose of this section is to determine if Schmidt's proposed transition model will improve the transition capability of the K. Y. Chien two-equation turbulence model when used in the TEXSTAN boundary layer computer code. In the previous section it was shown that the "natural transition" predictions of the K. Y. Chien turbulence model resulted in transition predictions with the correct trends but with the start and end consistently predicted early, resulting in a short length of transition. In this section, the calibration method and results for the transition model proposed by Schmidt, equation (2.55), coupled with the K. Y. Chien turbulence model in the TEXSTAN boundary layer code is discussed. Then the simulation of the flat plate heat transfer data of Blair and Werle [1980] using Schmidt's PTM transition model and the K. Y. Chien model are compared to the experimental data to determine the prediction capability of the transition model.

4.2.1 Calibration Procedure for Schmidt's PTM Transition Model

The transition model proposed by Schmidt controls the growth rate of TKE in the boundary layer and thus controls the transition process. As shown in equation (2.55), two empirical parameters, A and B, must be calibrated for each two-equation turbulence model. Schmidt obtained calibration curves for the A and B empirical constants as functions of freestream turbulence intensity for the Lam and Bremhorst [1981] and Launder and Sharma [1974] two-equation turbulence mod-

els. However, in this thesis the K. Y. Chien two-equation turbulence model is used; therefore, new calibration curves for A and B must be developed.

The start and end of transition correlations proposed by Abu-Ghannam and Shaw, equations (4.1) and (4.2), are used to determine when the correct combination of A and B allows the numerical transition prediction to match the experimental correlations for a given freestream turbulence intensity. Since the prediction capability of the transition models are based on the A and B empirical parameters, which in turn are based on the experimental correlations of Abu-Ghannam and Shaw, the importance of these experimental transition correlations is readily apparent.

For a given freestream turbulence intensity, a series of computational tests were conducted. Given an initial guess for A and B, a corresponding start and end of transition is numerically calculated and compared to the Abu-Ghannam and Shaw transition correlations. If the guess for A and B does not yield the correct start and end of transition, another guess for the A and B is made. This iteration process continues until given values of A and B yields a start and end of transition that matches the Abu-Ghannam and Shaw correlations.

To reduce the number of required guesses to determine A and B at each turbulence intensity, it is suggested that the following plotting method be used. Contour plots for $Re_{m,S}$ and $Re_{m,E}$ as a function of A and B are used to track the transition start and end momentum Reynolds numbers prescribed by equations (4.1) and (4.2). By observing the trends of both the start and end momentum Reynolds number contour plots, guesses for A and B are made until the $Re_{m,S}$ contour line and the $Re_{m,E}$ contour line cross at the same combination of A and B. It is at this cross-over point where the specified A and B will yield a $Re_{m,S}$ and $Re_{m,E}$ that matches the Abu-Ghannam and Shaw correlations.

It should be noted that Schmidt used an additional stability criteria in conjunction with his PTM transition model to control the production term of the k-

equation. He believed that since the production term, P_k, is the model term that simulates the amplification of perturbations in the boundary layer, there should be some critical momentum Reynolds number, $Re_{m,C}$, below which P_k should always be insignificant. For $Re_m < Re_{m,C}$, P_k is maintained at zero. This critical momentum Reynolds number criteria affects only the production of k and does not affect the transport of k in the boundary layer for $Re_m < Re_{m,C}$. Schmidt believed $Re_{m,C}$ should be approximately equal to 162, corresponding to the Tollmien-Schlichting limit of stability. However, at high Tu_e levels transition occurs near $Re_m = 163$ which does not allow sufficient time for the TKE to develop in the boundary layer. Therefore Schmidt used $Re_{m,C} = 125$ for all of his calculations. For low Tu_e, the $Re_{m,C}$ affects are minimal. For the present study, $Re_{m,C}$ was set to zero and P_k was calculated over the entire calculation domain. The reason for not using $Re_{m,C}$ is due to the observations of Dyban et al. [1976] who stated that in the presence of high freestream turbulence the boundary layer does not act as a laminar boundary layer. Therefore, since the boundary layer is not purely laminar, the production of k would not be suppressed and instead would be continually changing. Note that, following Schmidt, modification of P_k in the production of dissipation was not carried out.

4.2.2 Calibration of Schmidt's PTM Transition Model for the K. Y. Chien Turbulence Model

The method for obtaining calibration curves for the A and B empirical constants of Schmidt's PTM transition model coupled with the K. Y. Chien turbulence model requires a series of numerical tests. The conditions for the calibration tests were the same as discussed in Section 4.1.3,

- Flat plate flow to eliminate curvature effects
- dP/dx = 0 by using a constant freestream velocity
- The starting location determined from equation (3.27)

- The $\hat{\varepsilon}$-profile structural coefficient, a_1, was maintained at 1.0
- The freestream dissipation rate is set to 0.01 to maintain a constant freestream turbulence intensity.

The effect of a decaying freestream turbulence intensity will be discussed later. Test calculations to determine the values of A and B for the K. Y. Chien two-equation turbulence model with the Schmidt PTM transition model were conducted for freestream turbulence levels of 1.0% to 8.0%. For the test calculations, the start and end of transition is taken to be the minimum and maximum points of the calculated C_f distribution.

The results of the calibration tests for calculating the A and B empirical constants of Schmidt's transition model are shown in Figures 4.6 and 4.7. In these Figures, the A and B constants have been nondimensionalized with respect to the initial freestream conditions as follows

$$\overline{A} = \frac{A\,\mu_e}{\rho_e\,U_e^2} \tag{4.3}$$

and

$$\overline{B} = \frac{B\,\mu_e^2}{\rho_e^3\,U_e^6}\,. \tag{4.4}$$

Curve fits between the discrete numerical calibration tests allowed the values of A and B to be determined for any freestream turbulence level between 1.0% and 8.0%. The curve fits described the variation of A and B as follows,

$$\text{for} \quad 0.01 \le \phi \le 0.08 \quad A = 20.687 - 2605.0*\phi + (8.0223*10^4)*\phi^2 - (1.0488*10^6)*\phi^3 + (4.9551*10^6)*\phi^4 \tag{4.5}$$

and

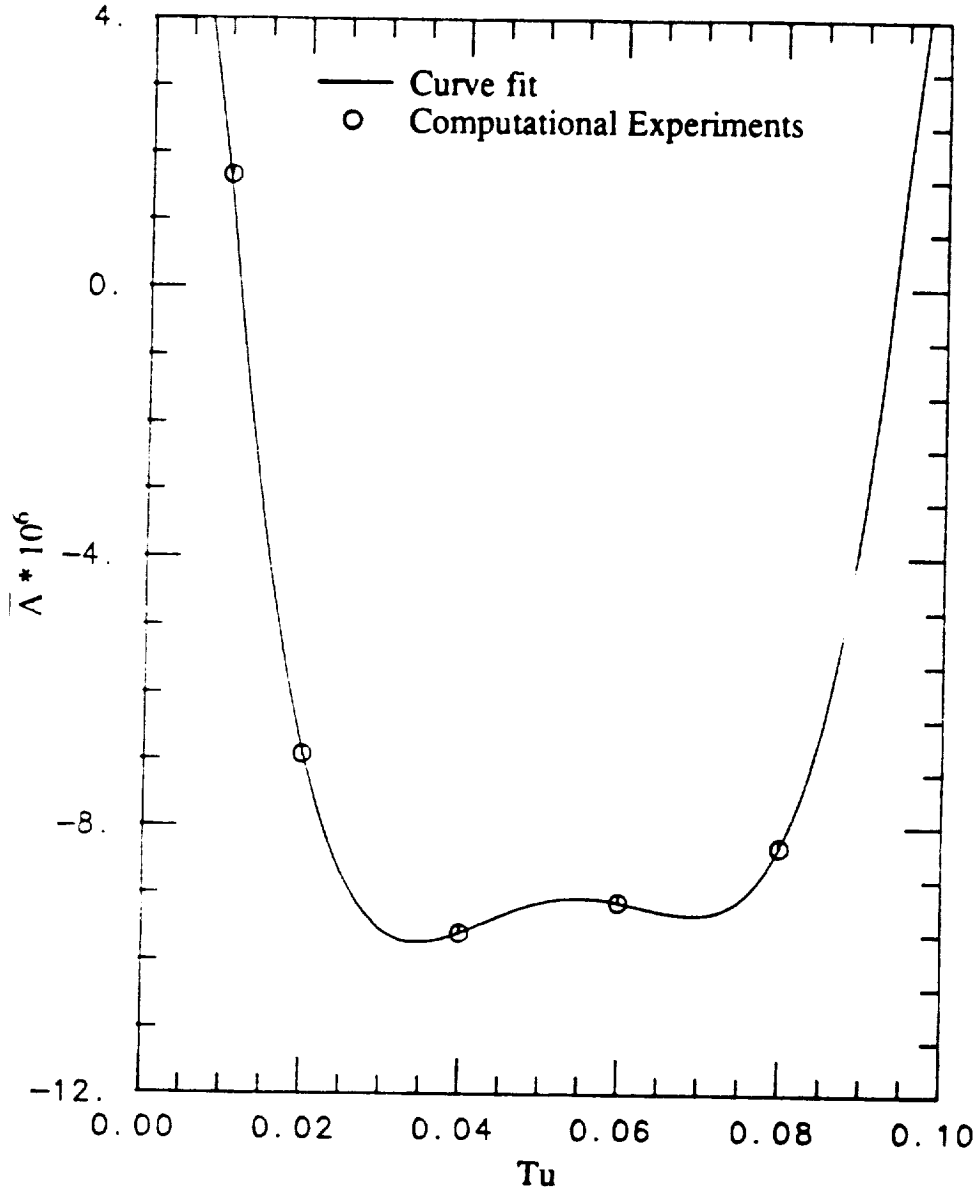

Figure 4.6. Calibration curve for $\bar{A}$ as a function of freestream turbulence intensity for Schmidt's PTM transition model coupled with the K. Y. Chien turbulence model [1982].

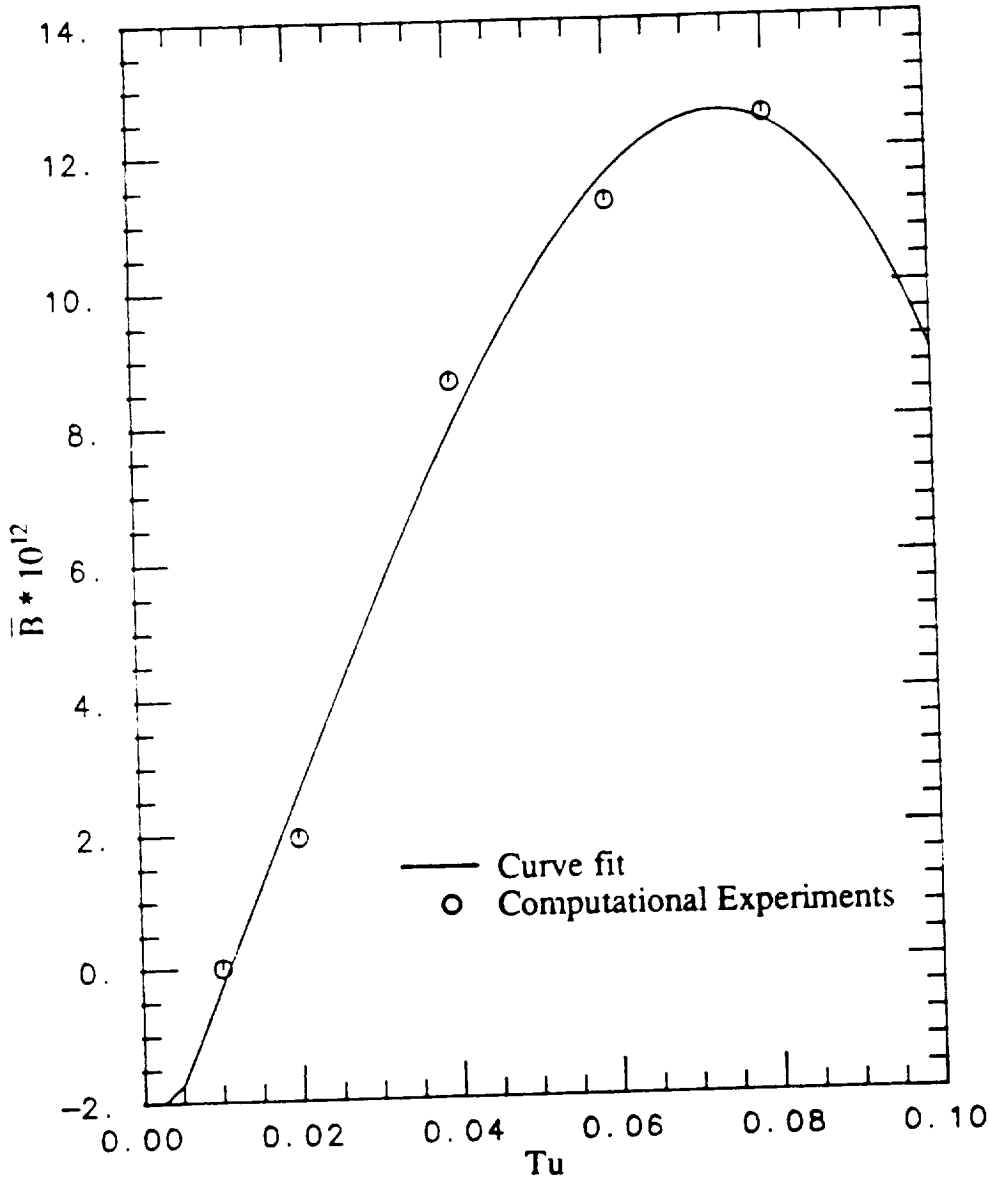

Figure 4.7. Calibration curve for $\overline{B}$ as a function of freestream turbulence intensity for Schmidt's PTM transition model [1987] coupled with the K. Y. Chien turbulence model [1982].

$$\text{for} \quad 0.01 \le \phi \le 0.08 \quad B = -3.1533 + 277.72*\phi + 1066.2*\phi^2 - (2.6284*10^4)*\phi^3 \tag{4.6}$$

where $\phi = Tu_e$, $A = \overline{A}*10^6$, and $B = \overline{B}*10^{12}$.

Figures 4.8 and 4.9 show how the transition predictions of the K. Y. Chien two-equation turbulence model, coupled with Schmidt's PTM transition model, match the start and end transition momentum Reynolds numbers for the correlations of Abu-Ghannam and Shaw. These figures show that with Schmidt's PTM transition model, the numerical start and end of transition can be modified to match the correlations of Abu-Ghannam and Shaw.

All of the numerical transition tests so far have not allowed a decay in the freestream turbulence intensity so that the A and B empirical parameters could be evaluated for a constant freestream turbulence intensity. To eliminate a decay in freestream turbulence intensity, $\hat{\varepsilon}_e$ was set to a small value. However in reality, the freestream dissipation rate can be quite large, especially for high freestream turbulence intensities, which in turn causes a decay in Tu_e. To model the decay of Tu_e and its affects on transition, the calculation for the empirical parameters of the PTM transition model, A and B, are simply based on the local freestream conditions. Equation (3.25) may be rearranged to obtain an expression for the freestream turbulence intensity as a function of the freestream TKE and freestream velocity as follows

$$Tu_e = \frac{\sqrt{k_e}}{\sqrt{1.5}\, U_e}. \tag{4.7}$$

Using equation (4.7) the local freestream turbulence intensity is easily calculated and used with equations (4.5) and (4.6) to obtain new A and B values for the transition model based on the local conditions. Schmidt suggests the A and B pa

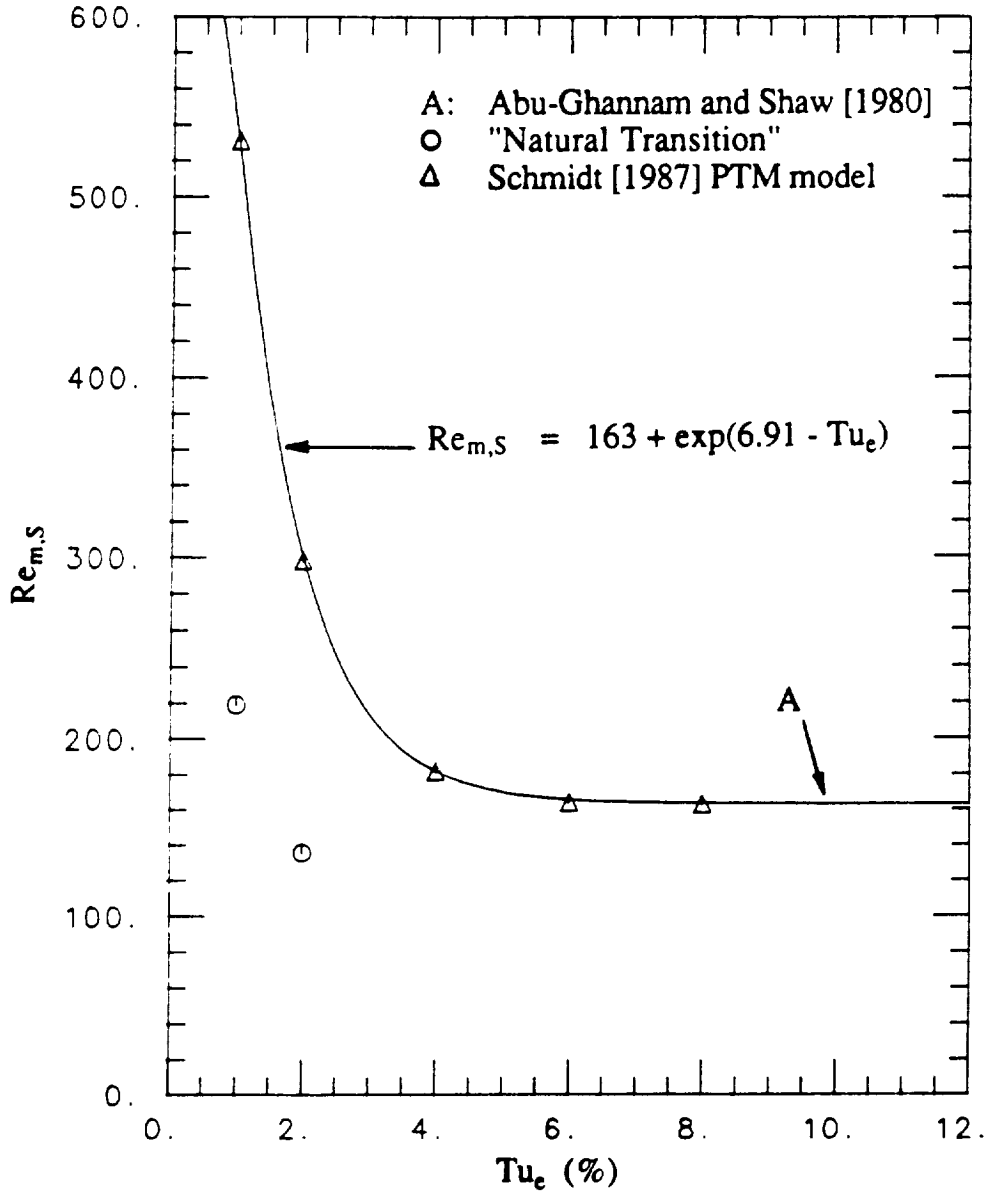

Figure 4.8. Comparison of the numerical start of transition based on momentum Reynolds number for K. Y. Chien [1982] "natural transition", Schmidt's PTM transition model [1987], and the experimental correlations of Abu-Ghannam and Shaw [1980].

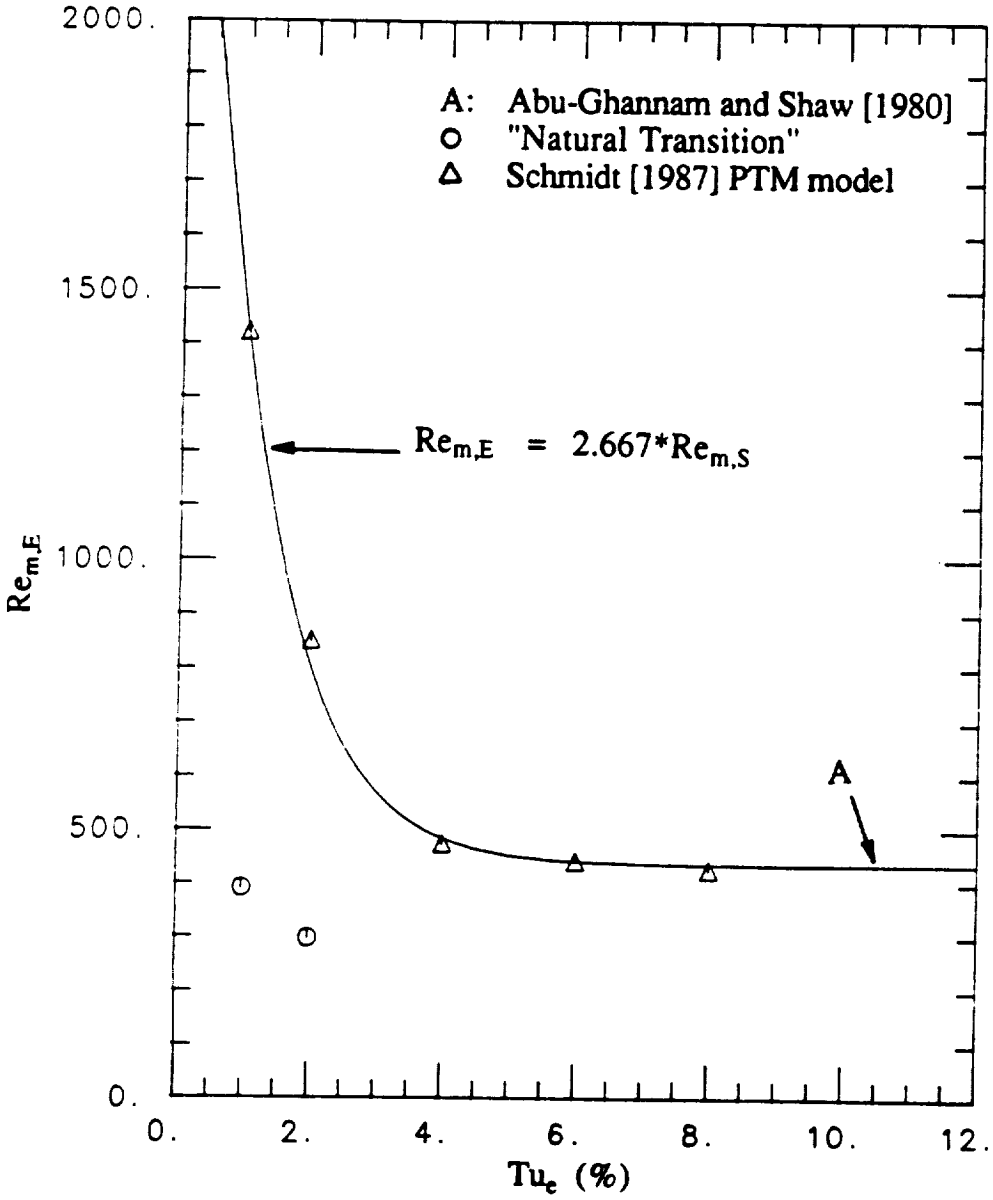

Figure 4.9. Comparison of the numerical end of transition based on momentum Reynolds number for K. Y. Chien [1982] "natural transition", Schmidt's PTM transition model [1987], and the experimental correlations of Abu-Ghannam and Shaw [1980].

rameters be updated every 10 to 20 integration steps for flows with high freestream turbulence intensities. The simplicity of Schmidt's transition model is readily apparent when flow acceleration or deceleration is added to the simulation process. The acceleration or deceleration of a boundary layer is produced by a change in the freestream velocity. Equation (4.7) takes a changing freestream velocity into account when calculating the freestream turbulence intensity; therefore, the empirical parameters, A and B, are easily calculated for an accelerating or decelerating boundary layer.

Figure 4.10 is a plot of the C_f distribution versus momentum Reynolds number for the same test conditions as for Figure 4.3 except that the PTM transition model has been used to simulate the start and end of transition according to the Abu-Ghannam and Shaw correlations. From Figure 4.10 it is noted that at Tu_e = 2.0% the end of transition has been moved far downstream and as a result the length of transition has increased considerably. A discussion of this problem will be detailed in Section 4.3.

4.2.3 Comparison of the K. Y. Chien Turbulence Model with Schmidt's PTM Transition Model to Experimental Data

The direct comparison of numerical transition simulations has not been conducted up to this point; instead the experimental correlations of Abu-Ghannam and Shaw have been used to calibrate Schmidt's PTM transition model for the K. Y. Chien turbulence model in TEXSTAN. At this point the PTM transition model will be used to simulate the experimental flat plate transition studies available in the open literature. All of the experiments considered are for transition occurring under the influence of freestream turbulence.

The first comparison of Schmidt's PTM transition model is made for the experimental data of Blair and Werle [1980]. The details of the flow parameters

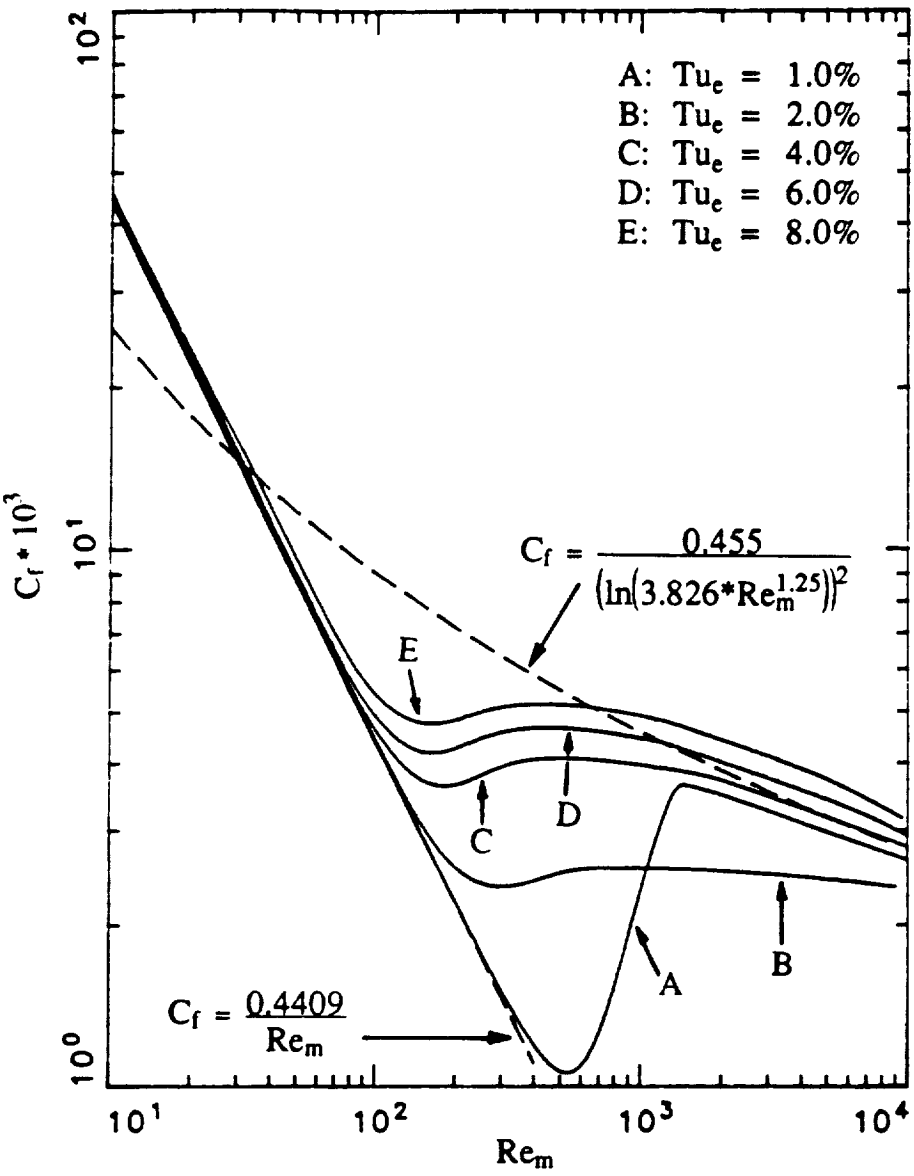

Figure 4.10. Local friction coefficient distribution versus momentum Reynolds number for freestream turbulence level sensitivity of Schmidt's PTM transition model [1987] coupled with the K. Y. Chien turbulence model [1982].

used for this comparison are provided in Appendix D. This set of numerical simulations are for flat plate zero pressure gradient flow. Blair and Werle measured the effects of transition in terms of heat transfer; therefore, the numerical comparisons with the experimental data will use the Stanton number, St. Three test cases, with freestream turbulence levels of 1.3%, 2.6%, and 6.2%, will be used to examine transition.

Figures 4.11 to 4.13 are plots of the Stanton number distribution versus x-Reynolds number for the grid 1 ($Tu_{e,i}$ = 1.3%), grid 2 ($Tu_{e,i}$ = 2.6%), and grid 3 ($Tu_{e,i}$ = 6.2%) flow conditions of Blair and Werle. In these figures, the "natural transition" and PTM modified transition are compared to the experimental transition data of Blair and Werle. In Figures 4.11 to 4.13 it is noted that the "natural transition" plots for the Stanton number do not show any form of transition similar to local friction coefficient plots. This apparent lack of transition is due to the fact that for all three Blair cases K. Y. Chien "natural transition" occurred on the unheated starting length of the plate; therefore, the step change in wall heat flux at the end of the unheated starting length masked any remnants of the transition process. In Figures 4.11 and 4.12, the PTM modified transition does not compare well to the experimental data in the transition region for the grid 1 and grid 2 flow conditions. In fact, the PTM model does not even reproduce the fully turbulent results.

In examining Schmidt's [1987] results for the grid 1, grid 2, and grid 3 cases of Blair and Werle [1980], it was shown that Schmidt could reproduce the experimental data quite accurately for grid 1 and fairly accurately for the other two grids. What was consistent with all of Schmidt's results was his ability to reproduce fully turbulent results at the end of transition. The results shown in Figures 4.11 to 4.13 are the first evidence that the K. Y. Chien two-equation turbulence model is not appropriate for transition studies. It was at this point that further comparison of Schmidt's PTM transition model in TEXSTAN with experimental data would be useless because of the apparent fundamental problem with using the K. Y. Chien two-equation turbulence model for transition studies. This low-Reynolds

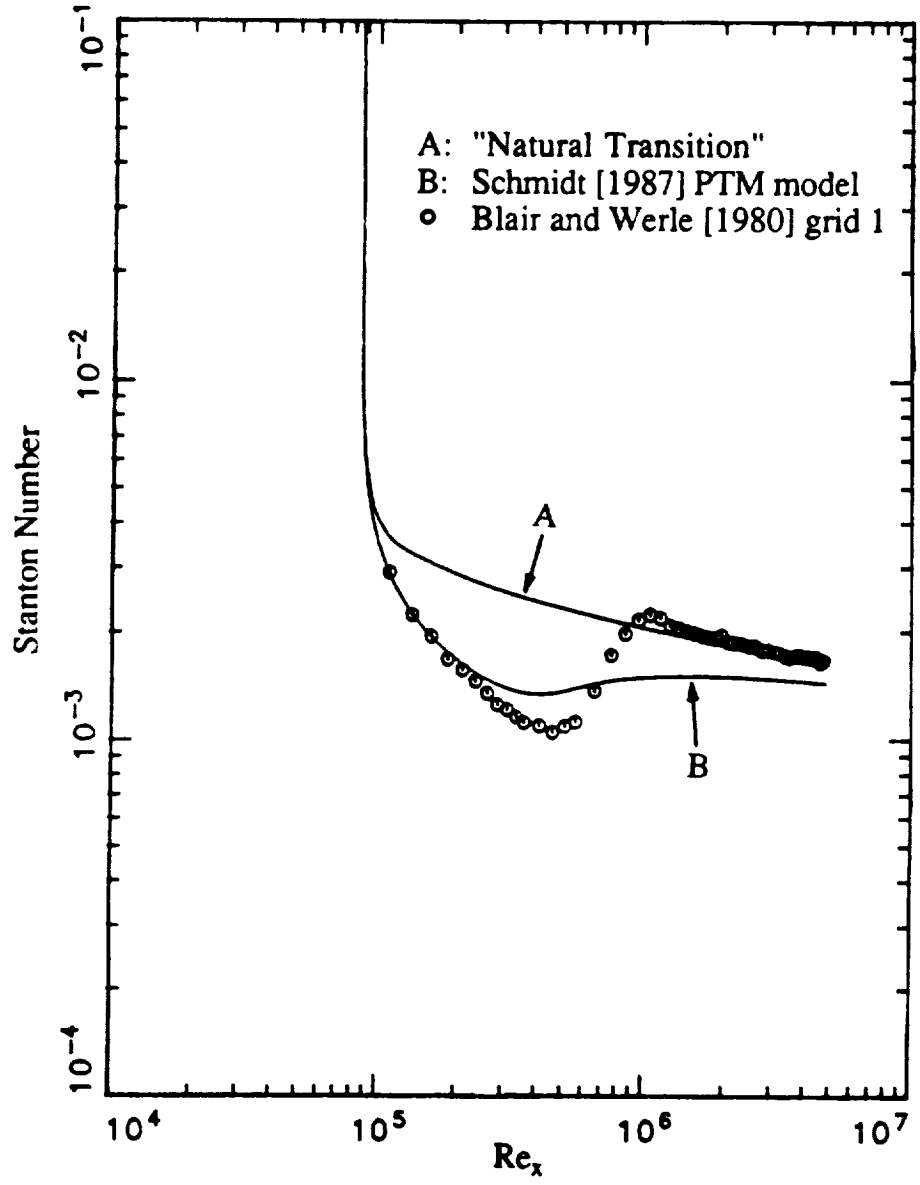

Figure 4.11. Comparison of the experimental zero pressure gradient heat transfer distribution of Blair and Werle [1980], for $Tu_e = 1.27\%$, to the K. Y. Chien turbulence model [1982] prediction for "natural transition" and for Schmidt's PTM transition model [1987].

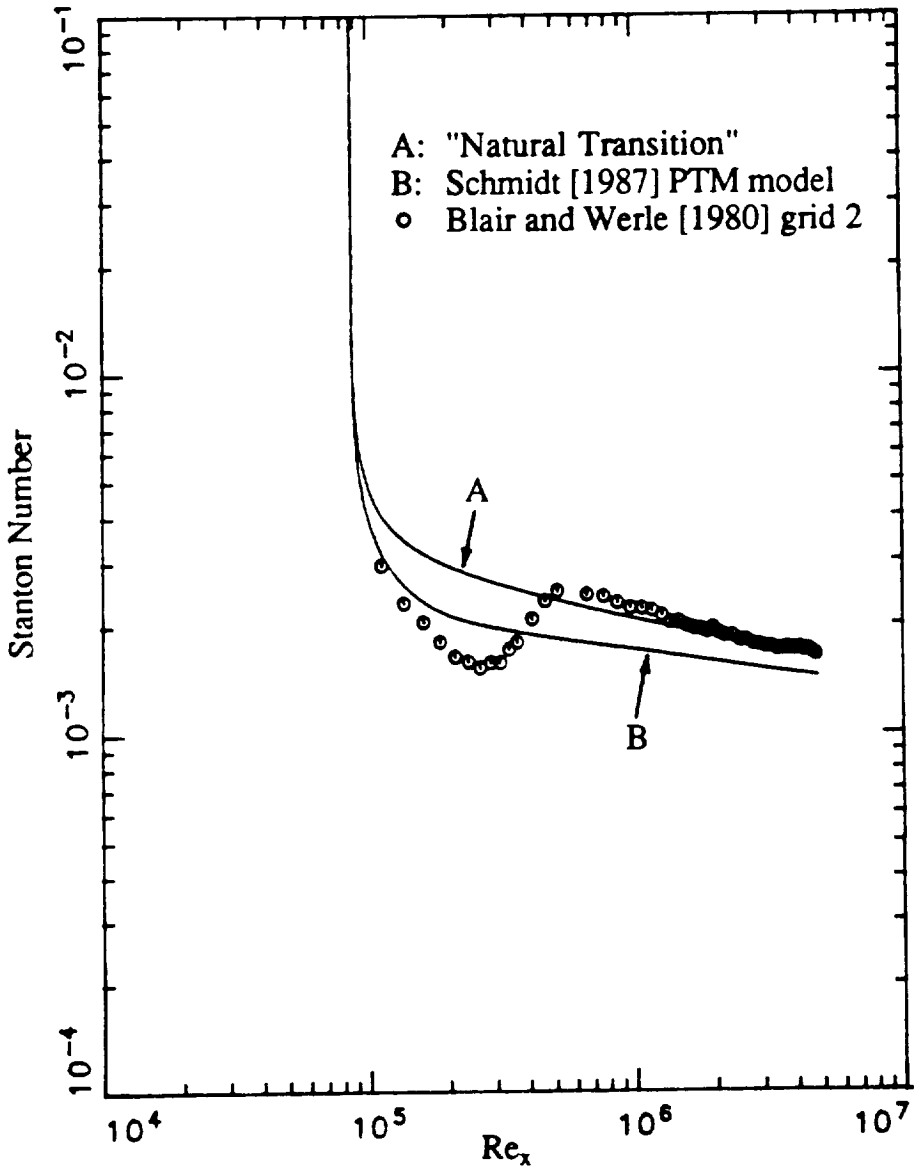

Figure 4.12. Comparison of the experimental zero pressure gradient heat transfer distribution of Blair and Werle [1980], for $Tu_e = 2.58\%$, to the K. Y. Chien turbulence model [1982] prediction for "natural transition" and for Schmidt's PTM transition model [1987].

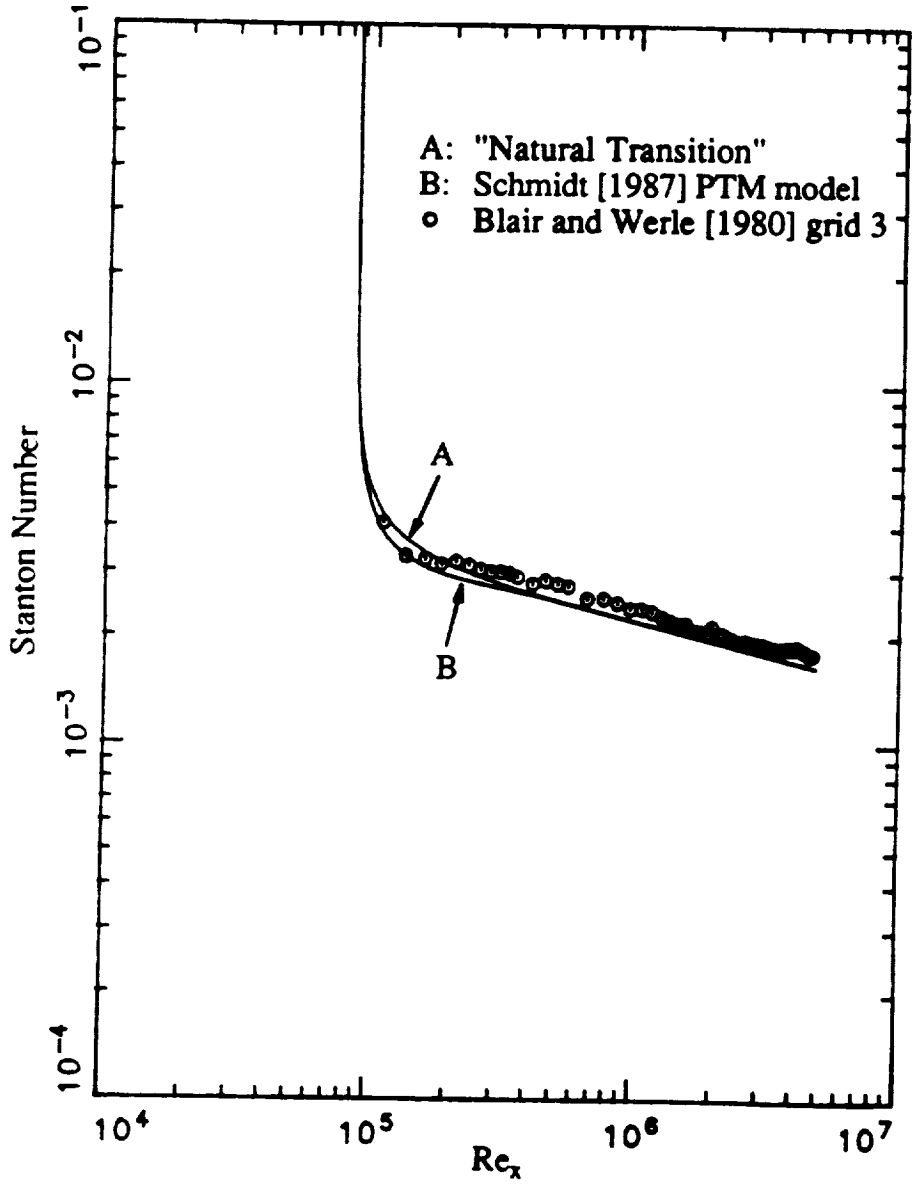

Figure 4.13. Comparison of the experimental zero pressure gradient heat transfer distribution of Blair and Werle [1980], for $Tu_e = 6.17\%$, to the K. Y. Chien turbulence model [1982] prediction for "natural transition" and for Schmidt's PTM transition model [1987].

number problem associated with the K. Y. Chien two-equation model also prevented a direct comparison of the transition prediction capabilities of Schmidt's PTM transition model and The University of Texas transition model. At this point the objective of this research turned to the identification of the source of the low-Reynolds number problem associated with the K. Y. Chien turbulence model.

4.3 Problems Associated with the K. Y. Chien Turbulence Model for Transition Studies

From Figures 4.11 and 4.12 it was noted that the modified transition results do not reproduce the experimental Stanton number distribution as well as expected. The numerical predictions appear to "damp" the development of a fully turbulent boundary layer. This behavior is also seen in Figure 4.10 for $Tu_e = 2.0\%$ which shows that the fully turbulent response is "damped", instead of predicting a fully turbulent boundary layer at the end of transition. The delay in the fully turbulent response with the use of Schmidt's PTM transition model is attributed to the "natural transition" behavior of the K. Y. Chien two-equation turbulence model. In Figure 4.3, the C_f distribution for "natural transition" with $Tu_e > 1.0\%$ appears to be "damped" instead of having a sharp increase as for $Tu_e < 1.0\%$. This "damping" effect hinders the ability to define a specific start and end of transition which is very important in developing the model constants for Schmidt's PTM transition model. Therefore, the "damping" of the transition response shown in Figure 4.10, using Schmidt's PTM transition model, can be directly related to the "damping" affect of the "natural transition" behavior for the K. Y. Chien two-equation turbulence model, shown in Figure 4.3.

To determine why the K. Y. Chien two-equation turbulence model yields a different "natural transition" behavior than traditional two-equation turbulence models, a comparison between the "natural transition" results of the K. Y. Chien [1982] and Launder and Sharma [1974] was conducted. The Launder and Sharma

[1974] two-equation turbulence model is similar to the Jones and Launder [1972 and 1973] two-equation turbulence model except for different empirical constants, damping functions, and low-Reynolds number terms as given in equations (2.45) to (2.54). The following conditions were used to compare the "natural transition" C_f distribution for the K. Y. Chien and Launder and Sharma two-equation turbulence models (see Appendix D for details),

- Flat plate flow to eliminate curvature effects
- $dP/dx = 0$ by using a constant freestream velocity
- The starting location determined from equation (3.27)
- Freestream turbulence intensity, Tu_e, was equal to 2.0%
- The $\hat{\varepsilon}$-profile structural coefficient, a_1, was maintained at 1.0
- The freestream dissipation rate is set to 0.01 to maintain a constant freestream turbulence intensity.

Figure 4.14 is a plot of the C_f distribution versus momentum Reynolds number for the K. Y. Chien and Launder and Sharma two-equation turbulence models. From Figure 4.14, two distinct differences in the transition predictions are evident. First, the K. Y. Chien transition model predicts an earlier start of transition ($Re_{m,S} \approx 135$) than for the Launder and Sharma transition model ($Re_{m,S} \approx 239$). Second, the start and end of transition for the K. Y. Chien model are not as clearly defined as for the Launder and Sharma model due to the "damping" affect in the K. Y. Chien results. The purpose of the comparison of the K. Y. Chien model to the Launder and Sharma model is to answer the following two questions,

1. Why does the K. Y. Chien two-equation turbulence model predict an earlier start of "natural transition" than the Launder and Sharma turbulence model?
2. Why does the C_f distribution for the K. Y. Chien two-equation turbulence model in the transition region appear to be damped instead of having a sharp increase?

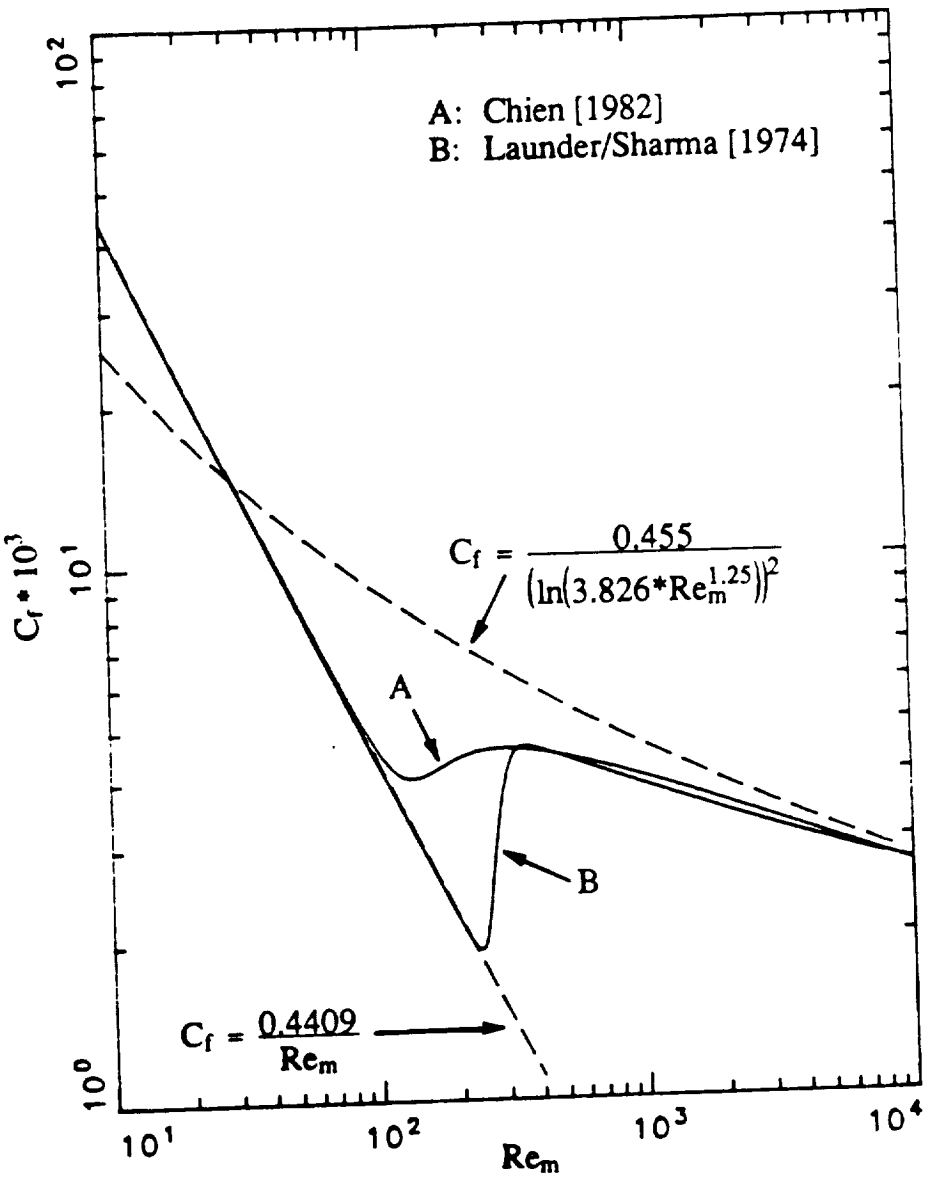

Figure 4.14. Local friction coefficient distribution versus momentum Reynolds number for a "natural transition" comparison of the K. Y. Chien turbulence model [1982] and the Launder and Sharma turbulence model [1974] for $Tu_e = 2.0\%$.

To answer the two questions posed above, the differences between the K. Y. Chien turbulence model and the Launder and Sharma turbulence model must be examined. The empirical constants, damping functions, and low-Reynolds number terms for the K. Y. Chien and the Launder and Sharma turbulence models are given in equations (2.35) to (2.44) and (2.45) to (2.54) respectively. In examining the various terms of the two turbulence models the major differences between the two models appear in the f_μ and f_2 damping functions, as well as the D and E low-Reynolds number terms.

To determine if the low-Reynolds number terms, D and E, are the cause of the differences between the K. Y. Chien turbulence model and the Launder and Sharma turbulence model, the source terms for equations (2.19) and (2.20) were combined as follows

$$S_k = \mu_t\left(\frac{\partial U}{\partial y}\right)^2 - \left(\rho\hat{\varepsilon} + D\right) \tag{4.8}$$

and

$$S_\varepsilon = C_1 f_1 \frac{\hat{\varepsilon}}{k}\mu_t\left(\frac{\partial U}{\partial y}\right)^2 - \left[\rho C_2 f_2 \frac{\hat{\varepsilon}^2}{k} + E\right] \tag{4.9}$$

Using equations (4.8) and (4.9), equations (2.19) and (2.20) are written as follows

$$\rho U\frac{\partial k}{\partial x} + \rho V\frac{\partial k}{\partial y} = \frac{\partial}{\partial y}\left[\left(\mu + \frac{\mu_t}{\sigma_k}\right)\frac{\partial k}{\partial y}\right] + S_k \tag{4.10}$$

and

$$\rho U\frac{\partial \hat{\varepsilon}}{\partial x} + \rho V\frac{\partial \hat{\varepsilon}}{\partial y} = \frac{\partial}{\partial y}\left[\left(\mu + \frac{\mu_t}{\sigma_\varepsilon}\right)\frac{\partial \hat{\varepsilon}}{\partial y}\right] + S_\varepsilon . \tag{4.11}$$

Equations (4.10) and (4.11) are not the exact form of the governing equations solved by TEXSTAN, instead, S_k and S_ε are used for plotting purposes to compare the K. Y. Chien turbulence model source terms to the Launder and Sharma source terms.

In comparing the K. Y. Chien and Launder and Sharma turbulence models, profiles of turbulence quantities are examined at various momentum Reynolds numbers, relating to Figure 4.14. In the following comparisons, it is useful to understand the status of the boundary layers for each of the turbulence models at specified momentum Reynolds numbers. Table 4.1 shows the boundary layer status for each turbulence model at specified momentum Reynolds numbers. The various momentum Reynolds numbers described in Table 4.1 and used in the following comparisons were selected to emphasize the distribution of the various boundary layer characteristics at the three stages of a boundary layer development, the laminar stage, transitional stage, and the fully turbulent stage. For Re_m equal to 30 and 60, both the K. Y. Chien and Launder and Sharma turbulence models calculate a laminar boundary layer. Therefore these two momentum Reynolds numbers demonstrate the developing laminar boundary layer under the influence of the two turbulence models. For Re_m equal to 135 to 359, both the K. Y. Chien and Launder and Sharma turbulence models are within various stages of transition. Therefore these momentum Reynolds numbers demonstrate a transitional boundary layer under the influence of the two turbulence models. For Re_m equal to 1000 and 3000, both the K. Y. Chien and Launder and Sharma turbulence models predict a fully turbulent boundary layer. Therefore, these two momentum Reynolds numbers serve to demonstrate the developing fully turbulent boundary layer under the influence of the two turbulence models.

Table 4.1. Boundary Layer Characteristics for Figure 4.14 as a Function of Momentum Reynolds Number and Type of Two-Equation Turbulence Model.

Re_m	Boundary Layer Characteristics	
	K. Y. Chien	Launder and Sharma
30.0	Laminar	Laminar
60.0	Laminar	Laminar
135.5	Start of transition	Laminar
239.0	In transition	Start of transition
300.0	End of transition	In transition
359.0	Turbulent	End of transition
1000.0	Turbulent	Turbulent
3000.0	Turbulent	Turbulent

In the profiles that follow, all of the "+ scaling" is in terms of the local shear velocity (u_τ) and kinematic viscosity. Definitions of the "+ scale" terms as well as the other profile variables are provided in the nomenclature.

Figures 4.15 to 4.18 are profiles of S_k^+ versus y^+ at the momentum Reynolds numbers specified in Table 4.1. Figure 4.15 shows that S_k^+ develops more rapidly for the K. Y. Chien model than for the Launder and Sharma model in the laminar region (Re_m = 30 and 60). Figure 4.16 shows the rapid rise in S_k^+ associated with the start of transition for both turbulence models, however, the rise in S_k^+ for the K. Y. Chien model occurs at Re_m = 135 where as for the Launder and Sharma model the rise in S_k^+ occurs at Re_m = 239. At the start of transition for the K. Y. Chien turbulence model the peak region is at approximately y^+ = 18, while the peak region is at a y^+ = 24 for the Launder and Sharma model. For fully turbulent flow, as shown in Figure 4.18, the S_k^+ distribution for $y^+ > 8$ are approximately the same for both turbulence models, but the peak region has moved closer to the wall (y^+ = 12) for both models due to diffusion. In Figures 4.16 to 4.18, the

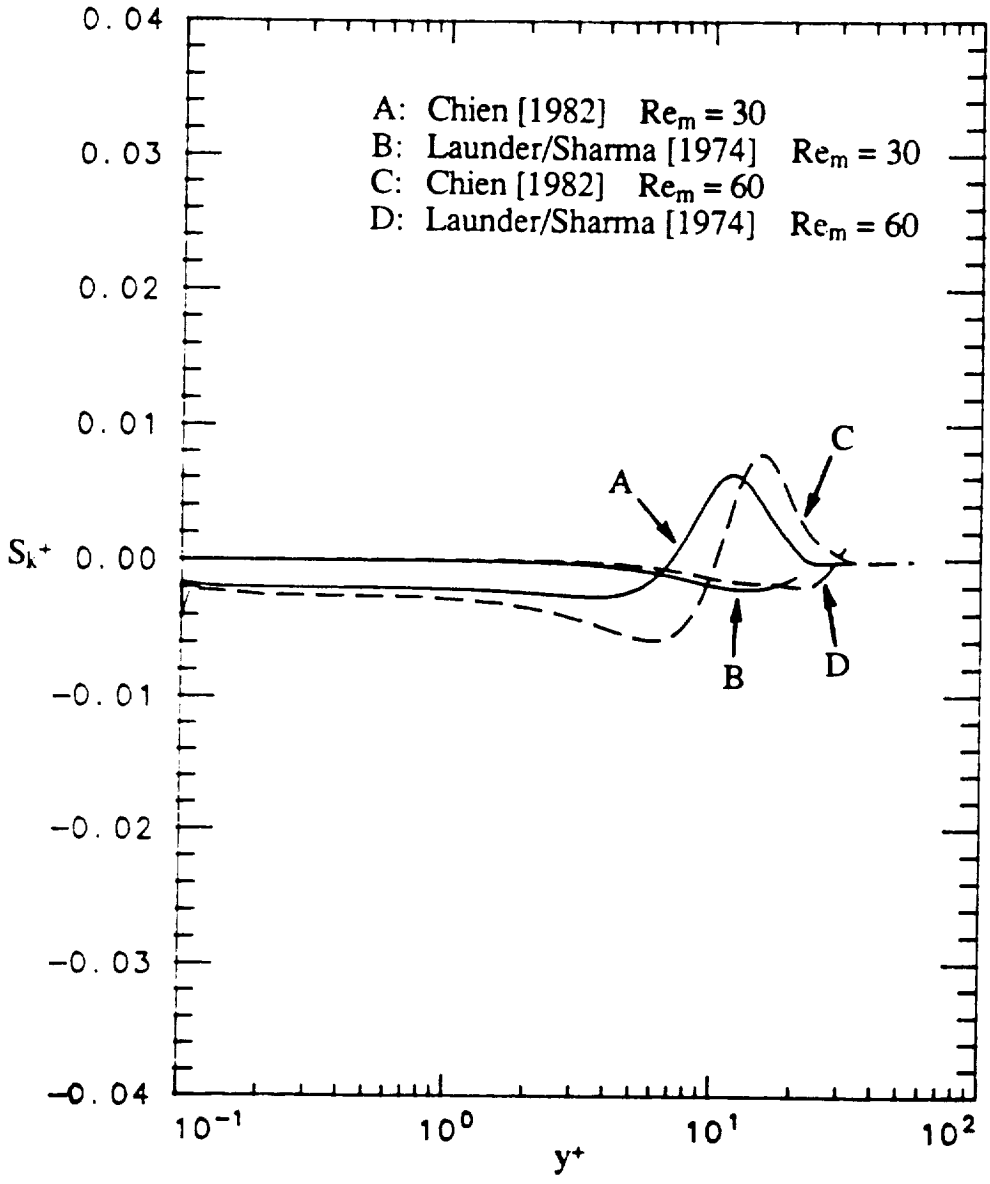

Figure 4.15. Turbulent kinetic energy source term profiles at $Re_m = 30$ and 60 for the K. Y. Chien [1982] and the Launder and Sharma [1974] turbulence models.

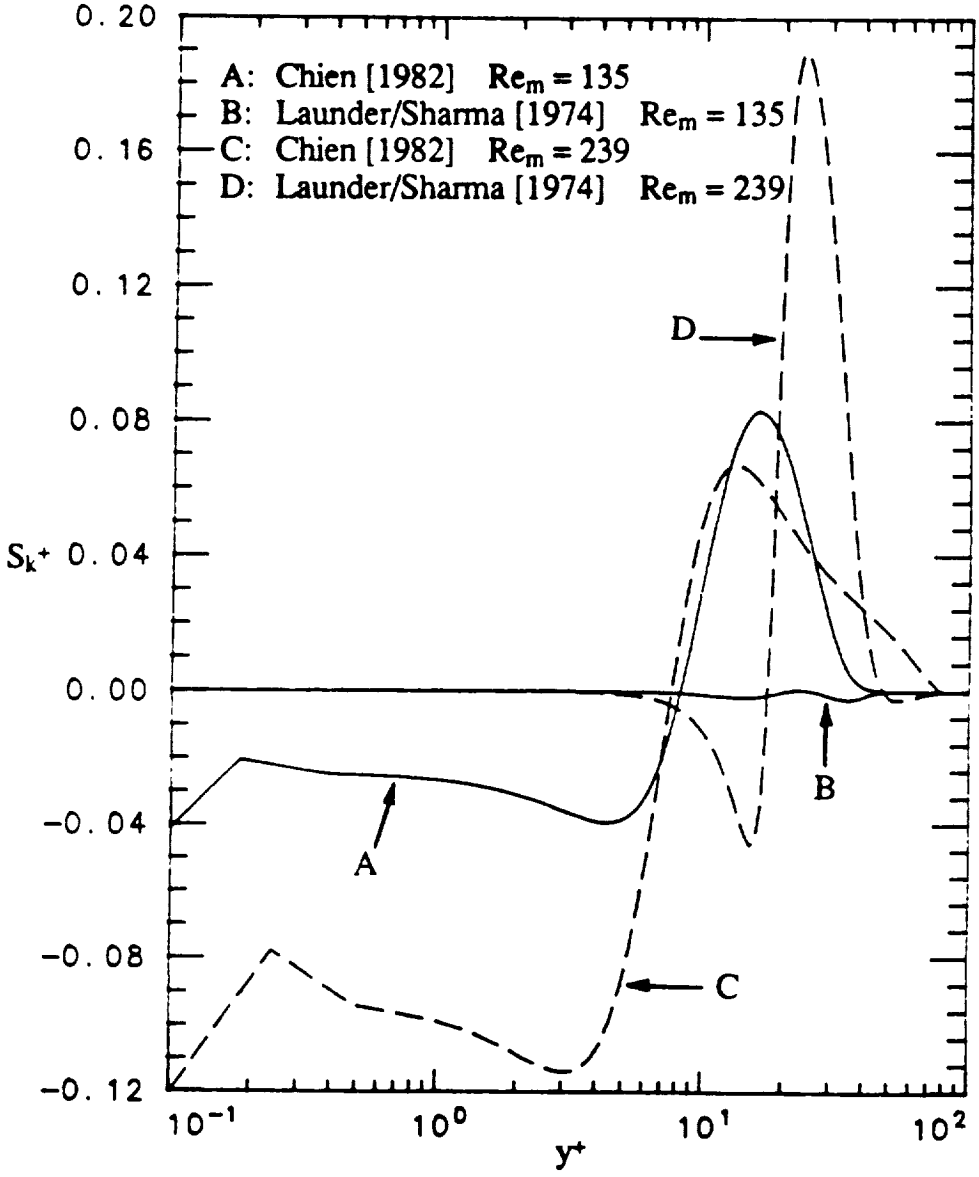

Figure 4.16. Turbulent kinetic energy source term profiles at Re_m = 135 and 239 for the K. Y. Chien [1982] and the Launder and Sharma [1974] turbulence models.

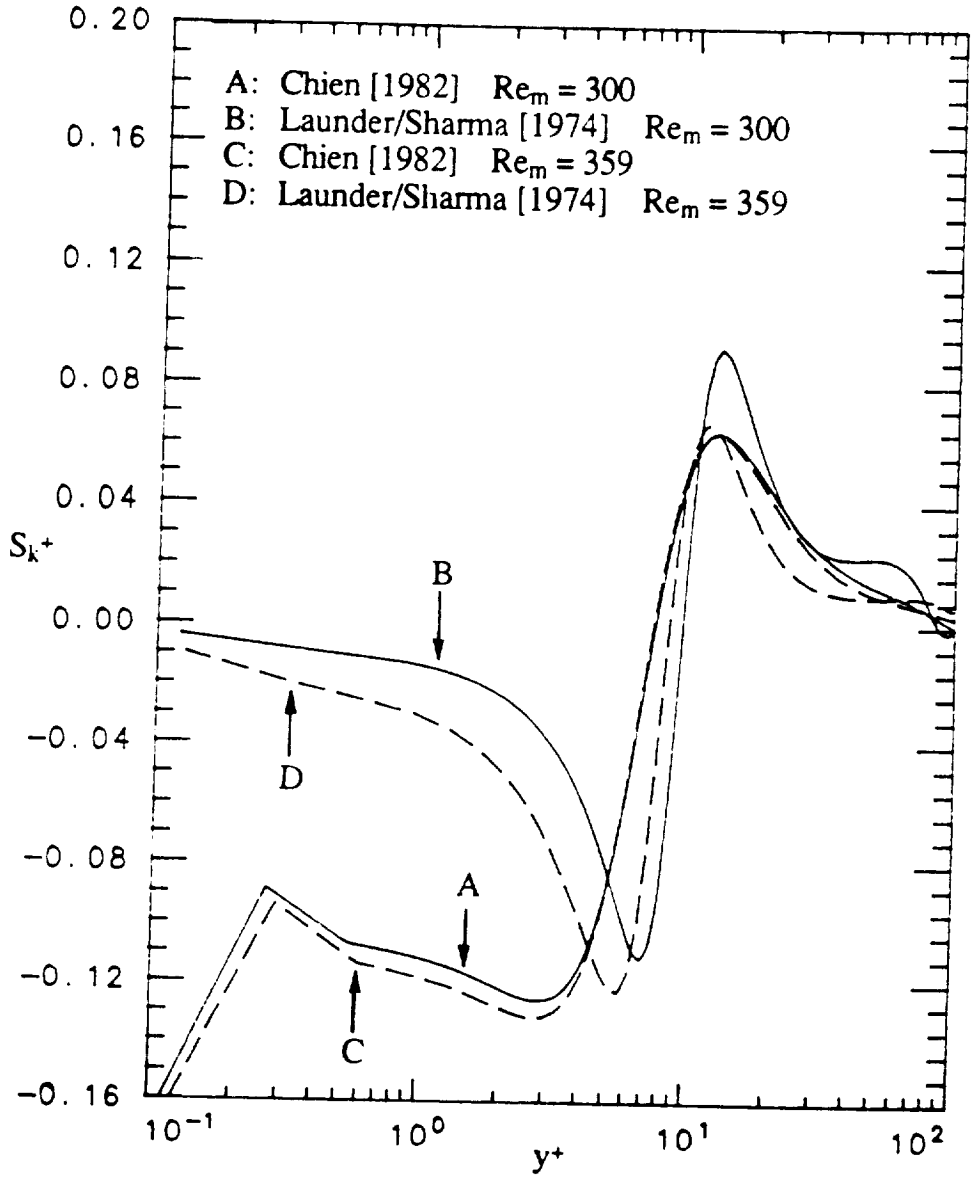

Figure 4.17. Turbulent kinetic energy source term profiles at $Re_m = 300$ and 359 for the K. Y. Chien [1982] and the Launder and Sharma [1974] turbulence models.

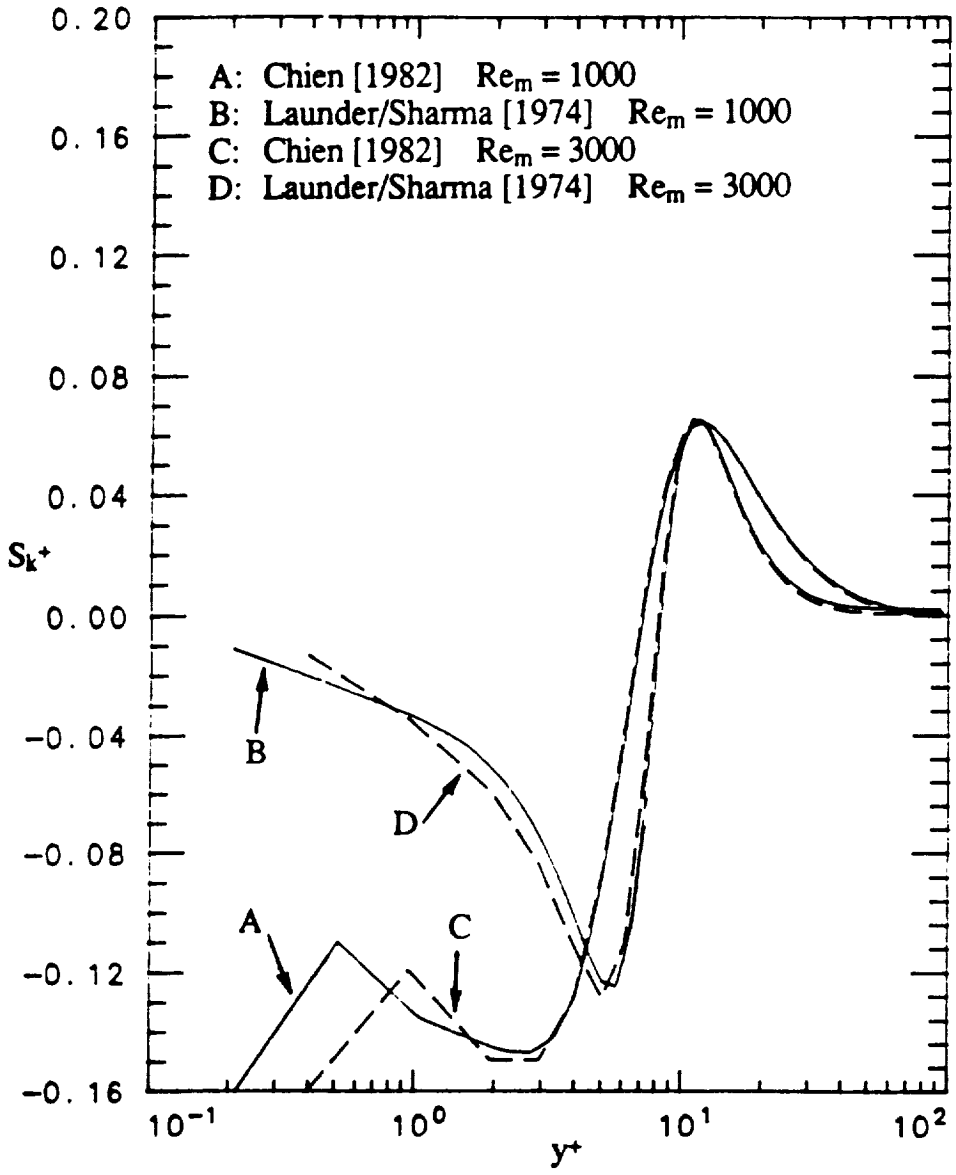

Figure 4.18. Turbulent kinetic energy source term profiles at $Re_m = 1000$ and 3000 for the K. Y. Chien [1982] and the Launder and Sharma [1974] turbulence models.

K. Y. Chien model predicts an ever increasing negative S_k^+ in the very near-wall region. The source of this increasing negative S_k^+ is due to the low-Reynolds number term (D) in equation (4.8), which as shown in equation (2.43) contains a $1/y^2$ term which becomes large as $y \rightarrow 0$.

Figures 4.19 to 4.22 are profiles of S_ε^+ versus y^+ at the momentum Reynolds numbers specified in Table 4.1. As with the S_k^+ profiles, Figure 4.19 shows that S_ε^+ develops more rapidly for the K. Y. Chien model than for the Launder and Sharma model in the laminar region (Re_m = 30 and 60). As shown in Figure 4.16, the start of transition for the K. Y. Chien and Launder and Sharma turbulence models are also reflected in Figure 4.20 with a rapid rise in S_ε^+. Figure 4.22 shows that for a fully turbulent boundary layer, the peak region of the S_ε^+ profile is larger and further from the wall for the Launder and Sharma turbulence model than for the K. Y. Chien turbulence model. This peak region for the Launder and Sharma model is at approximately y^+ = 10, while for the K. Y. Chien model the peak region is at y^+ = 8. The source term development, shown in Figures 4.15 to 4.22, is reflected in the development of the k^+ and ε^+ profiles.

Figures 4.23 to 4.26 are the k^+ profiles at the momentum Reynolds numbers specified in Table 4.1. Figure 4.23 shows a comparison of the degree to which the k^+ profile has developed in the laminar region for the K. Y. Chien turbulence model as compared to the Launder and Sharma turbulence model. The increased k^+ profile for the K. Y. Chien turbulence model leads to an earlier start of transition than for the Launder and Sharma model. Figure 4.24 shows the rapid growth of the k^+ profile for the K. Y. Chien model once transition has started, while for a fully turbulent boundary layer (Figure 4.26) the k^+ profiles are relatively constant. The cause of the increased development in the k^+ profile is explained by examining the turbulent viscosity distribution for both turbulence models.

Figures 4.27 to 4.30 are the ε^+ profiles at the momentum Reynolds numbers specified in Table 4.1. As expected, with an increased k^+ distribution in the

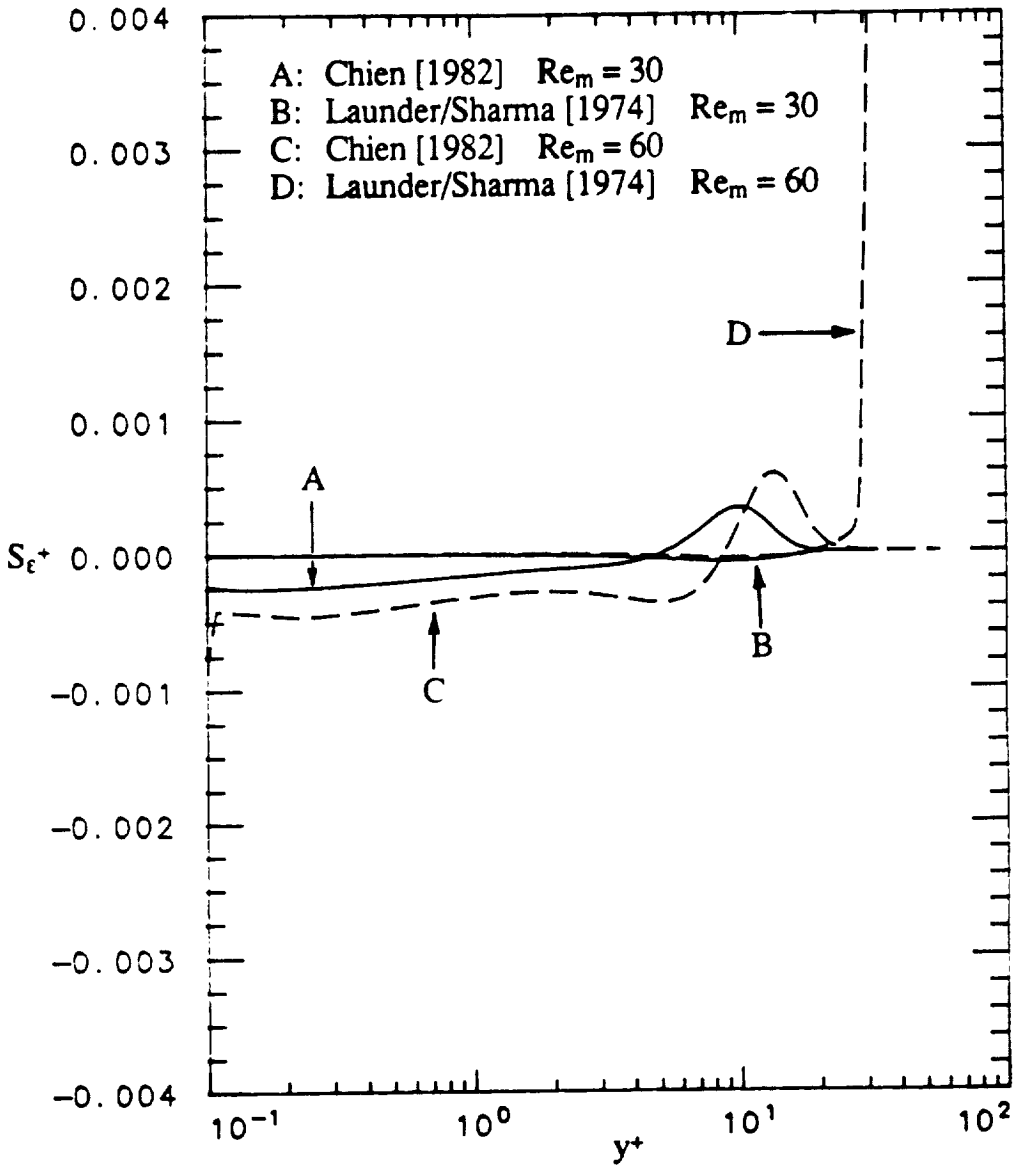

Figure 4.19. Turbulent dissipation rate source term profiles at $Re_m = 30$ and 60 for the K. Y. Chien [1982] and the Launder and Sharma [1974] turbulence models.

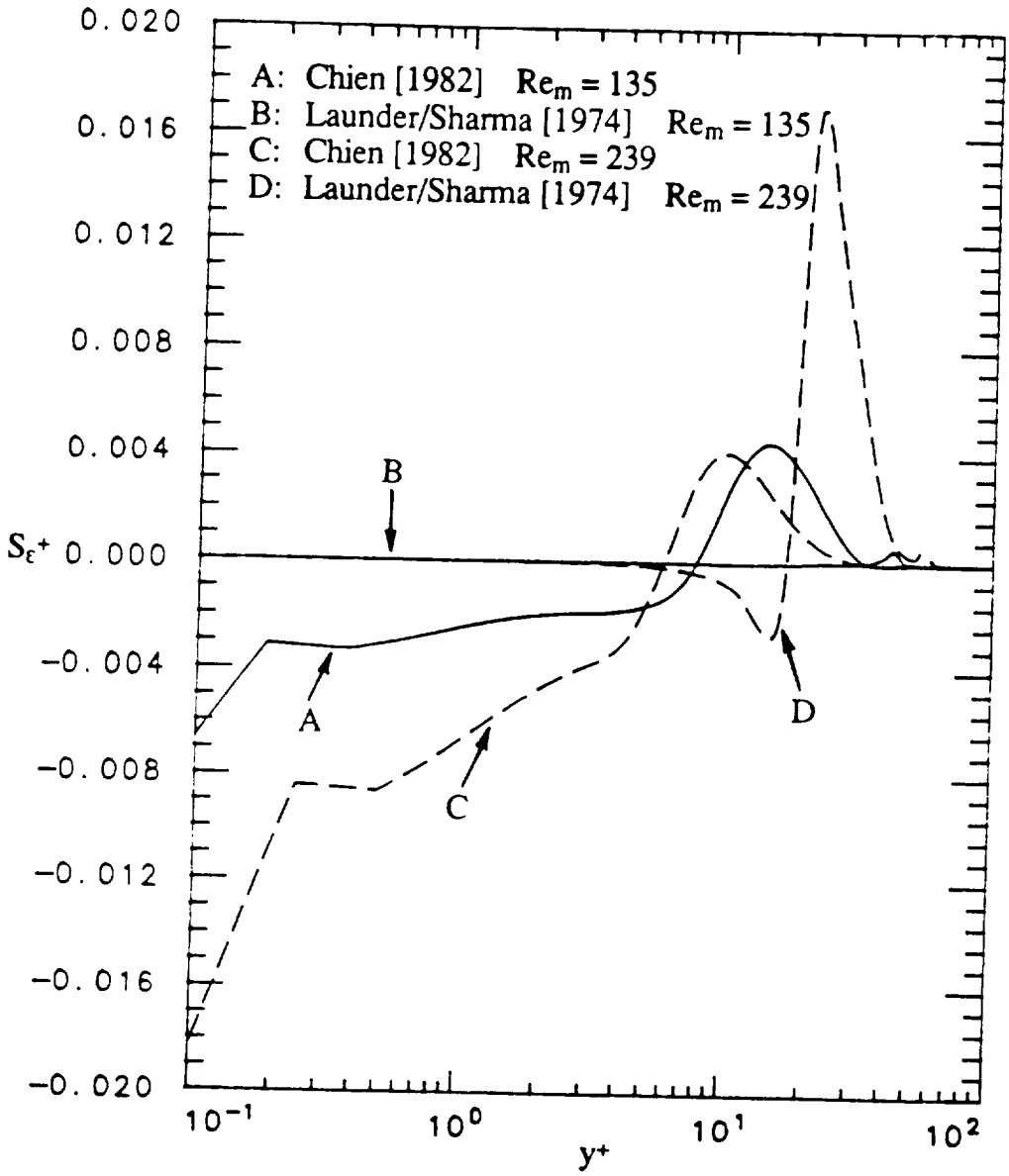

Figure 4.20. Turbulent dissipation rate source term profiles at $Re_m = 135$ and 239 for the K. Y. Chien [1982] and the Launder and Sharma [1974] turbulence models.

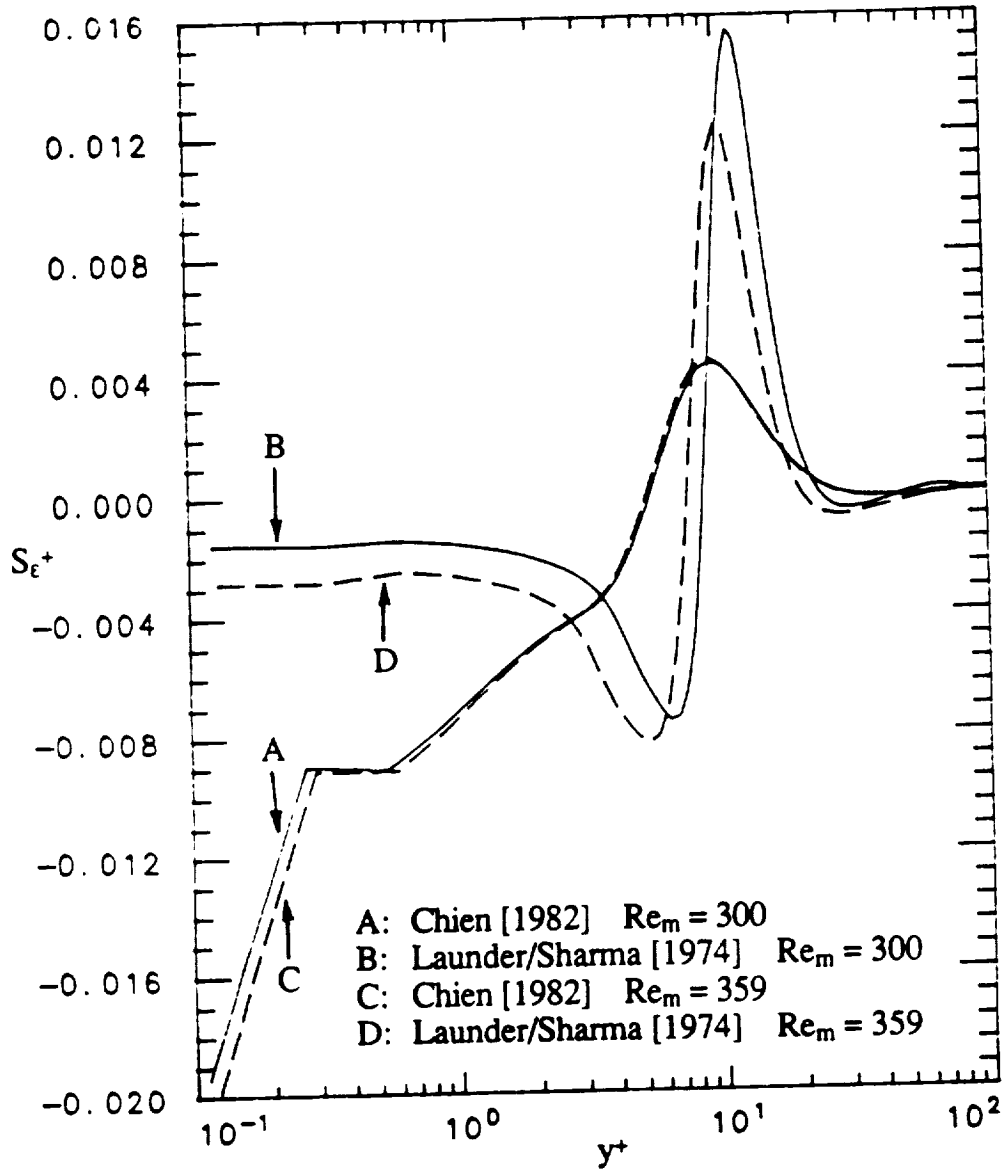

Figure 4.21. Turbulent dissipation rate source term profiles at $Re_m = 300$ and 359 for the K. Y. Chien [1982] and the Launder and Sharma [1974] turbulence models.

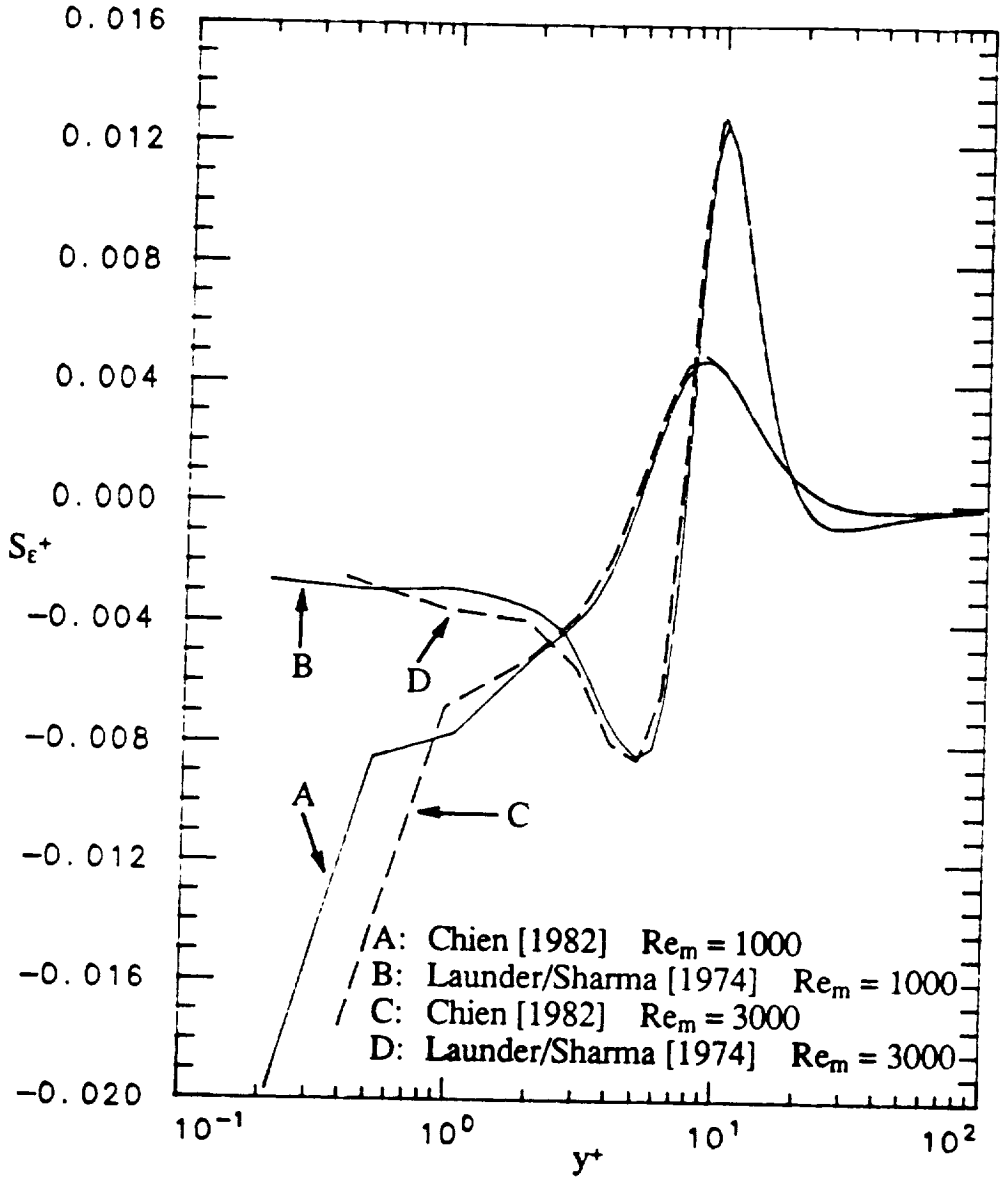

Figure 4.22. Turbulent dissipation rate source term profiles at $Re_m = 1000$ and 3000 for the K. Y. Chien [1982] and the Launder and Sharma [1974] turbulence models.

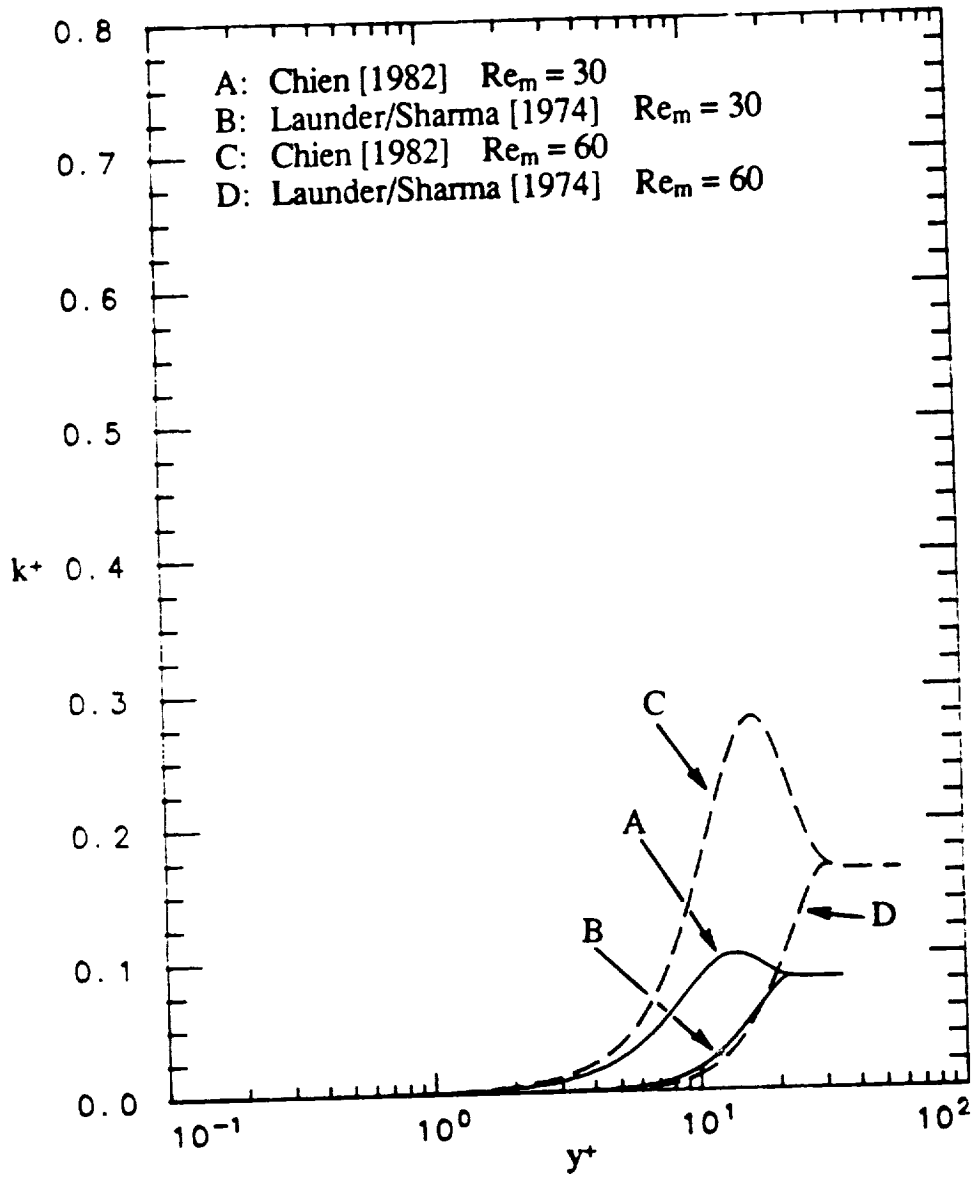

Figure 4.23. Turbulent kinetic energy profiles at $Re_m = 30$ and 60 for the K. Y. Chien [1982] and the Launder and Sharma [1974] turbulence models.

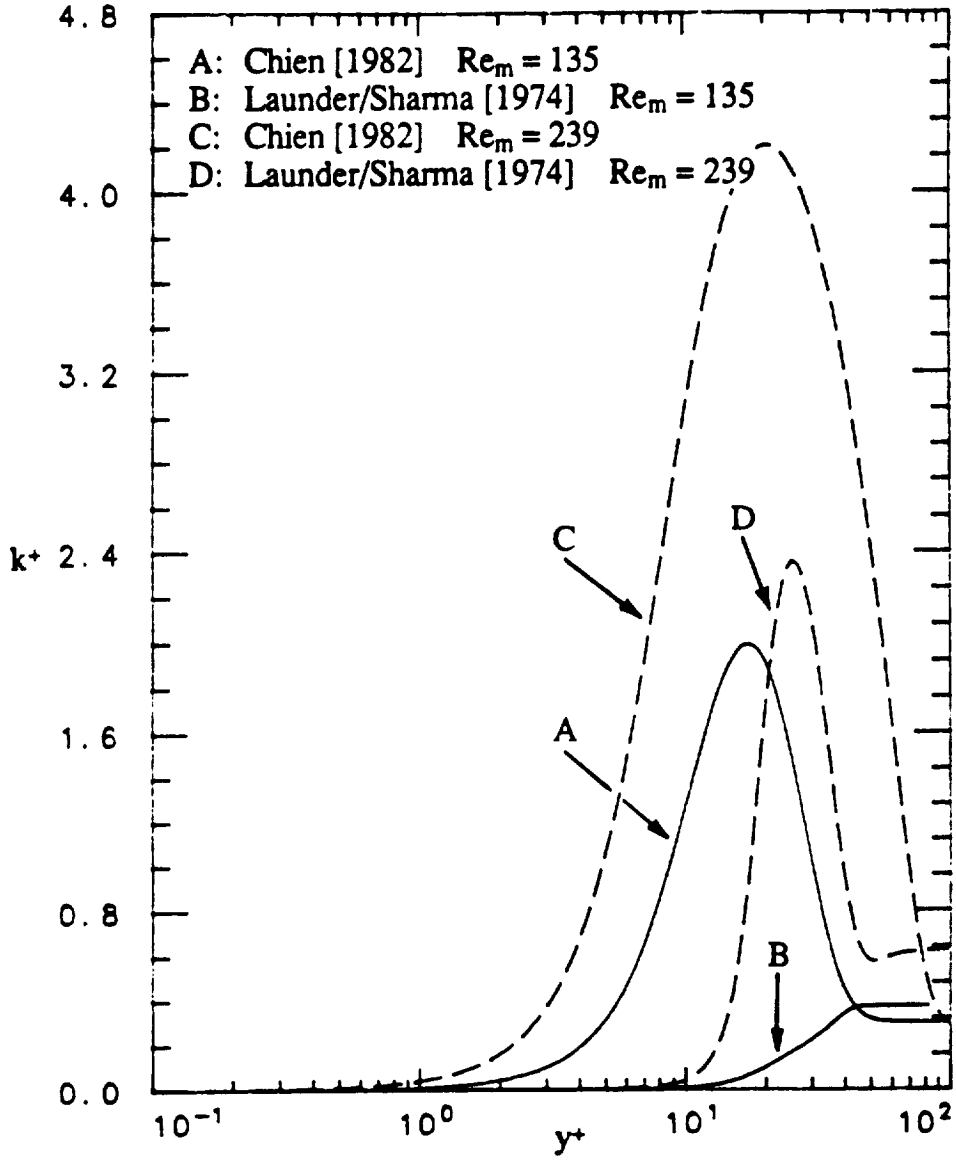

Figure 4.24. Turbulent kinetic energy profiles at $Re_m = 135$ and 239 for the K. Y. Chien [1982] and the Launder and Sharma [1974] turbulence models.

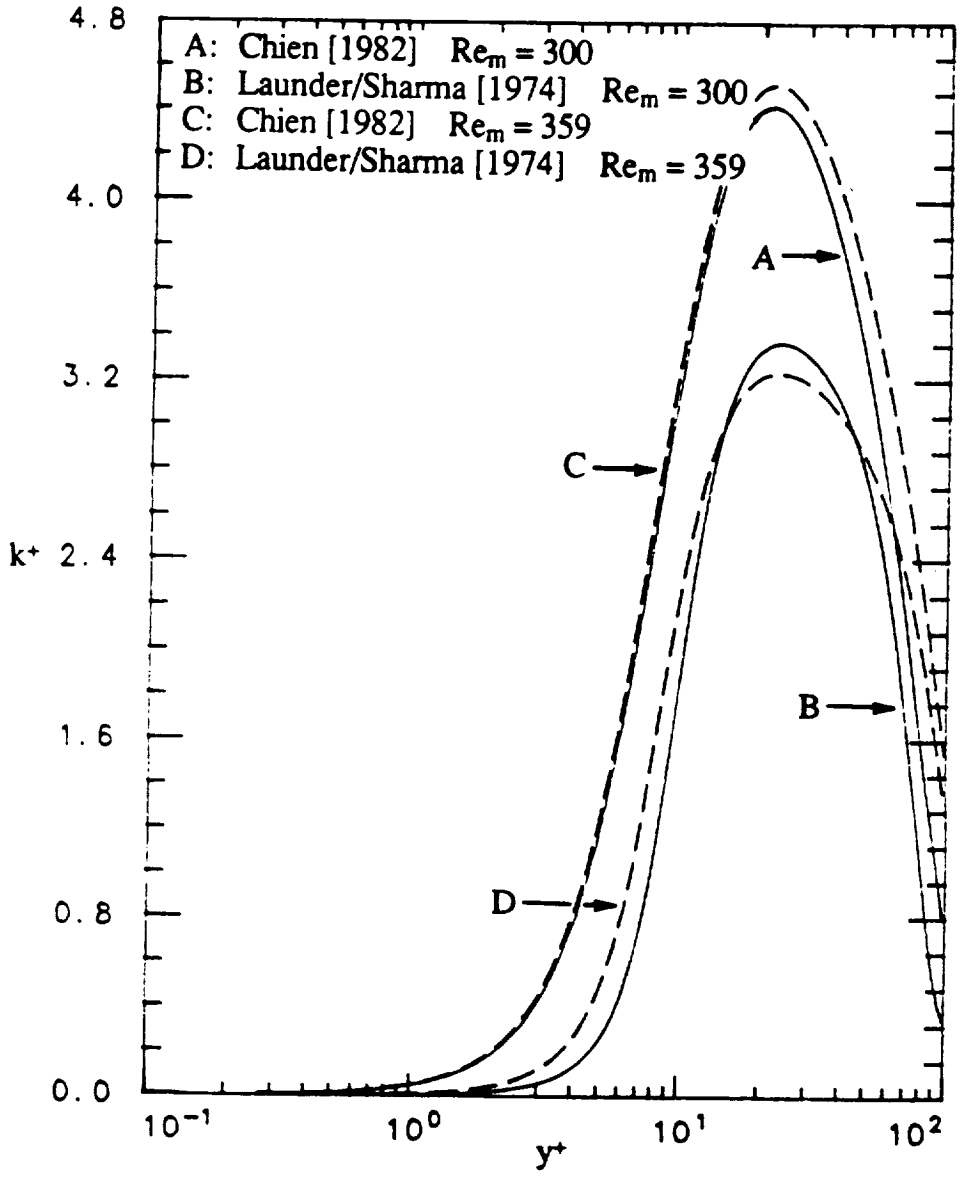

Figure 4.25. Turbulent kinetic energy profiles at $Re_m = 300$ and 359 for the K. Y. Chien [1982] and the Launder and Sharma [1974] turbulence models.

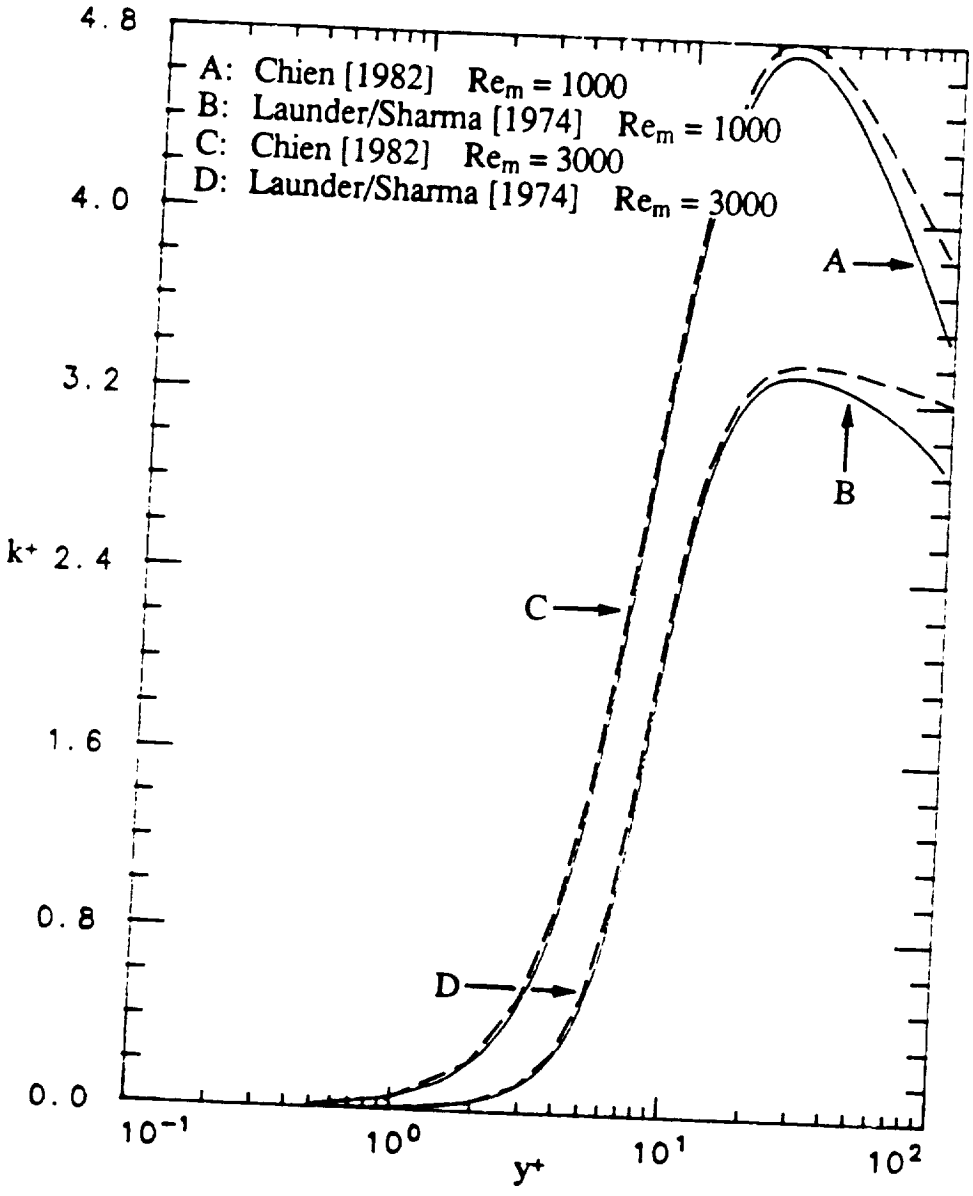

Figure 4.26. Turbulent kinetic energy profiles at $Re_m = 1000$ and 3000 for the K. Y. Chien [1982] and the Launder and Sharma [1974] turbulence models.

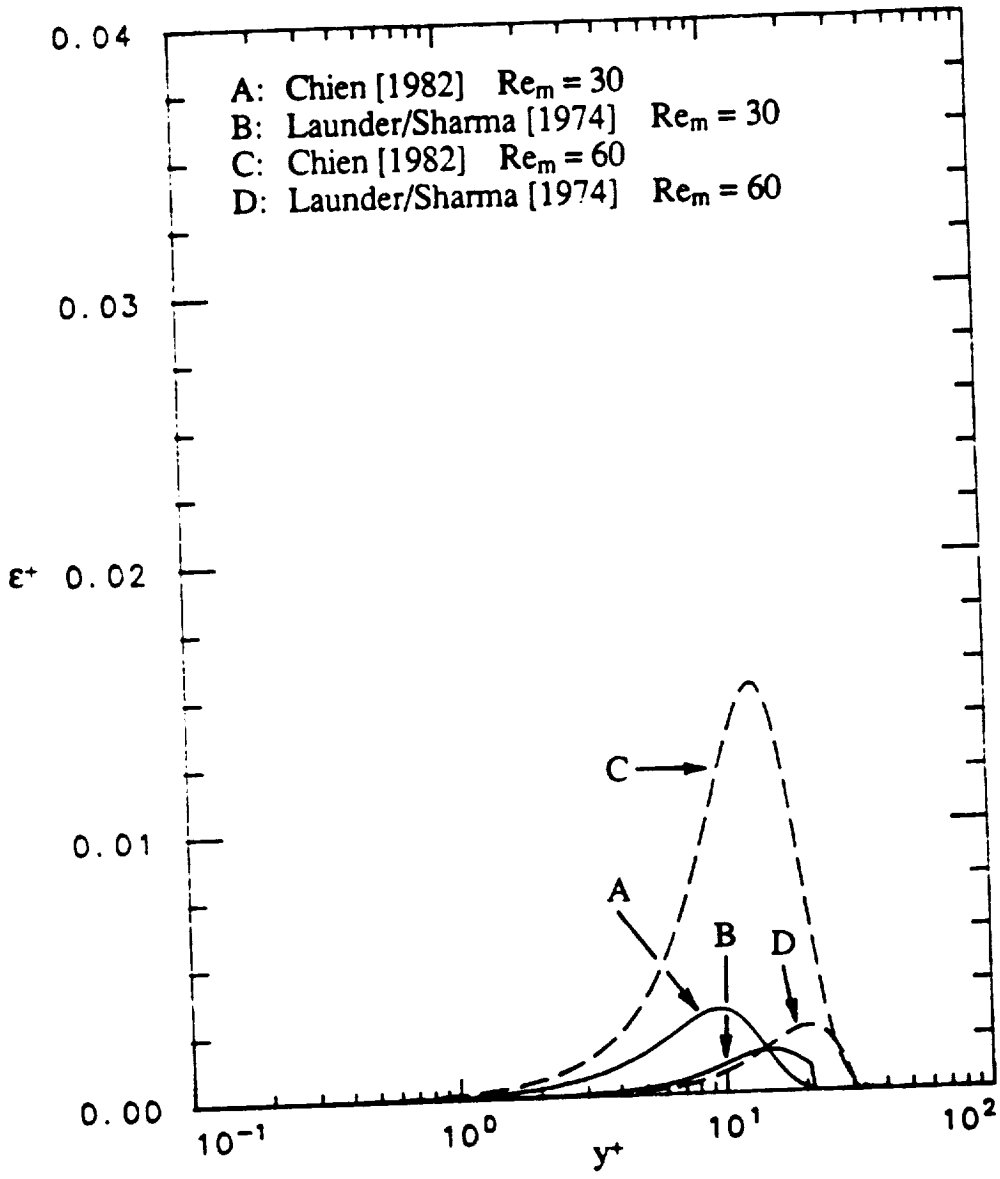

Figure 4.27. Turbulent dissipation rate profiles at $Re_m = 30$ and 60 for the K. Y. Chien [1982] and the Launder and Sharma [1974] turbulence models.

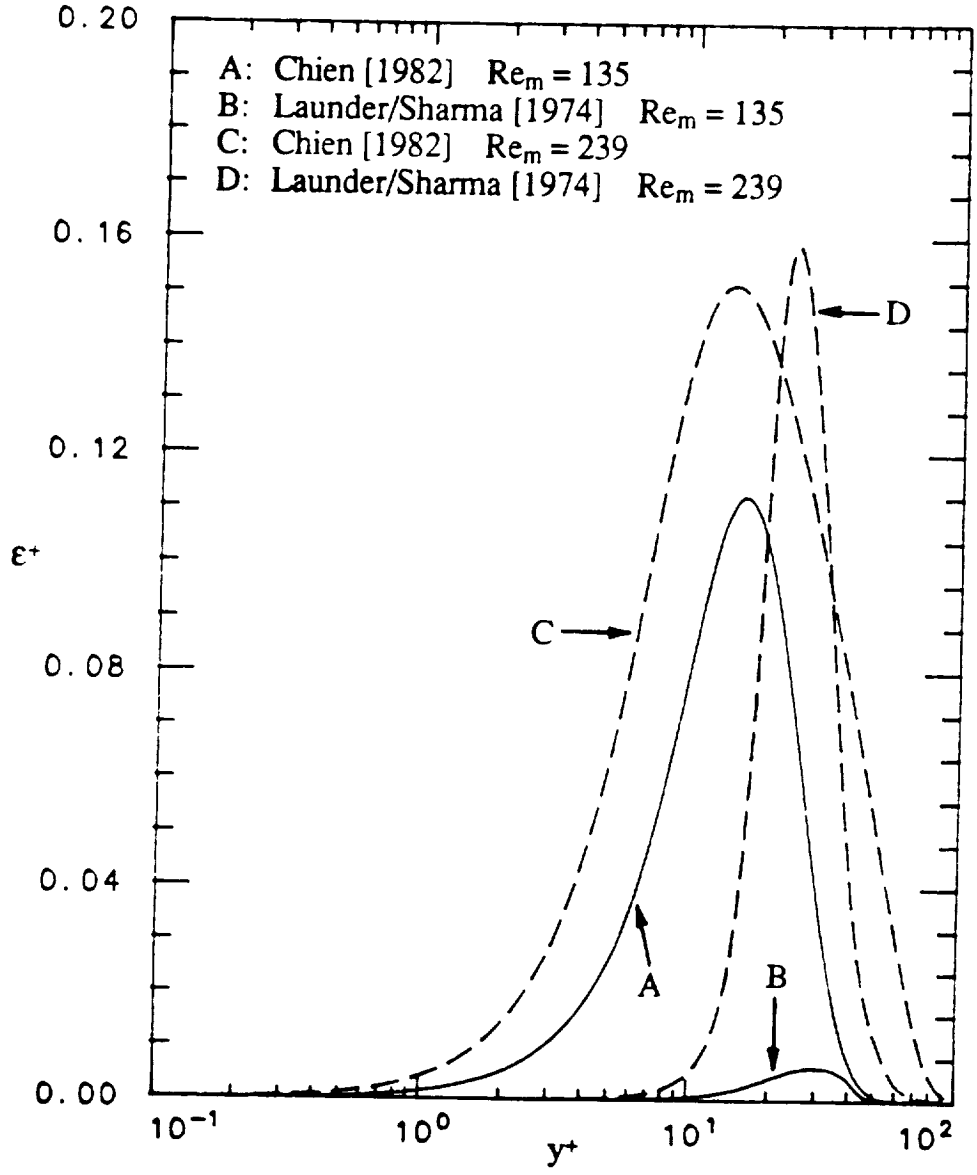

Figure 4.28. Turbulent dissipation rate profiles at $Re_m = 135$ and 239 for the K. Y. Chien [1982] and the Launder and Sharma [1974] turbulence models.

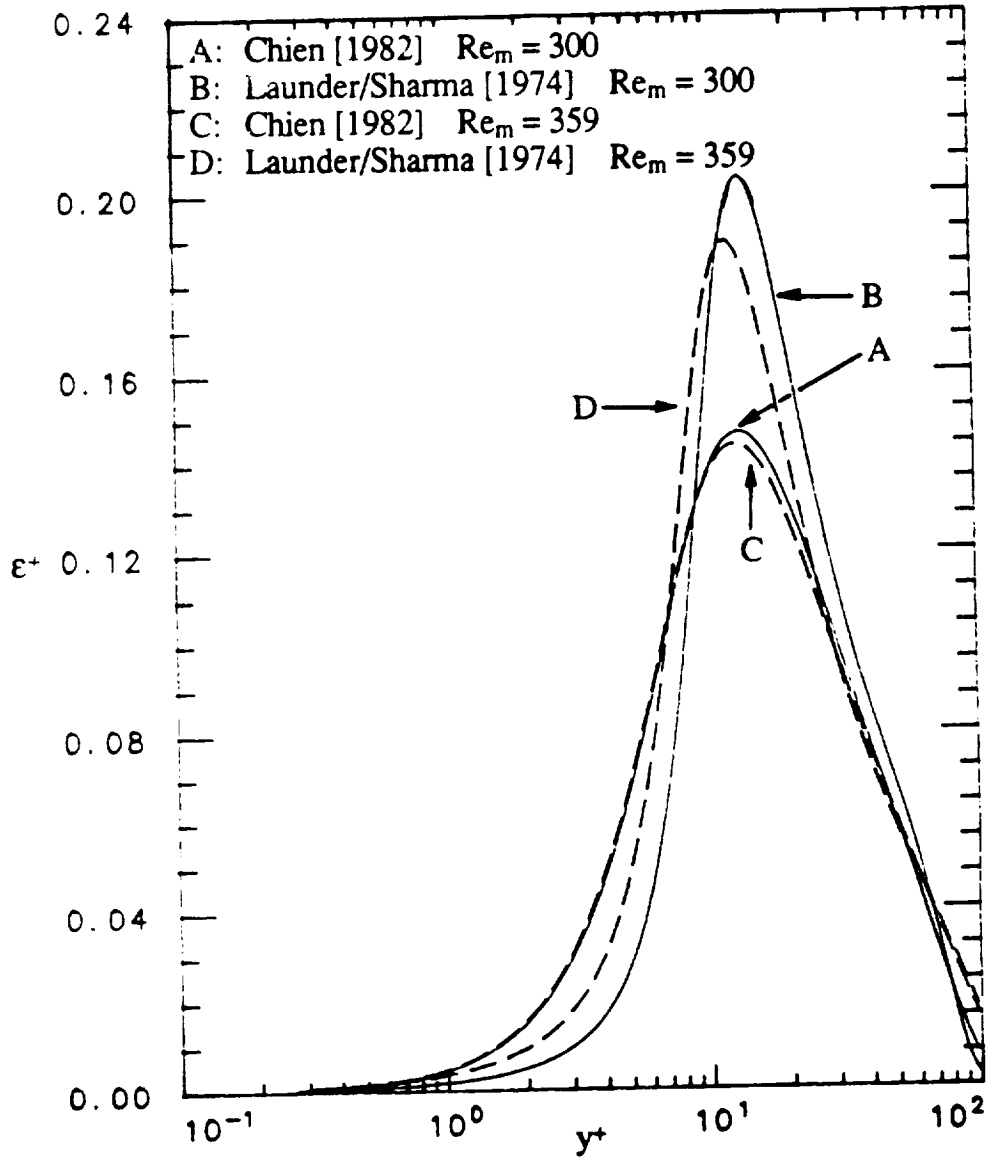

Figure 4.29. Turbulent dissipation rate profiles at $Re_m = 300$ and 359 for the K. Y. Chien [1982] and the Launder and Sharma [1974] turbulence models.

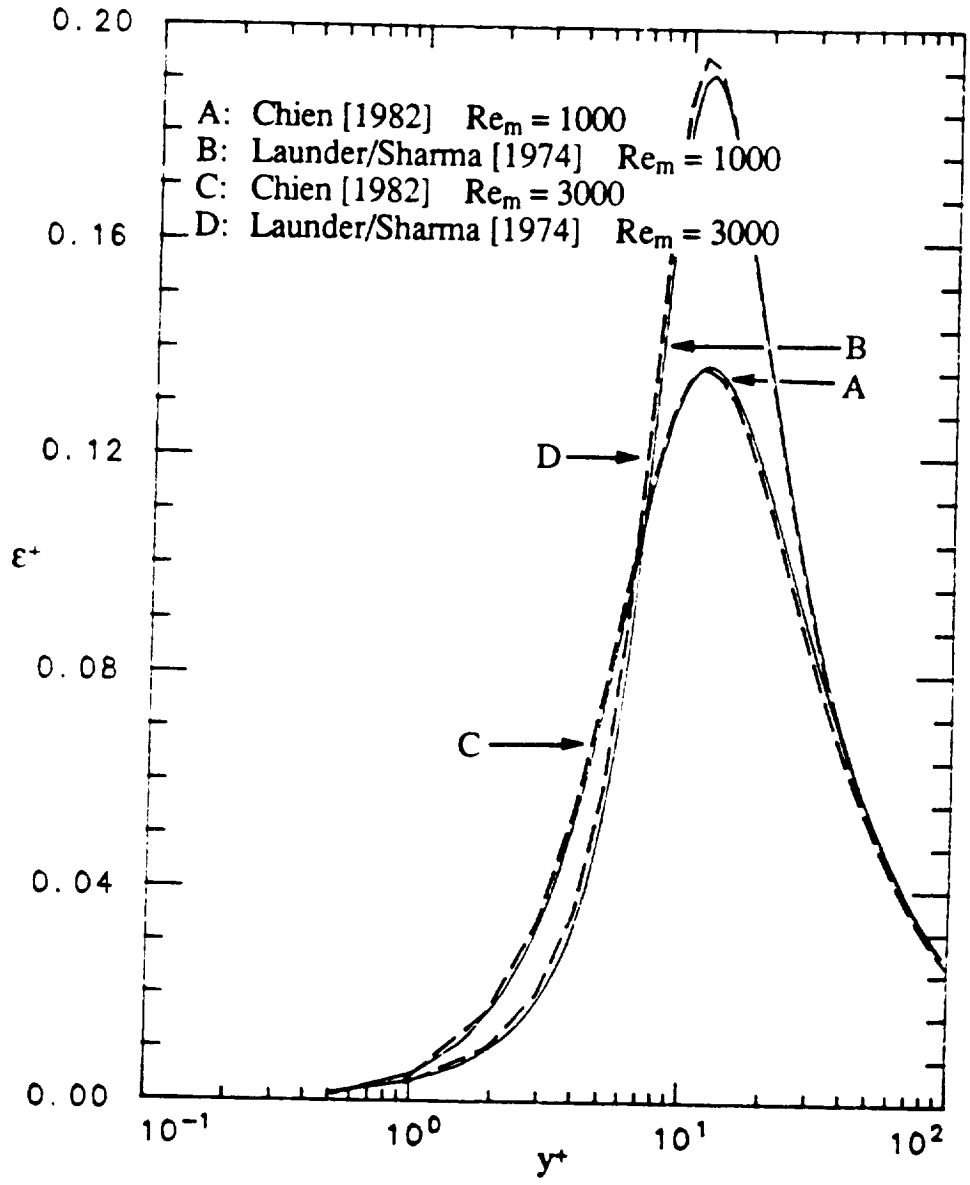

Figure 4.30. Turbulent dissipation rate profiles at Re_m = 1000 and 3000 for the K. Y. Chien [1982] and the Launder and Sharma [1974] turbulence models.

laminar region, the ε^+ distribution for the K. Y. Chien turbulence model is more developed than for the Launder and Sharma turbulence model as shown in Figure 4.27. For a fully turbulent boundary layer, shown in Figure 4.30, the ε^+ profile is larger for the Launder and Sharma model than for the K. Y. Chien model, while in Figure 4.26, the k^+ profile for the K. Y. Chien model is larger than the k^+ profile for the Launder and Sharma model.

Figures 4.31 to 4.34 are profiles of ν_t/ν versus y^+ at the momentum Reynolds numbers specified in Table 4.1. From Figure 4.31 it is noted that for $7 \leq y^+ \leq 20$ the following is true

$$\frac{\nu_t}{\nu_C} > \frac{\nu_t}{\nu_{LS}} \tag{4.12}$$

where C and LS correspond to K. Y. Chien and Launder and Sharma respectively. With ν_t for the K. Y. Chien model greater than ν_t for Launder and Sharma model, the near-wall production of TKE for the K. Y. Chien model will be greater than for the Launder and Sharma model. However, by the time the boundary layer becomes fully turbulent, the ν_t/ν distribution for both the K. Y. Chien and Launder and Sharma turbulence models become the same, as shown in Figure 4.34. From equation (2.17) the turbulent viscosity may be written as

$$\nu_t = C_\mu f_\mu \frac{k^2}{\hat{\varepsilon}} . \tag{4.13}$$

Using the definition of the turbulent Reynolds number, $Re_t = k^2/\hat{\varepsilon}\nu$, equation (4.13) may be rewritten as follows

$$\frac{\nu_t}{\nu} = C_\mu f_\mu Re_t . \tag{4.14}$$

By examining equation (4.14), the characteristics of ν_t/ν are defined by examining the characteristics of f_μ and Re_t.

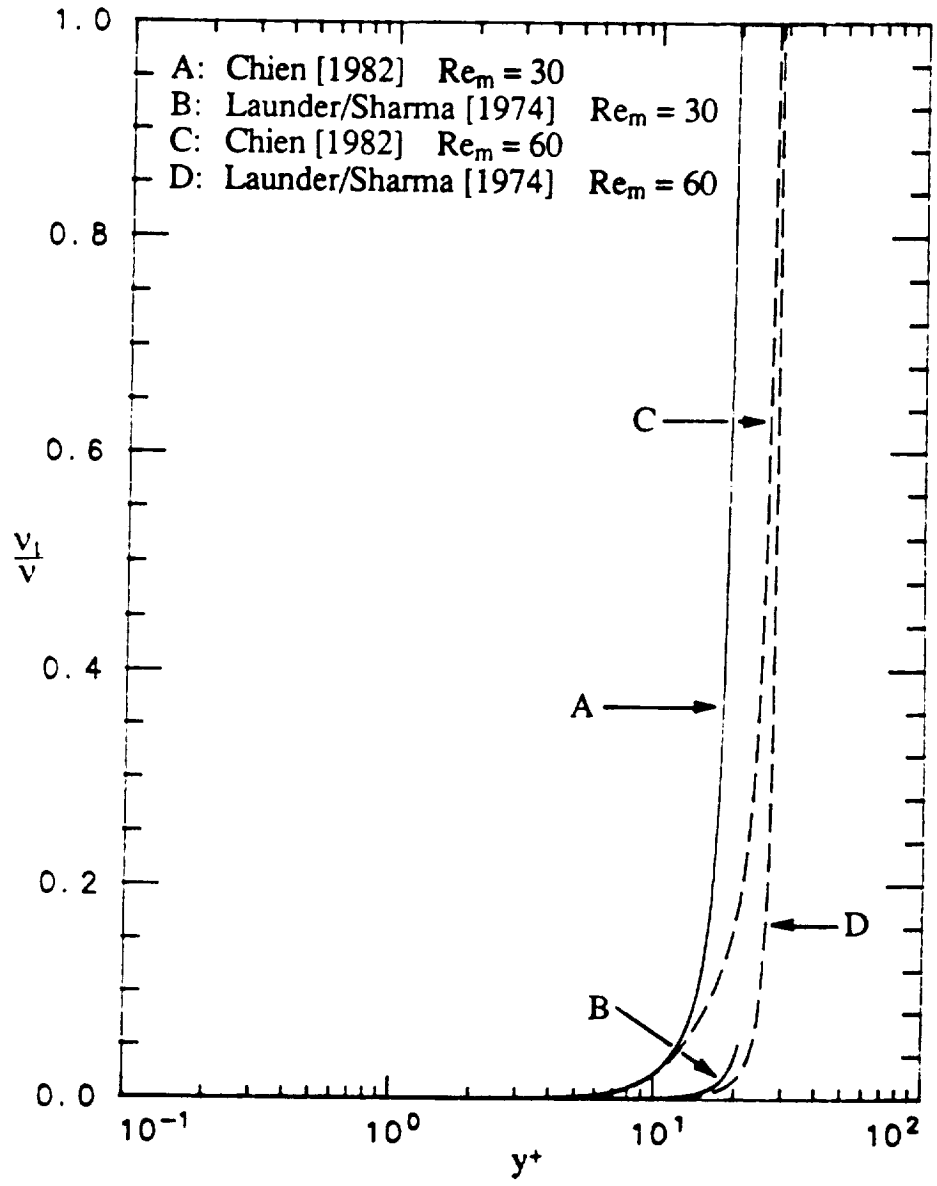

Figure 4.31. Eddy diffusivity profiles at $Re_m = 30$ and 60 for the K. Y. Chien [1982] and the Launder and Sharma [1974] turbulence models.

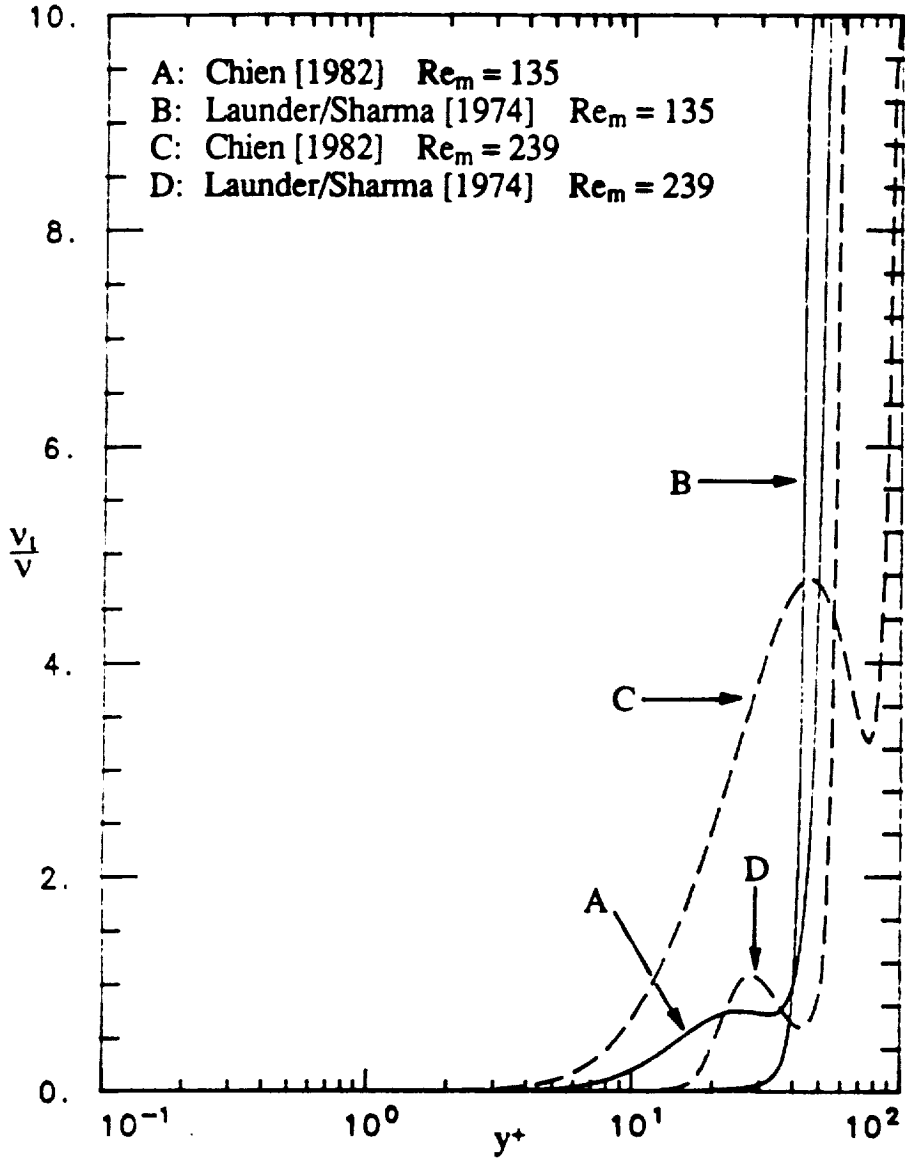

Figure 4.32. Eddy diffusivity profiles at $Re_m = 135$ and 239 for the K. Y. Chien [1982] and the Launder and Sharma [1974] turbulence models.

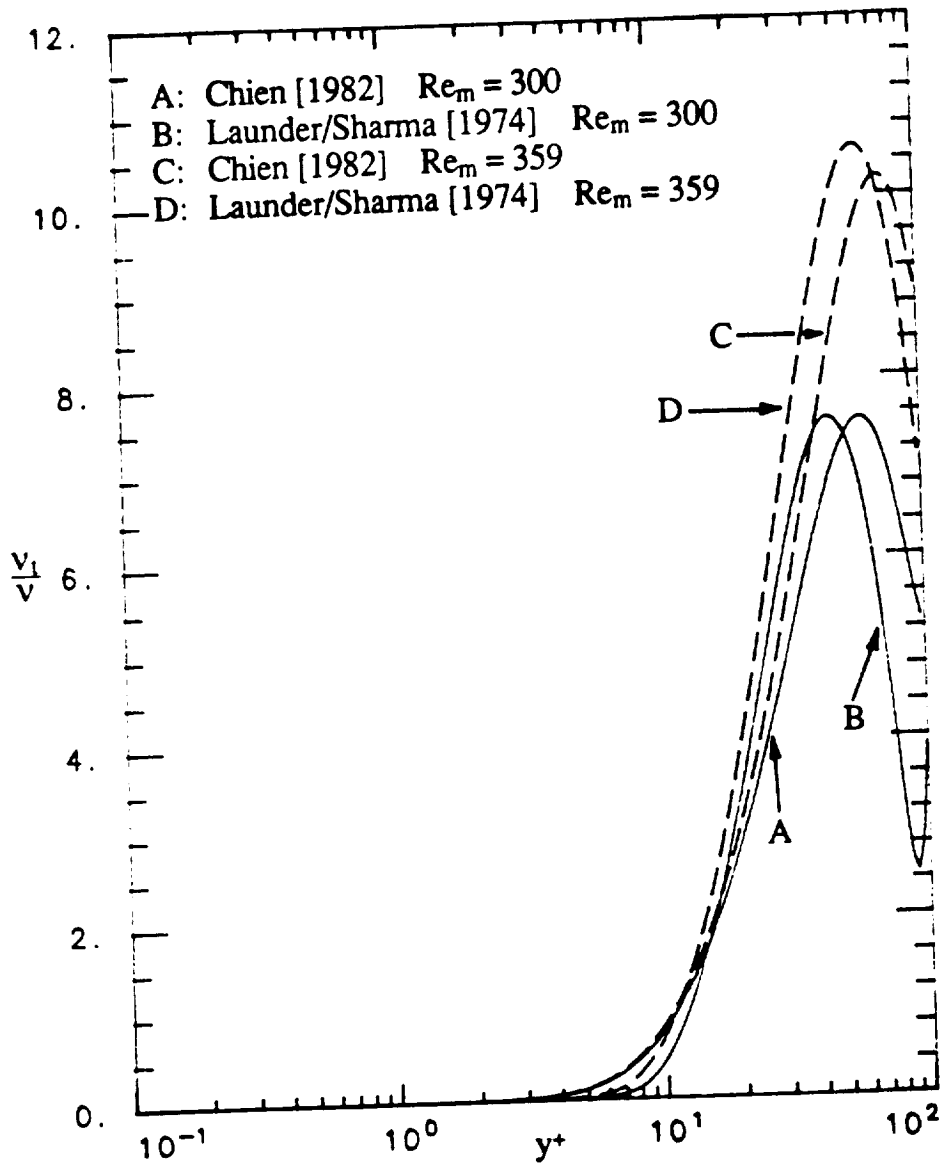

Figure 4.33. Eddy diffusivity profiles at $Re_m = 300$ and 359 for the K. Y. Chien [1982] and the Launder and Sharma [1974] turbulence models.

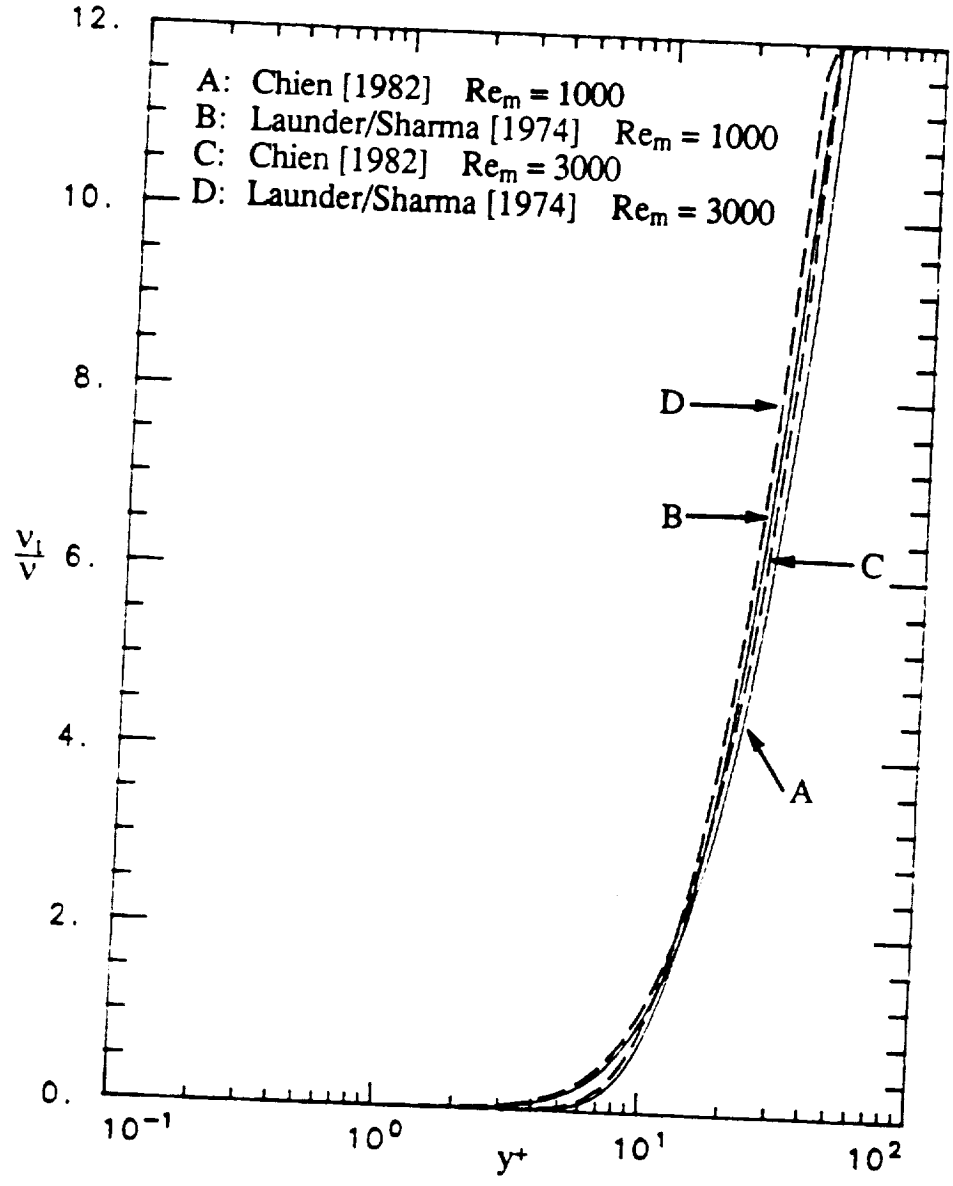

Figure 4.34. Eddy diffusivity profiles at $Re_m = 1000$ and 3000 for the K. Y. Chien [1982] and the Launder and Sharma [1974] turbulence models.

Figures 4.35 to 4.38 are profiles of Re_t versus y^+ for the momentum Reynolds numbers defined in Table 4.1. As shown in Figures 4.35 to 4.38, the turbulent Reynolds number for both the K. Y. Chien and Launder and Sharma turbulence models are not exactly the same but they reflect similar behavior. The turbulent Reynolds number is a ratio of the boundary layer TKE and TDR, therefore it is merely a reflection of the distribution of TKE and TDR governed by the solution of equations (2.19) and (2.20). It should be expected that the turbulent Reynolds number for both the K. Y. Chien and Launder and Sharma be approximately the same and not pose a direct influence on the calculation of ν_t/ν.

On the other hand, the f_μ function has a direct effect on the calculation of the turbulent viscosity. Figures 4.39 to 4.42 are profiles of f_μ versus y^+ for the momentum Reynolds numbers defined in Table 4.1. As shown in Figures 4.39 and 4.40, the following is noted,

$$f_{\mu,C} > f_{\mu,LS} \qquad \text{for } 3 < y^+ < 25 \text{ and } 0 < Re_m < 300. \qquad (4.15)$$

Equation (4.15) is the reason why the start of transition for the K. Y. Chien turbulence model is less than the start of transition for the Launder and Sharma turbulence model. For the K. Y. Chien two-equation model, a larger f_μ damping function in the near-wall region means ν_t will be larger in the near-wall region, which ultimately translates into an increase in the production of TKE in the near-wall region and an earlier start of transition (the first question posed earlier in this section).

To answer the second question posed in this section pertaining to the "damped" C_f distribution associated with the K. Y. Chien turbulence model, the form of the f_μ expression must be examined. The f_μ proposed by K. Y. Chien is only a function of y, as shown in equation (2.40). This means that the f_μ function has only one shape and varies only in the y-direction as the boundary layer grows,

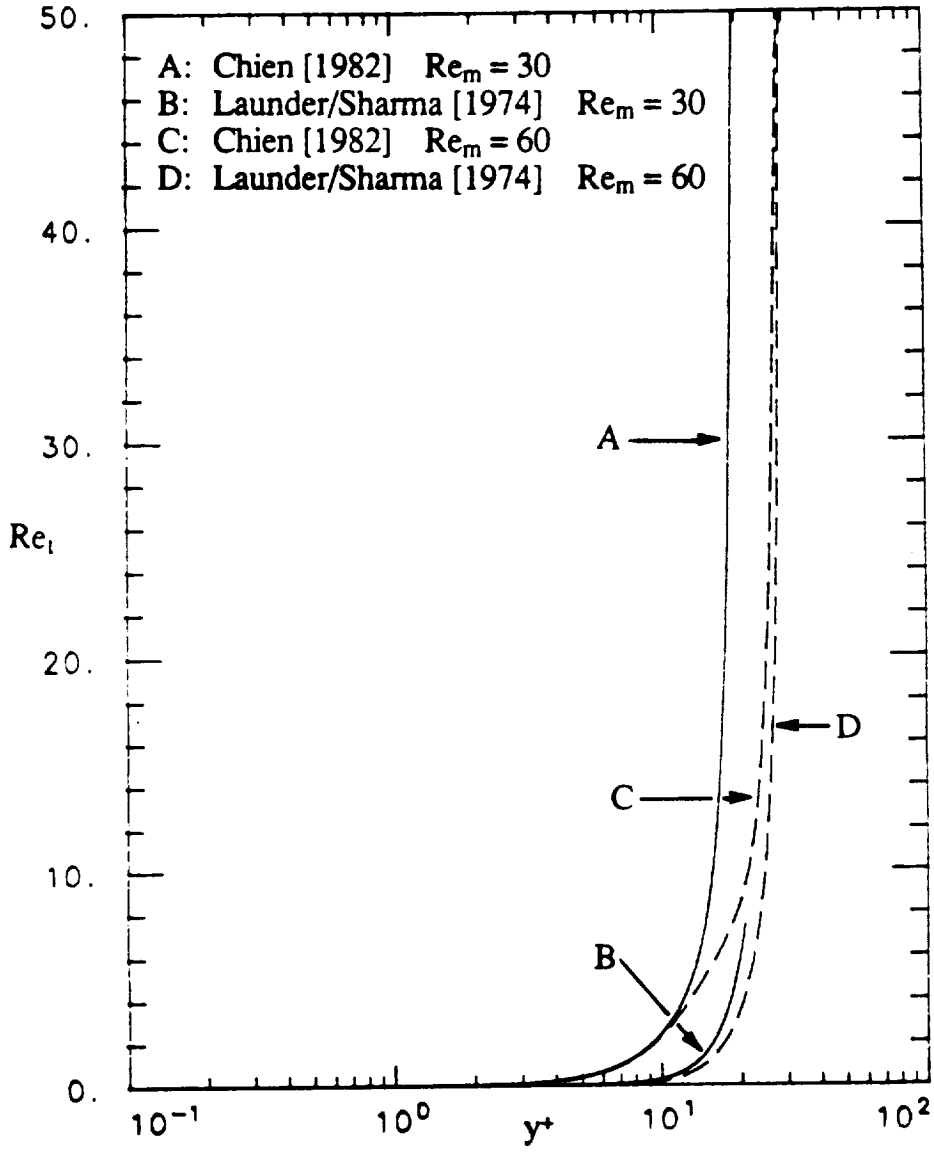

Figure 4.35. Turbulent Reynolds number profiles at Re_m = 30 and 60 for the K. Y. Chien [1982] and the Launder and Sharma [1974] turbulence models.

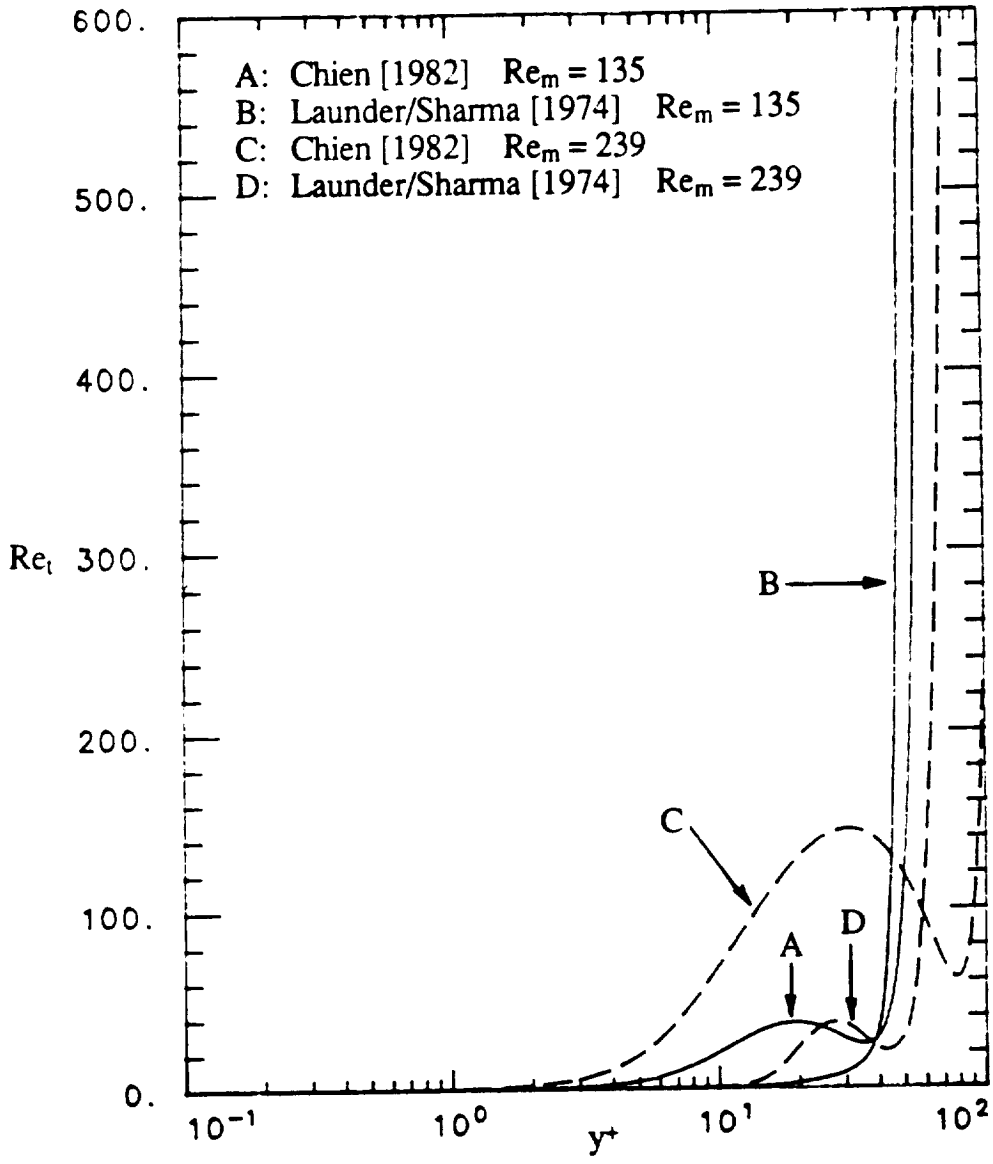

Figure 4.36. Turbulent Reynolds number profiles at Re_m = 135 and 239 for the K. Y. Chien [1982] and the Launder and Sharma [1974] turbulence models.

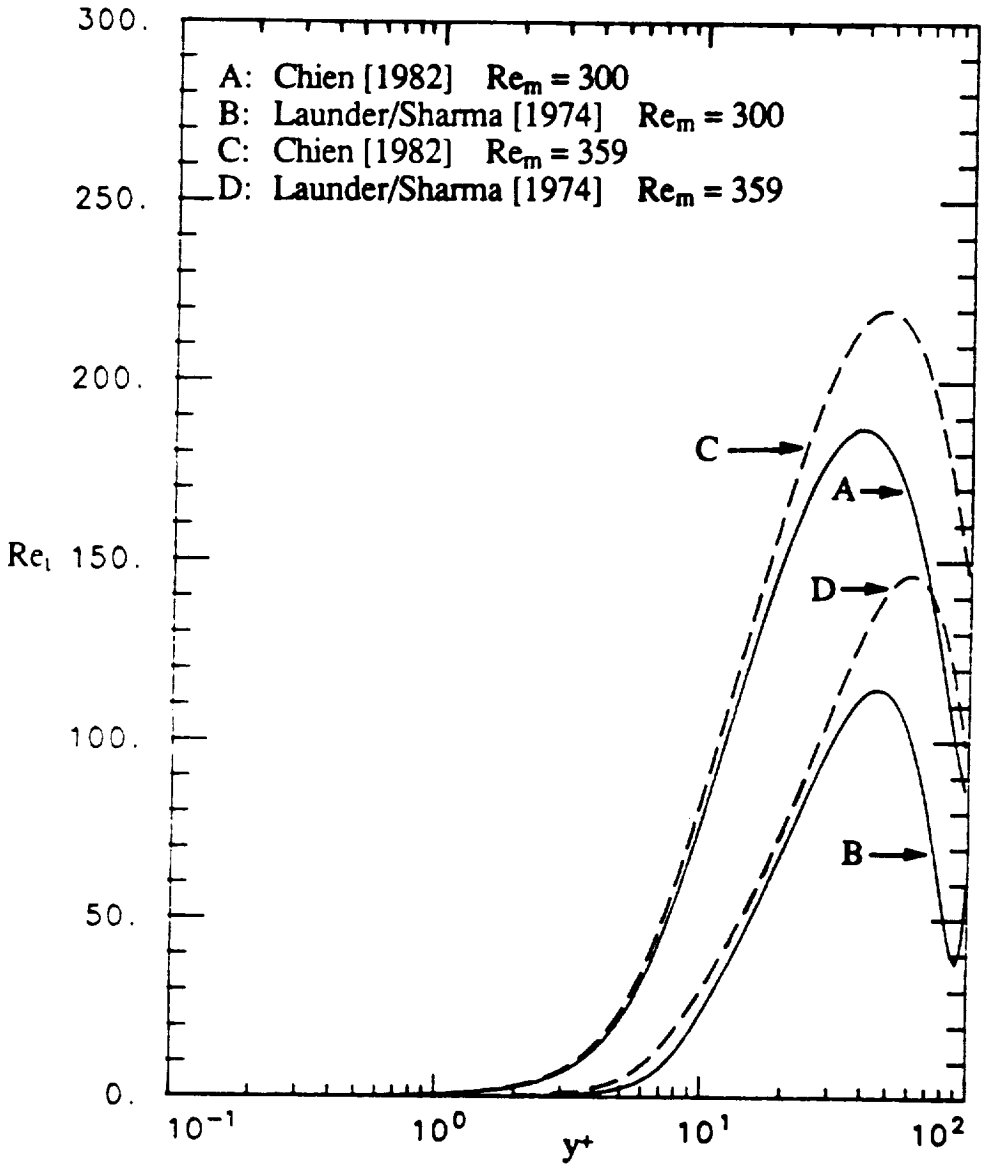

Figure 4.37. Turbulent Reynolds number profiles at $Re_m = 300$ and 359 for the K. Y. Chien [1982] and the Launder and Sharma [1974] turbulence models.

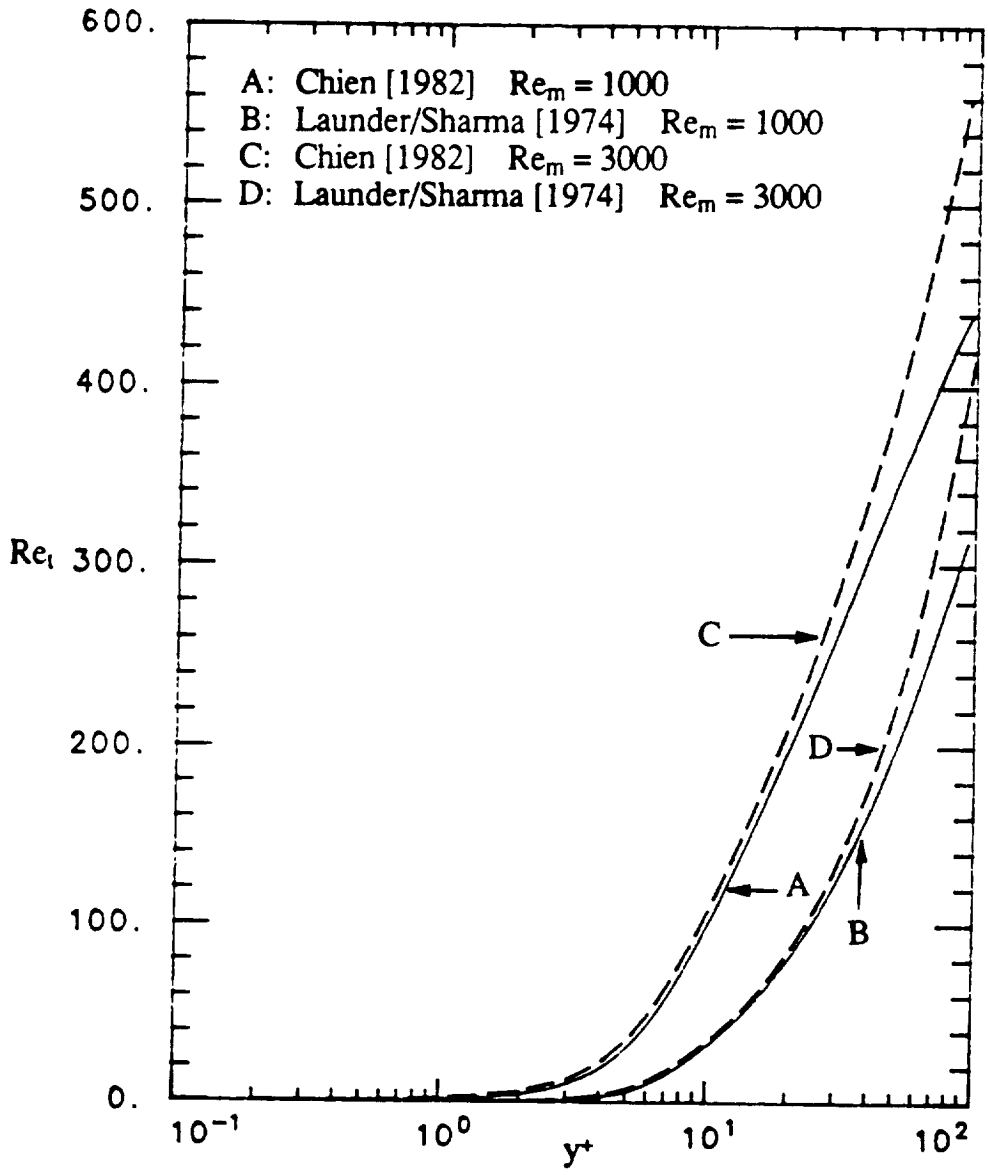

Figure 4.38. Turbulent Reynolds number profiles at $Re_m = 1000$ and 3000 for the K. Y. Chien [1982] and the Launder and Sharma [1974] turbulence models.

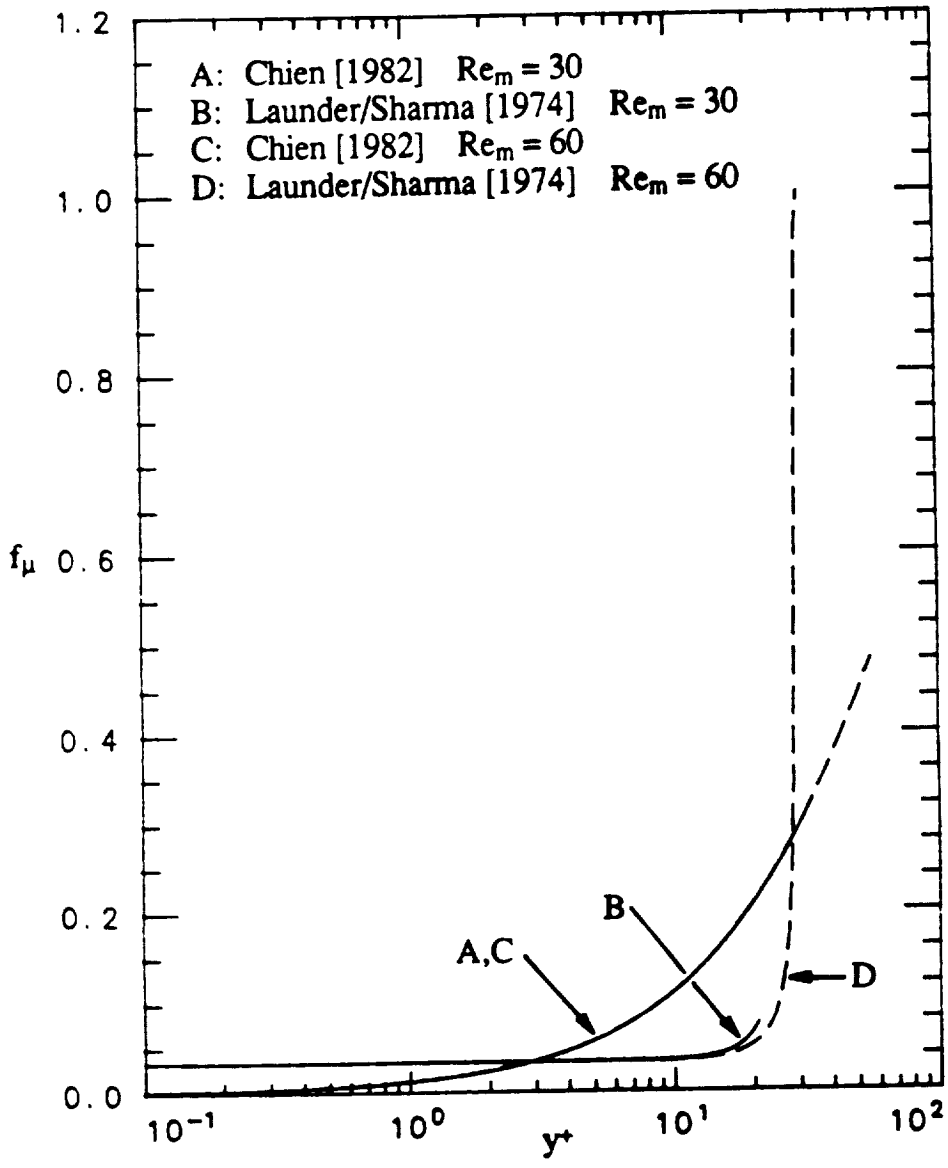

Figure 4.39. Turbulent viscosity damping function profiles at $Re_m = 30$ and 60 for the K. Y. Chien [1982] and the Launder and Sharma [1974] turbulence models.

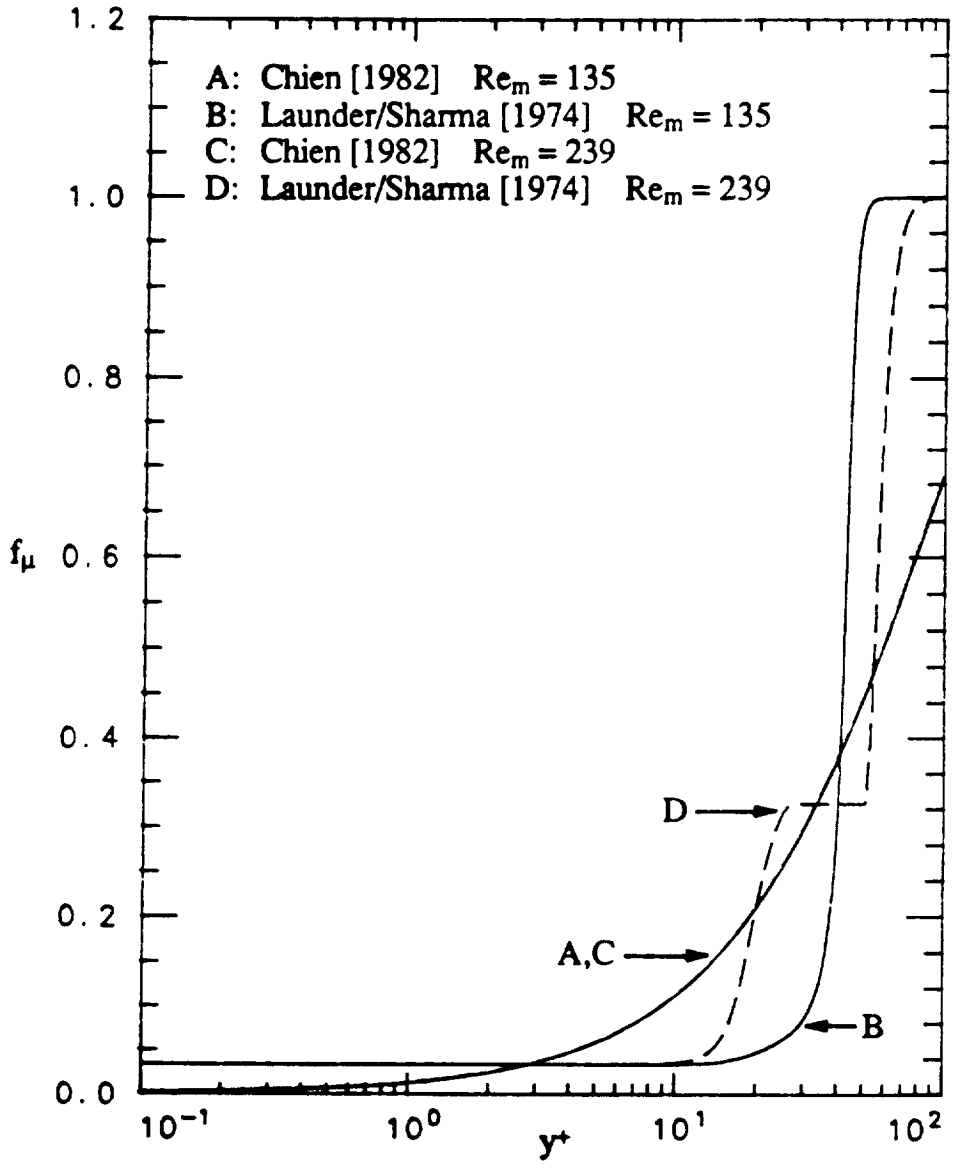

Figure 4.40. Turbulent viscosity damping function profiles at Re_m = 135 and 239 for the K. Y. Chien [1982] and the Launder and Sharma [1974] turbulence models.

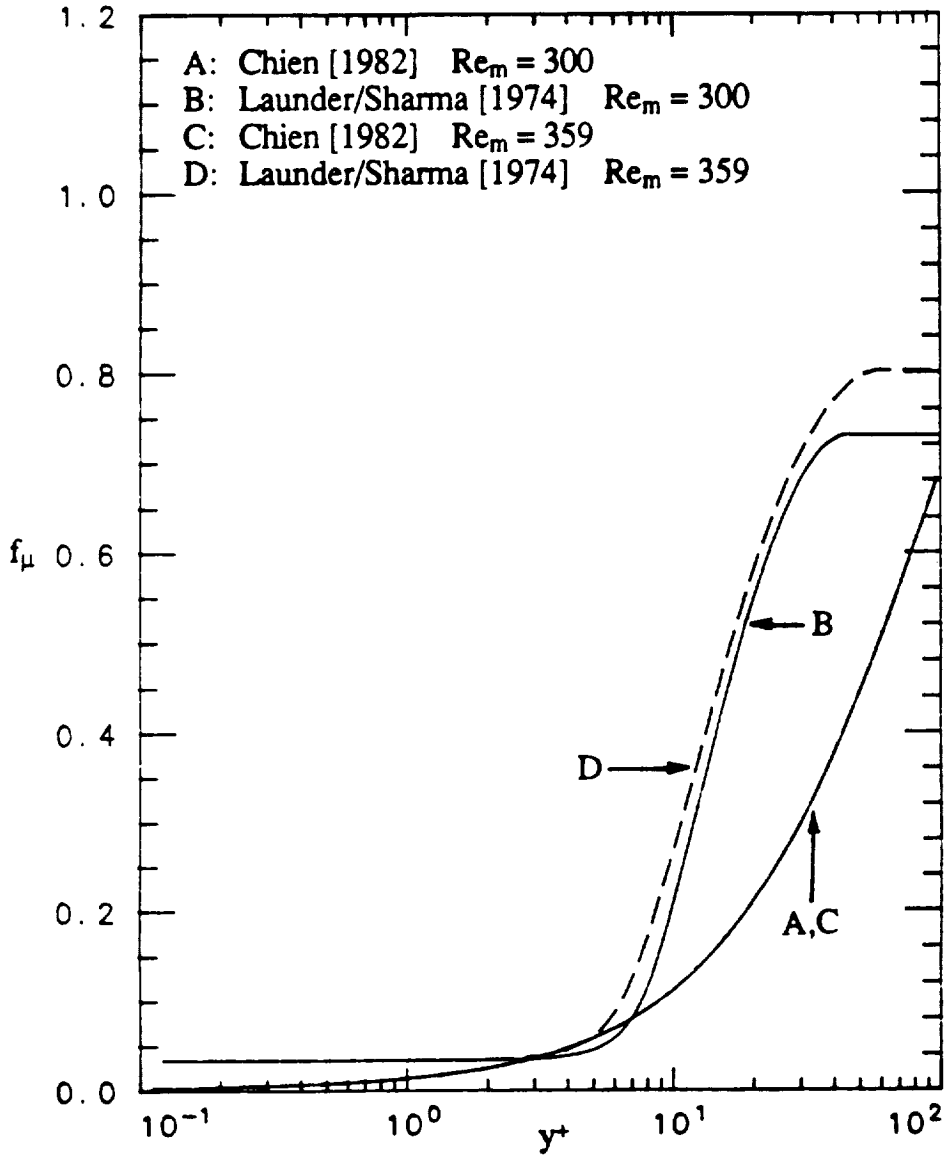

Figure 4.41. Turbulent viscosity damping function profiles at $Re_m = 300$ and 359 for the K. Y. Chien [1982] and the Launder and Sharma [1974] turbulence models.

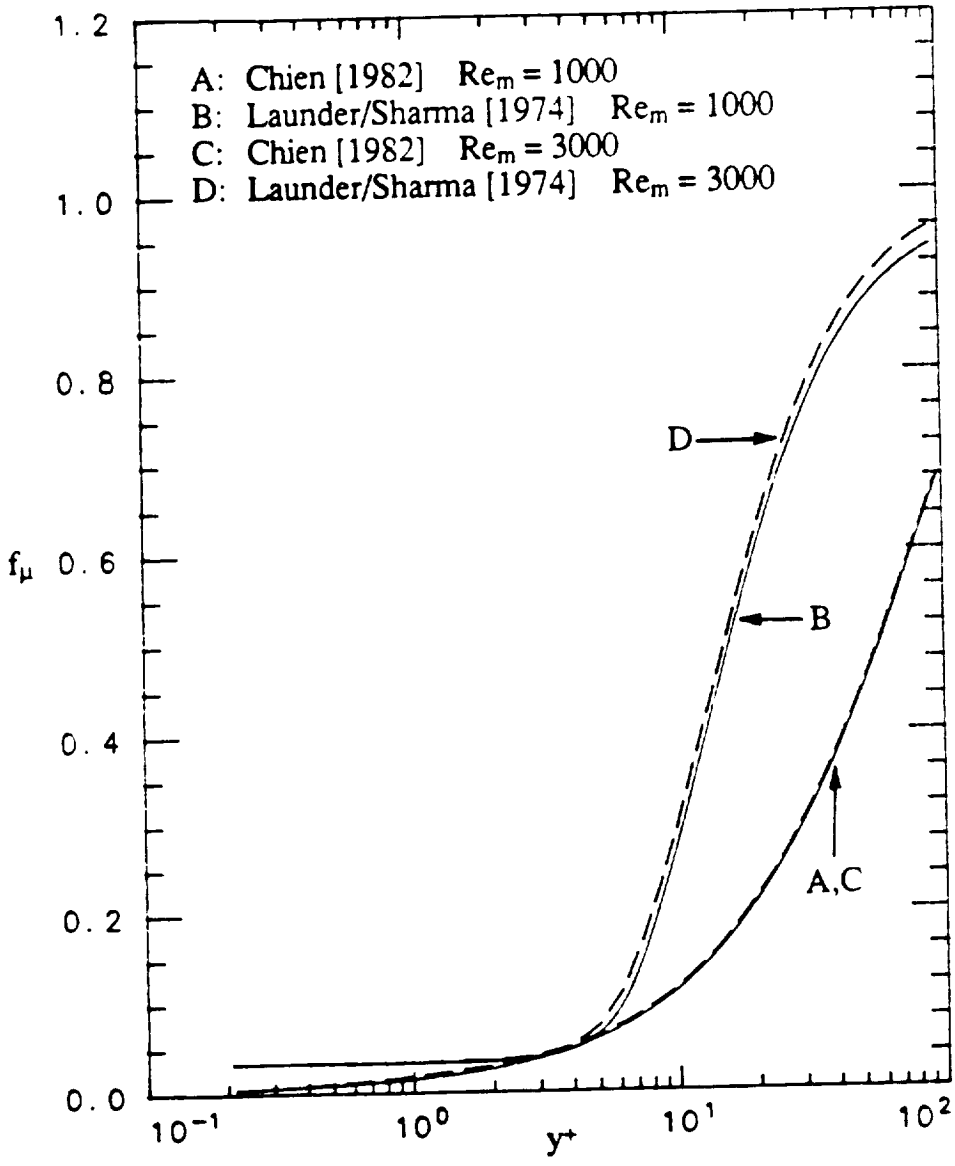

Figure 4.42. Turbulent viscosity damping function profiles at $Re_m = 1000$ and 3000 for the K. Y. Chien [1982] and the Launder and Sharma [1974] turbulence models.

as shown in Figures 4.39 to 4.42. The f_μ function used by K. Y. Chien was undoubtedly formulated for a fully turbulent boundary layer and does not change whether the flow is laminar or in transition. Therefore, in a laminar boundary layer, the K. Y. Chien turbulence model predicts an f_μ distribution throughout the entire layer. On the other hand, the f_μ for the Launder and Sharma model is a function of the turbulent Reynolds number and does reflect whether the flow is laminar, transitional, or fully turbulent depending on the ratio of TKE to TDR. In Figure 4.39, there is an f_μ distribution for the K. Y. Chien model throughout the boundary layer, but for the Launder and Sharma model the f_μ distribution is constant except for at the freestream location. In Figure 4.40, the diffusion of TKE and TDR from the freestream causes the f_μ distribution to change further into the boundary layer. Figure 4.42, when compared to Figure 4.39, shows how much the f_μ distribution has changed for the Launder and Sharma model, reflecting a change in the boundary layer; whereas, the f_μ distribution for the K. Y. Chien model has remained the same.

The "damped" effect in the C_f distribution for the K. Y. Chien model is therefore due to the fact that the f_μ function is set for a fully turbulent boundary layer and, at the start of the calculations, the resulting f_μ distribution within in the laminar boundary layer is not correct. In fact, the f_μ distribution for the K. Y. Chien model is not correct until the boundary layer has progressed to a high Reynolds number where the f_μ distribution only occupies the log and viscous regions of the turbulent boundary layer instead of the entire boundary layer when the flow is laminar.

The problem associated with the f_μ function for transitional flows does not mean the K. Y. Chien two-equation turbulence model should not be used for turbulence modeling. On the contrary, for internal flows at high Reynolds numbers the numerical C_f distribution matches experimental data as shown by Pietrzyk [1985] and Chen [1989]. For external flows, Patel et al. [1985] demonstrated that the K. Y. Chien turbulence model produces reasonable results for fully turbulent flat plate

boundary layer flow. The limitations of the K. Y. Chien model appear to be in the laminar and transition region.

In an attempt to compare Schmidt's transition model and The University of Texas transition model (the original objective of this thesis), the use of two other numerical turbulence models was investigated. The two-equation turbulence models of Lam and Bremhorst [1981] and Launder and Sharma [1974] were examined in this study to attempt to make a comparison of the prediction capabilities of the two proposed transition models. However, in each case numerical instabilities in TEXSTAN associated with each of the turbulence models examined hampered all progress.

In the case of the Lam and Bremhorst turbulence model in TEXSTAN, a fully turbulent boundary layer would revert back to a laminar boundary layer in a zero pressure gradient flow field. The instability by which the turbulent boundary layer reverts back to a laminar boundary layer always begins near the solid wall boundary and propagates out to the freestream. The exact cause of the numerical instability associated with the Lam and Bremhorst turbulence model was not determined, but it is believed to be tied into the asymptotic behavior of the turbulence quantities in the region of the solid wall boundary and how TEXSTAN calculates these values in the wall half control volume of the finite difference equations.

In the case of the Launder and Sharma model in TEXSTAN, for freestream turbulence levels less than 2.0%, the boundary layer would never completely transition into a fully turbulent boundary layer. Instead the boundary layer midway through transition would revert back to a laminar boundary layer. For freestream turbulence levels greater than 2.0%, the C_f distribution would oscillate at high momentum Reynolds numbers associated with a fully turbulent boundary layer. The low freestream turbulence level problem associated with the Launder and Sharma turbulence model was discovered and corrected by Schmidt [1987] in his numerical boundary layer code. However, when the corrections suggested by Schmidt, for

the Launder and Sharma turbulence model, were implemented into TEXSTAN, they had no effect on the transition for low freestream turbulence levels ($Tu_e \leq 1.0\%$).

Chapter 5

Summary and Recommendations

5.0 Summary

The original goal of this research was to compare the transition prediction capabilities of the two transition models, developed at the University of Minnesota and The University of Texas at Austin, coupled with the K. Y. Chien two-equation turbulence model. However, the results of this research has lead to the identification of a major shortcoming in the use of the basic K. Y. Chien turbulence model for low-Reynolds number flows.

Accurate specification of initial dependent variable profiles (such as velocity, stagnation enthalpy, TKE, and TDR) are required in order to obtain satisfactory heat transfer predictions in the stagnation region of a turbine blade. Boundary layer solutions can be desensitized to errors in the initial conditions by starting the boundary layer solution far upstream of the region of interest. However, for turbine blade calculations, the entire airfoil surface makes up the computational domain and requires accurate initial profiles specified at the onset of the calculations. A method for specifying initial TKE and TDR profiles that are compatible with the finite-difference equations defining the K. Y. Chien two-equation turbulence model are detailed in Chapter 3.

Accurate specification of boundary conditions for the computational domain are required in order to obtain accurate results in the governing equations at each integration step. This study detailed a method used to define an accurate and smooth freestream velocity distribution which results in a smooth pressure gradient distribution for the momentum equation. The specification of the freestream turbu-

lence level at a minimum of two locations was required in order to predict an accurate decay of freestream TKE and TDR, which in turn affects the transitional behavior of any two-equation turbulence model. A method for calculating the initial freestream TKE and TDR levels given the freestream turbulence level at one, two, or more locations is detailed in Chapter 3. A problem associated with calculating a decreasing freestream length scale distribution for the K. Y. Chien turbulence model was identified and steps to correct the problem are discussed.

Ultimately, a problem associated with using the K. Y. Chien two-equation turbulence model for transition studies was identified. The problem with the K. Y. Chien two-equation model involved premature start of "natural transition" and a "damped" response as the simulation moved to fully turbulent flow at the end of transition. This is in contrast to other two-equation turbulence models at comparable freestream turbulence conditions. The "damping" of the transition response of the K. Y. Chien turbulence model lead to an inaccurate estimate of the start and end of transition for freestream turbulence levels greater than 1.0%. An inaccurate determination of the start and end of transition leads to difficulty in calculating proper model constants for either of the proposed transition models (equations 2.55 or 2.59). The cause of both problems associated with the K. Y. Chien turbulence model is linked to the form of the f_μ function defined by K. Y. Chien [1982]. Specifying the f_μ function as only a function of y^+ leads to an increased production of TKE in the near-wall region of a laminar boundary layer, which in turn leads to an early start to transition. The resulting f_μ distribution also leads to a "damping" of the fully turbulent response of the K. Y. Chien turbulence model. The form of the f_μ function specified by K. Y. Chien is for a fully turbulent boundary layer. Therefore, in a laminar and transition region of a developing boundary layer, the distribution of f_μ is not correct and will not be correct until the boundary layer becomes fully turbulent with the y^+ effect buried in the sublayer and log regions of the boundary layer.

5.1 Recommendations for Future Work

In this study, it is shown that the K. Y. Chien two-equation turbulence model should not be used for transition studies because of the formation of the f_μ function. As shown by Schmidt [1987], other two-equation turbulence models may be used to obtain accurate transition simulations. For future work in comparing the transition predictions of the two proposed transition models (equations 2.55 and 2.59), it is suggested that a two-equation turbulence model similar to the model proposed by Jones and Launder [1972 and 1973] be used which employes an f_μ function that is not based on y^+.

As for the TEXSTAN boundary layer code, the finite difference equations should be examined to determine if the numerical instabilities associated with the Lam and Bremhorst [1981] and Launder and Sharma [1974] two-equation turbulence models are due to finite difference expressions. Particular emphasis should be placed on the half control volume formulations for both at the wall and freestream locations.

Future work on the study of transition should go beyond the comparison of the two proposed transition models. The ability to numerically predict transition at higher freestream turbulence levels (greater than 10.0%) should be investigated. Included in the study of high freestream turbulence intensities should be an examination of numerically predicting transition under the influence of various pressure gradients. The comparisons of developing dependent variable profiles has been extremely beneficial in this study and would benefit future numerical studies. Future studies should also examine the energy budget for any proposed turbulence model to avoid any numerical irregularities in the boundary layer calculations. For all numerical studies the comparison of numerical simulations to available experimental data is essential in order to draw the correct conclusions from the numerical results.

Appendix A

Derivation of Model Equations for Turbulent Kinetic Energy and Turbulent Dissipation Rate

This appendix is an outline of the derivation for the model form of the turbulent kinetic energy (TKE) and turbulent dissipation rate (TDR) equations, as shown in Chapter 2 as equations (2.19) and (2.20). The equations are derived in tensor notation, then converted to standard Cartesian coordinates.

A.1 Turbulent Kinetic Energy Equation

The standard method to derive the TKE equation is to subtract the mean momentum equation from the instantaneous momentum equation and multiply the results by u_i', then time-average. Using Reynolds decomposition, the instantaneous and mean momentum equations, neglecting body forces, are

$$\partial_k\left(\rho\widetilde{U_k}\widetilde{U_i} \right) = \partial_k\widetilde{\sigma_{ki}} \tag{A.1}$$

and

$$\partial_k\left(\rho U_k U_i \right) = \partial_k\sigma_{ki} - \partial_k\left(\rho\overline{u_k' u_i'} \right) \tag{A.2}$$

where $\widetilde{\sigma_{ki}}$ is the stress tensor for the instantaneous velocity, σ_{ki} is the stress tensor for the mean velocity, and ∂_k is the partial derivative operator, ∂/∂_k. The instantaneous stress tensor is defined as follows

$$\widetilde{\sigma_{ki}} = \sigma_{ki} + \sigma_{ki}' \tag{A.3}$$

where σ_{ki}' is the stress tensor for the fluctuating velocity. The definition of the mean and fluctuating stress tensors are

$$\sigma_{ki} = -P\delta_{ki} + \tau_{ki} \tag{A.4}$$

and

$$\sigma'_{ki} = -P\delta_{ki} + \tau'_{ki} \tag{A.5}$$

where τ_{ki} is the mean shear stress tensor, τ'_{ki} is the fluctuating shear stress tensor, and δ_{ki} is the Kronecker delta. The mean and fluctuating shear stress tensors are defined as follows in terms of the mean and fluctuating velocity gradients

$$\tau_{ki} = 2\mu\left[\frac{1}{2}\left(\frac{\partial U_k}{\partial x_i} + \frac{\partial U_i}{\partial x_k}\right)\right] \tag{A.6}$$

and

$$\tau'_{ki} = 2\mu\left[\frac{1}{2}\left(\frac{\partial u'_k}{\partial x_i} + \frac{\partial u'_i}{\partial x_k}\right)\right]. \tag{A.7}$$

The fluctuating momentum equation is calculated by subtracting the mean momentum equation (A.2) from the instantaneous momentum equation (A.1), which yields

$$\partial_k\left[\,\rho\left(\,U_k u'_i + u'_k U_i + u'_k u'_i\,\right)\right] = \partial_k\left(\,\sigma'_{ki}\,\right) - \partial_k\left(\,-\rho\overline{u'_k u'_i}\,\right). \tag{A.8}$$

Multiplying equation (A.8) by u'_i, time-averaging the resulting equation, and rearranging terms yields the TKE equation

$$\partial_k\left(\,\rho U_k k\,\right) = -\rho\overline{u'_k u'_i}\partial_k(U_i) - \partial_k\left[\,\rho\overline{u'_k k} + \rho\overline{u'_k\left(\frac{P'}{\rho}\right)} - \overline{u'_i\tau'_{ki}}\,\right] - \overline{\tau'_{ki}\partial_k(u'_i)}, \tag{A.9}$$

where k is the turbulent kinetic energy defined as $0.5\overline{u'_i u'_i}$ and repeated indicies imply summation over i (or k) = 1, 2, and 3.

Equation (A.9) is the TKE equation with true dissipation. A majority of the two-equation turbulence models are written in terms of isotropic dissipation. By com-

bining the last two terms on the right-hand side of equation (A.9), the isotropic form of the TKE equation may be written as

$$\underset{\text{I}}{\partial_k(\rho U_k k)} = \underset{\text{II}}{-\rho\overline{u_k' u_i'}\partial_k(U_i)} - \underset{\text{III}}{\partial_k\left[\rho\overline{u_k'}\left(k+\frac{\overline{P'}}{\rho}\right)\right]} - \underset{\text{IV}}{\mu\partial_k k} - \underset{\text{V}}{\hat{\varepsilon}}, \quad \text{(A.10)}$$

where I is the convection of TKE by the mean flow, II is the production of TKE by the mean flow, III is the transport of TKE by turbulence and transport of flow work by turbulence, IV is the transport of work due to viscous stresses, and V is the dissipation of TKE by viscous stresses. In equation (A.10), $\hat{\varepsilon}$ is the isotropic dissipation defined as $\overline{\mu\partial_k u_i'\partial_k u_i'}$.

The transport terms diffuse or redistribute the given quantity within the boundary layer. Invoking the boundary layer assumptions and recognizing the fact that $\overline{u'v'}$ is the dominant Reynolds stress in a two-dimensional boundary layer, equation (A.10) may be written in the following cartesian notation.

$$\underset{\text{I}}{\rho U\frac{\partial k}{\partial x}+\rho V\frac{\partial k}{\partial y}} = \underset{\text{II}}{-\rho\overline{u'v'}\frac{\partial U}{\partial y}} - \underset{\text{III}}{\frac{\partial}{\partial y}\left[\rho\overline{v'}\left(k+\frac{\overline{P'}}{\rho}\right)\right]} - \underset{\text{IV}}{\mu\frac{\partial k}{\partial y}} - \underset{\text{V}}{\hat{\varepsilon}}. \quad \text{(A.11)}$$

Various terms of equation (A.11) must be modeled in order to numerically obtain a solution. The following is a list of the model forms of the different terms of the TKE equation.

Term I: Represents the convection of TKE. No modeling is required for this term; therefore,

$$\text{I} = \rho U\frac{\partial k}{\partial x}+\rho V\frac{\partial k}{\partial y}. \quad \text{(A.12)}$$

Term II: Represents the production of TKE. Using the mean field closure approximation, equation (2.15), this term becomes

$$II = -\rho\overline{u'v'}\frac{\partial U}{\partial y} = \mu_t\left(\frac{\partial U}{\partial y}\right)^2 \qquad (A.13)$$

Term III: Represents the turbulent transport of TKE. Neglecting the fluctuating pressure and using a form of eddy-diffusivity hypothesis (Markatos, 1987) this term becomes

$$III = -\frac{\partial}{\partial y}\left[\rho\overline{u'}\left(k+\frac{\overline{P'}}{\rho}\right)\right] = \frac{\partial}{\partial y}\left(\frac{\mu_t}{\sigma_k}\frac{\partial k}{\partial y}\right). \qquad (A.14)$$

Term IV: Represents the molecular diffusion of TKE. No model is required for this term; therefore,

$$IV = -\frac{\partial}{\partial y}\left[-\mu\frac{\partial k}{\partial y}\right]. \qquad (A.15)$$

Term V: Represents isotropic dissipation. No model is required for this term; therefore,

$$V = -\hat{\varepsilon} = -\mu\overline{\frac{\partial u'}{\partial y}\frac{\partial u'}{\partial y}}. \qquad (A.16)$$

Using the model terms, equations (A.12) to (A.16), the form of the TKE equation used for two-equation turbulence modeling (equation 2.19) may be written as follows

$$\rho U\frac{\partial k}{\partial x}+\rho V\frac{\partial k}{\partial y} = \mu_t\left(\frac{\partial U}{\partial y}\right)^2+\frac{\partial}{\partial y}\left[\left(\mu+\frac{\mu_t}{\sigma_k}\right)\frac{\partial k}{\partial y}\right]-\left(\rho\hat{\varepsilon}+D\right), \qquad (A.17)$$

where D is the low-Reynolds number term used to ensure $\hat{\varepsilon} = 0$ at the wall.

A.2 Turbulent Dissipation Rate Equation

The standard approach to deriving the TDR equation is to differentiate the x_i -component of the fluctuating momentum equation with respect to x_l and multiply the results by $\nu\partial_l u_i'$, then time average [Hanjalic and Launder, 1976]. Using the

chain rule and conservation of mass ($\partial_k U_k = 0$), the fluctuating momentum equation (A.9) is rewritten as

$$\rho U_k \partial_k(u_i') + \rho u_k' \partial_k(U_i) + \rho u_k' \partial_k(u_i') + \partial_k\left(-\rho\overline{u_k' u_i'}\right) = \partial_k(\sigma_{ki}') . \quad \text{(A.18)}$$

Differentiating equation (A.18) by x_l yields

$$\partial_l\left[\rho U_k \partial_k(u_i') + \rho u_k' \partial_k(U_i) + \rho u_k' \partial_k(u_i') + \partial_k\left(-\rho\overline{u_k' u_i'}\right)\right] = \partial_l\partial_k(\sigma_{ki}') . \text{(A.19)}$$

Multiplying equation (A.19) by $\nu\partial_l u_i'$ and time-averaging produces

$$\begin{aligned} 2\nu\Big[\overline{(\partial_l u_i')\partial_l(\rho U_k \partial_k u_i')} + \overline{(\partial_l u_i')\partial_l(\rho u_k' \partial_k U_i)} + \overline{(\partial_l u_i')\partial_l(\rho u_k' \partial_k u_i')}\Big] + \\ 2\nu\Big[\overline{(\partial_l u_i')\partial_l\left(\partial_k\left(\rho\overline{u_k' u_i'}\right)\right)}\Big] = 2\nu\overline{(\partial_l u_i')\partial_l\partial_k(\sigma_{ki}')} . \end{aligned} \quad \text{(A.20)}$$

After expanding each term of equation (A.20), the final form of the TDR equation may be written as

$$\begin{aligned} U_k\partial_k\hat{\varepsilon} = \underset{\text{I}}{} -2\nu\underbrace{\left[\overline{(\partial_l u_i')(\partial_l u_k')} + \overline{(\partial_k u_l')(\partial_i u_l')}\right]}_{\text{II}}(\partial_k U_i) - 2\nu\underbrace{\overline{(\partial_l u_i')(\partial_k u_i')(\partial_l u_k')}}_{\text{III}} \\ - 2\underbrace{\left(\nu\overline{\partial_k\partial_l u_i'}\right)^2}_{\text{IV}} - \partial_k\Big[\underbrace{\overline{u_k'\hat{\varepsilon}}}_{V_A} + 2\underbrace{\frac{\nu}{\rho}\overline{(\partial_l u_k')(\partial_l p')}}_{V_B} - \underbrace{\nu\overline{\partial_k\hat{\varepsilon}}}_{V_C}\Big] - \underbrace{2\nu\overline{u_k'(\partial_l u_i')}(\partial_l\partial_k U_i)}_{\text{VI}} , \end{aligned} \quad \text{(A.21)}$$

where $\hat{\varepsilon}$ is the isotropic dissipation, I is the convection of TDR by the mean flow, II is the production of TDR by the mean flow, III is the production of TDR by vortex stretching, IV is the dissipation of TDR by viscous stresses, V_A is the transport of TDR by velocity fluctuations, V_B is the transport of TDR by pressure fluctuations, V_C is the transport of TDR by dissipation (self transport), and VI is the production of TDR by the mean flow.

Invoking the boundary layer assumptions and using the fact that $\overline{u'v'}$ is the dominate Reynolds stress, each term of equation (A.21) may be modeled as follows using cartesian coordinates [Hanjalic' and Launder, 1972].

Term I: Represents the convection of TDR. No modeling is required for this term; therefore,

$$I = U_k \partial_k \hat{\varepsilon} = U\frac{\partial \hat{\varepsilon}}{\partial x} + V\frac{\partial \hat{\varepsilon}}{\partial y}. \qquad (A.22)$$

Term II: Represents the production of TDR by the mean flow. Using the mean field closure approximation, equation (2.15), this term becomes

$$II = -2\nu\left[\overline{(\partial_l u_i')(\partial_l u_k')} + \overline{(\partial_k u_l')(\partial_i u_l')}\right](\partial_k U_i) = C_1 \frac{\hat{\varepsilon}}{k}\mu_t\left(\frac{\partial U}{\partial y}\right)^2. \qquad (A.23)$$

Terms III + IV: Represents the production of TDR by vortex stretching and the dissipation of TDR by viscous stresses. This term is modeled by Hanjalic and Launder [1972] as

$$III + IV = -2\left[\nu\overline{(\partial_l u_i')(\partial_k u_i')(\partial_l u_k')} + (\nu\partial_k\partial_l u_i')\right] = -C_2\frac{\hat{\varepsilon}^2}{k}. \qquad (A.24)$$

Term V_A: Represents the turbulent diffusion of TDR by velocity fluctuations. Using a form of eddy-diffusivity hypothesis (Hanjalic and Launder, 1972) this term becomes

$$V_A = -\partial_k\left(\overline{u_k'\hat{\varepsilon}}\right) = \frac{\partial}{\partial y}\left(\frac{\nu_t}{\sigma_\varepsilon}\frac{\partial \hat{\varepsilon}}{\partial y}\right). \qquad (A.25)$$

Term V_B: Represents the transport of TDR by pressure fluctuations. This term is neglected; therefore,

$$V_B = -2\frac{\nu}{\rho}\overline{\partial_l u_k'\partial_l P'} = 0. \qquad (A.26)$$

Term V_C: Represents the transport of TDR by dissipation (self transport). No modeling is required for this term; therefore,

$$V_C = \nu\overline{\partial_k\hat{\varepsilon}} = \nu\frac{\partial \hat{\varepsilon}}{\partial y}. \qquad (A.27)$$

Term VI: Represents production of TDR by the mean flow. This term is neglected because higher order derivatives of the mean flow are assumed negligible (Hanjalic and Launder, 1972)

$$VI = 2\nu\overline{u_k'(\partial_l u_i')}(\partial_l\partial_k U_i) = 0. \qquad (A.28)$$

Jones and Launder [1972] proposed the use of damping functions to modify the C-constants in the TDR equation so that numerical calculations may be made within the buffer and viscous layers close to the wall. Using the model terms, equations (A.22) and (A.28), with the addition of damping functions, the form of the TDR equation used for two-equation turbulence modeling (equation 2.20) may be written as follows

$$\rho U\frac{\partial\hat{\varepsilon}}{\partial x}+\rho V\frac{\partial\hat{\varepsilon}}{\partial y} = C_1 f_1\frac{\hat{\varepsilon}}{k}\mu_t\left(\frac{\partial U}{\partial y}\right)^2+\frac{\partial}{\partial y}\left[\left(\mu+\frac{\mu_t}{\sigma_\varepsilon}\frac{\partial\hat{\varepsilon}}{\partial y}\right)\right]-\left(\rho C_2 f_2\frac{\hat{\varepsilon}^2}{k}+E\right), \qquad (A.29)$$

where E is the low-Reynolds number term used to improve the match of the peak level of TKE with experiment [Jones and Launder, 1972].

Appendix B

Derivation of the Reshotko Equation Describing an Initial Turbulent Kinetic Energy Profile

This appendix outlines the method used to derive the initial TKE profile, equation (3.26), to simulate the effect freestream turbulence intensity has on the otherwise Blasius type of profile. To develop the TKE profile equation, assume the velocity fluctuations in the streamwise direction are the only fluctuations considered, therefore,

$$k = 0.5\,\overline{u'^2}\,. \tag{B.1}$$

The fluctuating streamwise velocity may be approximated as follows,

$$\overline{u'} = \frac{dU}{dU_e}\,. \tag{B.2}$$

Using the Blasius variables, equation (B.2) may be written as,

$$\frac{dU}{dU_e} = \frac{d}{dU_e}\left[U_e f'\right]. \tag{B.3}$$

Conducting the indicated differentiation in equation (B.3) yields

$$\overline{u'} = f' + 0.5\,\eta\, f''\,. \tag{B.4}$$

Equation (B.4) defines the fluctuating streamwise velocity component in terms of the Blasius variables. Examining Equation (B.1) the TKE profile may be defined as,

164

$$k \approx C_1 \overline{u'^2}. \tag{B.5}$$

Using equation (B.4) and defining the proportionality constant ,C_1, as the freestream TKE value, the Reshotko TKE profile equation is defined as follows

$$k = C_1 \left[f' + 0.5 \eta f'' \right]^2 \tag{B.6}$$

where,

$$C_1 = 1.5 (Tu\ U_e)^2 = k_e . \tag{B.7}$$

The constant of proportionality is defined as k_e in order for the TKE profile to asymptotically match the freestream TKE boundary condition.

Appendix C

Use of Splines to Obtain Smooth Freestream Velocity Data

As discussed in Chapter 3, TEXSTAN cannot use raw experimental freestream velocity data as boundary conditions because small experimental errors result in large errors in the numerical calculation of gradients. The purpose of this Appendix is to graphically demonstrate the effect the number of knots used in a least-squares cubic spline routine has on the calculated freestream velocity distribution and resulting pressure gradient calculation.

TEXSTAN requires a continuous representation of the freestream velocity distribution in order to calculate the pressure gradient at each integration step for the momentum equation. TEXIPBC uses a least-squares cubic spline to calculate a continuous freestream velocity distribution given a discrete set of input freestream velocity data values. There is one advantage to using a least-squares cubic spline over a general cubic spline. Besides giving the user a continuous representation of the input data, a least-squares cubic spline allows the user the option of smoothing any irregularities in the data through the selection of a number of knots.

To examine the effect the number of knots have on the calculation of the freestream pressure gradient, TEXIPBC was used to determine the freestream pressure distribution, freestream velocity distribution, and freestream pressure gradient distribution as a function of the number of knots used. Appendix D contains the relevant flow parameters used for calculating the freestream conditions. The freestream pressure distribution, i.e. input loading, used to calculate the freestream velocity and pressure gradient distributions was obtained from Daniels and Browne [1981] and corresponds to the turbine blade suction at the design conditions. In the analysis of turbine blade loading distributions the loading is often related to a loca-

tion on the blade through the use of the surface distance, s. The surface distance, s, is the distance measured along the surface of a blade from the stagnation point, where s = 0, to the trailing edge location. Since the curvature of the pressure and suction surfaces of a turbine blade are different, they will have different surface distances.

In the following discussion of the figures, the role the number of knots used by the least-squares cubic is considered. For zero knots, the least-squares cubic spline does not smooth the input data; therefore, the resulting output freestream distributions will contain random oscillations. For a large number of knots (approximately greater than 15) the resulting input data will not be smoothed because the advantage of a least-squares fit to the data between the knots vanishes. As a result, the output freestream distributions will look very similar to the case with zero knots. For a small number of knots (approximately less than 12) the input data will be smoothed which translates into smooth output distributions. In summary, the degree of smoothing for output freestream distributions is subject to the user's judgment and the number of knots used. The question of what aspects of the input loading data should or not be smoothed must be considered by the user.

Figure C.1 is a plot of the freestream pressure distribution as a function of s for a various numbers of knots. Zero knots corresponds to the original input freestream pressure distribution, ten and five knots correspond to different degrees of smoothing used by the least-squares cubic spline. As expected, the smoothest output pressure distribution is for the five knot case.

Figure C.2 is a plot of the freestream velocity distribution as a function of s for a various numbers of knots. The freestream velocity distribution is calculated by TEXIPBC using the input freestream pressure distribution and one-dimensional compressible flow equations. In this figure the freestream pressure distribution is

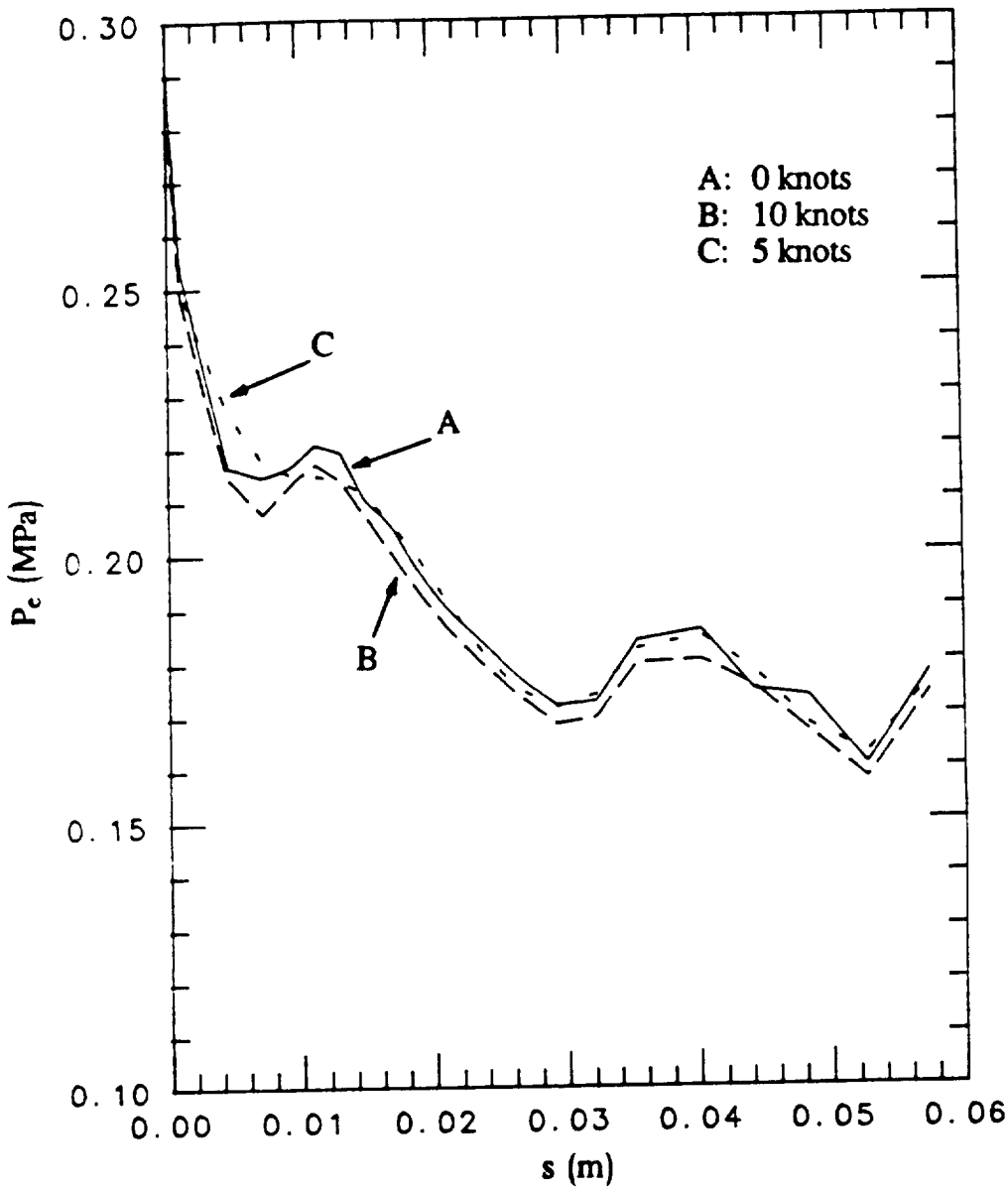

Figure C.1. Freestream pressure distribution for the suction surface of Daniels' [1978] turbine blade for the design Reynolds number case.

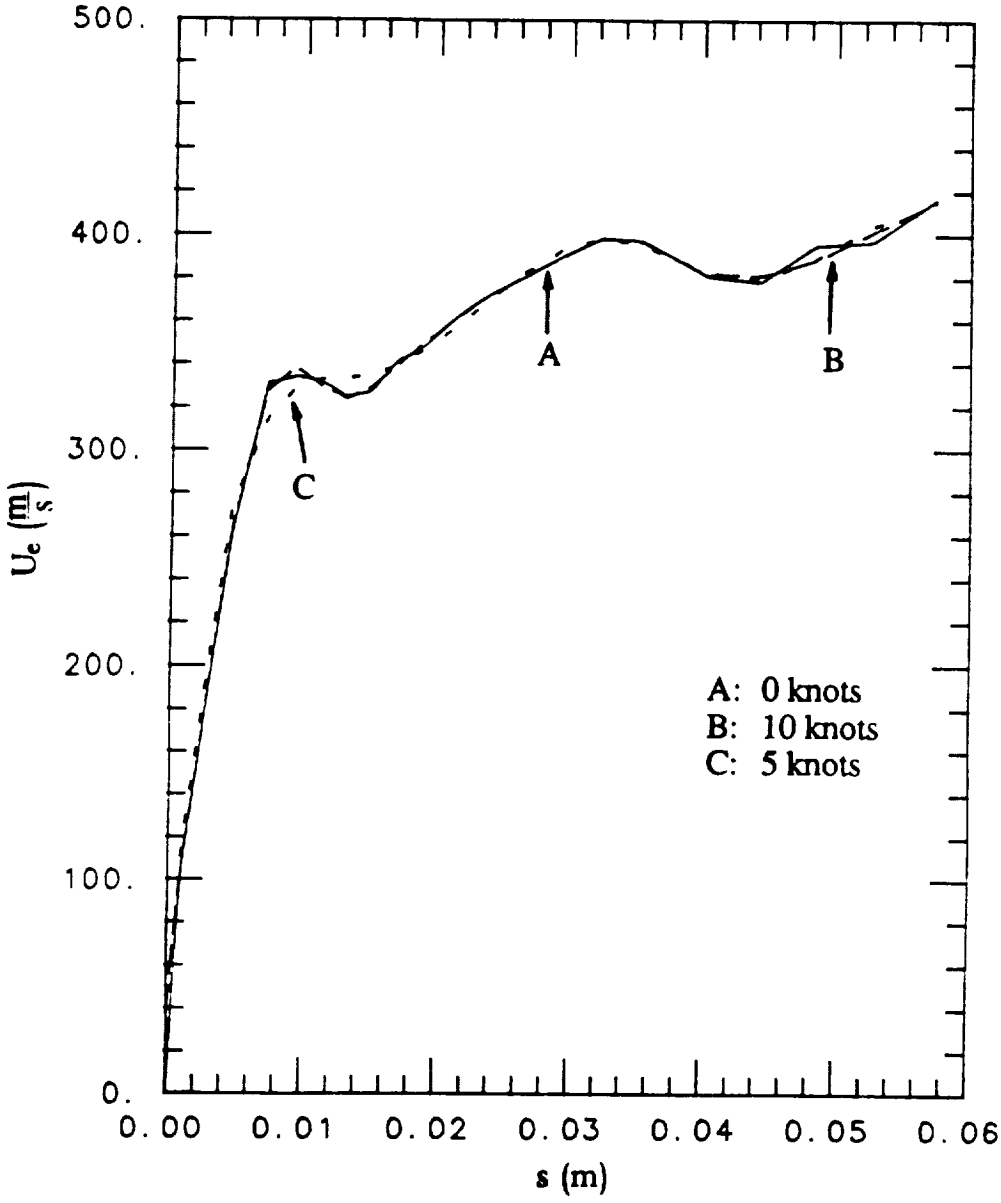

Figure C.2. Freestream velocity distribution for the suction surface of Daniels' [1978] turbine blade for the design Reynolds number case.

relatively smooth for the zero knot case, but by using five knots, the "bulge" at s = 0.01 m can be eliminated.

Figure C.3 is a plot of the freestream pressure gradient distribution as a function of s for a various number of knots. The pressure gradient is calculated from equation (3.4). What is immediately noticed in Figure C.3 is large oscillations in the pressure gradient calculations for the cases of zero and ten knots. These oscillations only emphasize the point that a smooth velocity distribution, like Figure C.2, does not guarantee a smooth pressure gradient distribution. The numerical calculation of the velocity gradient used in equation (3.4) amplifies any errors in the velocity distribution which results in the the large oscillations shown in Figure C.3. The five knot case smooths out a majority of the oscillations in the pressure gradient. Therefore, the freestream velocity distribution calculated from the five knot case could be used by TEXSTAN to simulate the freestream velocity boundary conditions for the suction surface of the turbine blade.

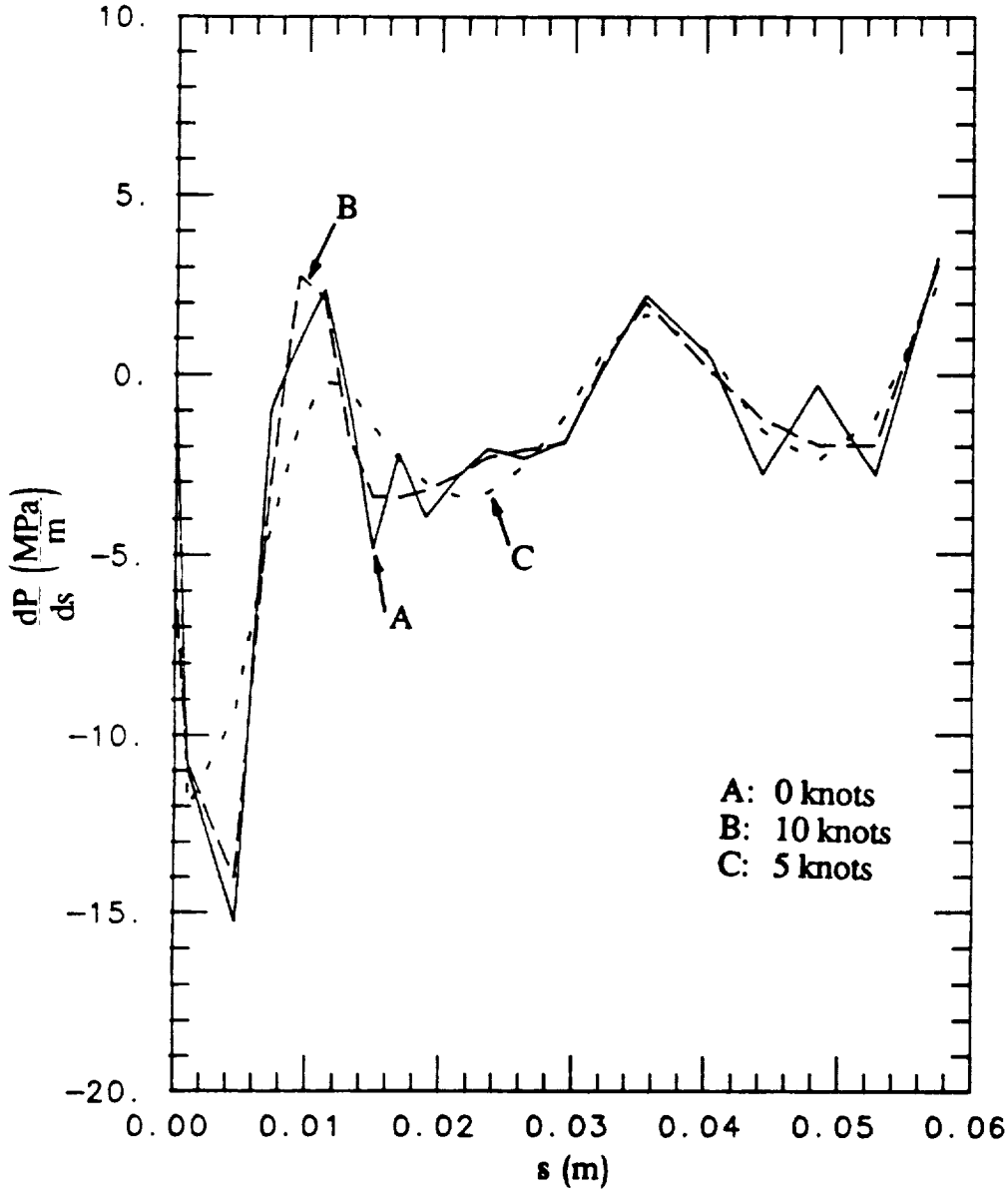

Figure C.3. Freestream pressure gradient distribution for the suction surface of Daniels' [1978] turbine blade for the design Reynolds number case.

Appendix D

Details of Numerical Simulations

This appendix outlines the various flow field characteristics used for the numerical transition simulations. The experimental heat transfer data of Blair and Werle [1980] for flat plate zero pressure gradient flow is presented as well as the turbine blade velocity loading for Daniels [1978] used in Appendix C.

For all of the numerical simulations discussed in this section, the working fluid was air, the fluid properties were considered constant, and the turbulent Prandtl number was assumed constant and equal to 0.9. Boundary layer entrainment was based only on the velocity profile and viscous dissipation was included.

Section 4.1.1 numerical simulation parameters (zero pressure gradient):

U_e = 30.3 m/s T_w = T_e = 294.7 K

P_e = 1 atm T_e^* = 295 K

Tu_e = 3.0% $k_{e,i}$ = 1.239 m^2/s^2

a_1 = 1.0 $\hat{\varepsilon}_{e,i}$ = 0.01 m^2/s^3

integration step size = 0.25δ

Starting locations:

for $Re_{x,i}$ = 10,000 → x_i = $5.0294*10^{-3}$ m

for $Re_{x,i}$ = 1000 → x_i = $5.0294*10^{-4}$ m

for $Re_{x,i}$ = 100 → x_i = $5.0294*10^{-5}$ m

for $Re_{x,i}$ = 10 → x_i = $5.0294*10^{-6}$ m

for $Re_{x,i}$ = 1 → x_i = $5.0294*10^{-7}$ m

Section 4.1.2 numerical simulation parameters (zero pressure gradient):

U_e = 30.3 m/s $T_w = T_e$ = 294.7 K

P_e = 1 atm T_e^* = 295 K

Tu_e = 3.0% $k_{e,i}$ = 1.239 m^2/s^2

$Re_{x,i}$ = 10 $\hat{\varepsilon}_{e,i}$ = 0.01 m^2/s^3

integration step size = 0.25δ

Initial turbulent dissipation rate profiles:

a_1 = 100, 10, 1, 0.1, and 0.01

Section 4.1.3 numerical simulation parameters (zero pressure gradient):

U_e = 30.3 m/s $T_w = T_e$ = 294.7 K

P_e = 1 atm T_e^* = 295 K

a_1 = 1.0 $\hat{\varepsilon}_{e,i}$ = 0.01 m^2/s^3

integration step size = 0.25δ

Starting locations:

for Tu_e = 0.5%: $k_{e,i}$ = 0.034 m^2/s^2 and $Re_{x,i}$ = 40,000
for Tu_e = 1.0%: $k_{e,i}$ = 0.138 m^2/s^2 and $Re_{x,i}$ = 100
for Tu_e = 2.0%: $k_{e,i}$ = 0.551 m^2/s^2 and $Re_{x,i}$ = 25
for Tu_e = 4.0%: $k_{e,i}$ = 2.203 m^2/s^2 and $Re_{x,i}$ = 6
for Tu_e = 6.0%: $k_{e,i}$ = 4.958 m^2/s^2 and $Re_{x,i}$ = 2
for Tu_e = 8.0%: $k_{e,i}$ = 8.814 m^2/s^2 and $Re_{x,i}$ = 1

Section 4.2.3 numerical simulation parameters for the Blair and Werle [1980] zero pressure gradient cases:

U_e = 30.3 m/s T_e^* = 295 K

P_e = 1 atm a_1 = 1.0

q_w = 0.0 W/m^2 0.0 < x ≤ 0.0429 m

q_w = 850 W/m^2 0.0429 < x ≤ 2.4 m

T_w/T_e = 1.03 (approximately) for x > 0.0429 m

integration step size = 0.25δ

Blair Grid 1:	at $x = 3.114*10^{-5}$ m:	Tu_e	= 1.27%
		$k_{e,i}$	= 0.222 m^2/s^2
		$\hat{\varepsilon}_{e,i}$	= 4.0 m^2/s^3
Blair Grid 2:	at $x = 7.546*10^{-6}$ m:	Tu_e	= 2.58%
		$k_{e,i}$	= 0.917 m^2/s^2
		$\hat{\varepsilon}_{e,i}$	= 25.0 m^2/s^3
Blair Grid 3:	at $x = 1.004*10^{-6}$ m:	Tu_e	= 6.17%
		$k_{e,i}$	= 5.243 m^2/s^2
		$\hat{\varepsilon}_{e,i}$	= 200.0 m^2/s^3

Table D.1 contains the experimental flat plate zero pressure gradient heat transfer distribution for Blair and Werle [1980]. This data is used in Figures 4.11 to 4.13.

Table D.1. Experimental Heat Transfer Data of Blair and Werle [1980] for Flat Plate Zero Pressure Gradient Flow

x-Reynolds Number	Stanton Number Grid 1	Stanton Number Grid 2	Stanton Number Grid 3
1.10603E+05	0.002916	0.002962	0.004105
1.35854E+05	0.002234	0.002321	0.003316
1.61106E+05	0.001954	0.002060	0.003251
1.86358E+05	0.001688	0.001811	0.003155
2.11609E+05	0.001574	0.001650	0.003207
2.36861E+05	0.001465	0.001596	0.003130
2.62113E+05	0.001356	0.001533	0.003054
2.87364E+05	0.001261	0.001583	0.003007
3.12616E+05	0.001221	0.001583	0.003007
3.37868E+05	0.001166	0.001723	0.002984
3.63120E+05	0.001124	0.001803	0.002917
4.13623E+05	0.001103	0.002096	0.002790
4.64126E+05	0.001055	0.002349	0.002848
5.14630E+05	0.001097	0.002501	0.002790
5.65133E+05	0.001129		0.002751
6.66140E+05	0.001377	0.002444	0.002549
7.67147E+05	0.001734	0.002415	0.002544
8.68154E+05	0.001982	0.002321	0.002484
9.69161E+05	0.002159	0.002241	0.002390
1.07017E+06	0.002234	0.002240	0.002391
1.17117E+06	0.002192	0.002207	0.002350
1.27218E+06	0.002089	0.002136	0.002278
1.37319E+06	0.002056	0.002040	0.002216
1.47420E+06	0.002016	0.002051	0.002177
1.57520E+06	0.001989	0.002001	0.002183
1.67621E+06	0.001962	0.001967	0.002092
1.77722E+06	0.001936	0.001955	0.002074
1.87822E+06	0.001923	0.001921	0.002052
1.97923E+06	0.001962	0.001967	0.002134
2.08024E+06	0.001883	0.001905	0.002045
2.18124E+06	0.001873	0.001873	0.002038
2.33275E+06	0.001860	0.001865	0.001989
2.48426E+06	0.001832	0.001814	0.001936
2.63577E+06	0.001822	0.001813	0.001953
2.78728E+06	0.001776	0.001770	0.001930
2.93879E+06	0.001781	0.001761	0.001918
3.09030E+06	0.001760	0.001739	0.001910
3.24181E+06	0.001749	0.001741	0.001885
3.39332E+06	0.001719	0.001713	0.001868
3.54484E+06	0.001694	0.001711	0.001849
3.69635E+06	0.001719	0.001723	0.001868
3.84786E+06	0.001723	0.001718	0.001874
3.99937E+06	0.001703	0.001713	0.001874
4.15088E+06	0.001706	0.001723	0.001881
4.30239E+06	0.001693	0.001698	0.001850
4.45390E+06	0.001703	0.001705	0.001827
4.60541E+06	0.001645	0.001674	0.001793
4.75692E+06	0.001665	0.001650	0.001791

Section 4.3 numerical simulation parameters (zero pressure gradient):

U_e = 30.3 m/s $T_w = T_e$ = 294.7 K

P_e = 1 atm T_e^* = 295 K

a_1 = 1.0 $\hat{\varepsilon}_{e,i}$ = 0.01 m^2/s^3

integration step size = 0.25δ

Starting locations:

for Tu_e = 2.0%: $k_{e,i}$ = 0.551 m^2/s^2 and $Re_{x,i}$ = 25

Appendix C numerical simulations for Daniels [1978] Turbine Blade:

M_f = 0.35 T_f^* = 432 K

P_f^* = 0.292 MPa T_f = 423 K

T_W = 289 K

integration step size = 0.25δ

Table D.2 contains the x and y coordinates and experimental freestream pressure distribution for the suction surface of Daniels [1978] turbine blade (design Reynolds number case). The x and y coordinates are used to determine the turbine blade geometry and resulting wetted surface distance, called s, while the freestream pressure distribution is used to calculate the freestream velocity boundary conditions.

Table D.2. Experimental x and y Coordinates and Freestream Pressure Distribution for the Suction Surface of Daniels' [1978] Turbine Blade

X (m)	Y (m)	Freestream Pressure (Pa)
0.00070	0.032640	2.92000e+5
0.00021	0.033561	2.78250e+5
0.00163	0.036909	2.18360e+5
0.00347	0.038693	1.82290e+5
0.00531	0.039692	1.80570e+5
0.00714	0.040228	1.82010e+5
0.00898	0.040383	1.85700e+5
0.01082	0.040187	1.84550e+5
0.01265	0.039667	1.76740e+5
0.01449	0.038807	1.72950e+5
0.01633	0.037538	1.65500e+5
0.01816	0.035857	1.59340e+5
0.02000	0.033829	1.54580e+5
0.02184	0.031472	1.48680e+5
0.02301	0.028736	1.44030e+5
0.02367	0.025685	1.44660e+5
0.02735	0.022444	1.53860e+5
0.02919	0.018998	1.55520e+5
0.03102	0.015314	1.45880e+5
0.03286	0.011348	1.44790e+5
0.03470	0.007042	1.33720e+5
0.03653	0.002307	1.47770e+5

Bibliography

Abu-Ghannam, B. J., and Shaw, R., 1980, "Natural Transition of Boundary Layers - The Effects of Turbulence, Pressure Gradient, and Flow History", Journal of Mechanical Engineering Science, Vol. 22, No. 5, pp. 213 - 228.

Arad, E., Berger, M., Israeli, M., and Wolfshtien, M., 1982, "Numerical Calculation of Transitional Boundary Layers", International Journal for Numerical Methods in Fluids, Vol. 2, pp. 1 - 23.

Benton, D. N., 1985, TEXSTAN Document Written for Dr. M. E. Crawford, Department of Mechanical Engineering, The University of Texas - Austin.

Blair, M. F., 1983a, "Influence of Free-Stream Turbulence on Turbulent Boundary Layer Heat Transfer and Mean Profile Development, Part I - Experimental Data", Journal of Heat Transfer, Vol. 105, pp. 33 - 40.

Blair, M. F., 1983b, "Influence of Free-Stream Turbulence on Turbulent Boundary Layer Heat Transfer and Mean Profile Development, Part II - Analysis of Results", Journal of Heat Transfer, Vol. 105, pp. 41 - 47.

Blair, M. F., and Werle, M. J., September 1980, "The Influence of Free-Stream Turbulence on The Zero Pressure Gradient Fully Turbulent Boundary Layer", United Technologies Research Center Report R80-914388-12.

Blair, M. F., and Werle, M. J., March 1981, "Combined Influence of Free-Stream Turbulence and Favorable Pressure Gradients on Boundary Transition and Heat Transfer", United Technologies Research Center Report R81-914388-17.

Boussinesq, J., 1877, "Mem. Pres. Acad. Sci.", Paris, Vol. 23, pp. 46.

Bradshaw, P., Ferriss, D. H., and Atwell, N. P., 1967, "Calculation of Boundary - Layer Development Using the Turbulent Energy Equation", Journal of Fluid Mechanics, Vol. 28, pp. 593

Carnahan, B., Luther, H. A., and Wilkes, J. O., 1969, Applied Numerical Methods, Wiley and Sons, New York.

Chen, T. H., 1989, An Investigation of the Low-Reynolds Form of the Two-Equation Turbulence Models for Pipe Flows and Channel Flows, MS Thesis, The University of Texas at Austin.

Chien, K. Y., January 1982, "Prediction Of Channel And Boundary-Layer Flows With A Low-Reynolds-Number Turbulence Model", AIAA Journal, Vol. 20, No. 1, pp. 33 - 38.

Comte-Bellot, G., and Corrsin, S., 1966, "The Use of a Contraction to Improve the Isotropy of Grid Generated Turbulence", Journal of Fluid Mechanics, Vol. 25, No. 4, pp. 657 - 682.

Crawford, M. E., and Kays, W. M., 1976, "STAN5 - A Program For Numerical Computation Of Two-dimensional Internal And External Boundary Layer Flows", NASA CR-2742.

Daniels, L. C., 1978, Film-cooling of Gas Turbine Blades, Ph.D. Thesis, Department of Engineering Science, University of Oxford, England.

Daniels, L. D., and Browne, W. B., 1981, "Calculation of Heat Transfer Rates to Gas Turbine Blades", International Journal of Heat and Mass Transfer, Vol. 24, No. 5, pp. 871 - 879.

Dhawan, S., and Narasimha, R., 1958, "Some Properties of Boundary Layer Flow During the Transition from Laminar to Turbulent Motion", Journal of Fluid Mechanics, Vol. 3, pp. 418 - 436.

Dutoya, D., and Michard, P., 1981, "A Program for Calculating Boundary Layers and Heat Transfer along Compressor and Turbine Blades", Numerical Methods in Heat Transfer, Wiley and Sons, New York.

Dyban, YE. P., Epik, E. YA., and Suprun, T. T., July - August 1976, "Characteristics of the Laminar Boundary Layer in the Presence of Elevated Free-stream Turbulence", Fluid Mechanics - Soviet Research, Vol. 5, No. 4, pp. 30 - 36.

Dyban, YE. P., and Epik, E. YA., August 7-11, 1978, "Heat Transfer in a Boundary Layer in Turbulized Air Flow", 6th International Heat Transfer Conference, Toronto, Canada, Hemisphere Publishing Corporation, Vol. 2, pp. 507 - 512.

Emmons, H. W., July 1951, "The Laminar - Turbulent Transition in a Boundary Layer - Part I", Journal of Aerospace Sciences, Vol. 18, No. 7, pp. 490 - 498.

Forest, A. E., October 1977, "Engineering Predictions of Transitional Boundary Layers", AGARD Conference Proceedings, No. 224, pp. 22-1 to 22-19.

Gaugler, R. E., 1985, "A Review and Analysis of Boundary Layer Transition Data for Turbine Application", ASME Paper 85-GT-83.

Graham, R. W., 1979, "Fundamental Mechanisms that Influence the Estimate of Heat Transfer to Gas Turbine Blades", ASME Paper 79-HT-43.

Hancock, P. E., Bradshaw, P., September 1983, "Effect of Free-stream Turbulence on Turbulent Boundary Layers", Journal of Fluids Engineering, Vol. 105, pp. 284 - 289.

Hanjalic, K. and Launder, B. E., 1972, "A Reynolds Stress Model of Turbulence and Its Application to Thin Shear Flows", Journal of Fluid Mechanics, Vol. 52, No. 4, pp.609 - 638.

Hanjalic, K. and Launder, B. E., 1976, "Contribution Towards a Reynolds-Stress Closure for Low-Reynolds-Number Turbulence", Journal of Fluid Mechanics, Vol. 74, No. 4, pp.593 - 610.

Hassid, S., and Poreh, M., June 1975, "A Turbulent Energy Model for Flows with Drag Reduction", Journal of Fluids Engineering, Vol. 97, pp. 234 - 241.

Hinze, J. O., 1975, Turbulence, second edition, McGraw-Hill Book Company, New York.

Hirata, M., Tanaka, H., Kawamura, H., and Kasagi, N., 1982, "Heat Transfer in Turbulent Flows", Proceedings of the 1982 Heat Transfer Conference, San Francisco, California.

Hylton, L. D., Mihelc, M. S., Turner, E. R., Nealy, D. A., York, R. E., May 1983, "Analytical and Experimental Evaluation of the Heat Transfer Distribution Over the Surface of Turbine Vanes", NASA CR - 168015.

IMSL, 1984, IMSL Library User's Manual, International Mathematical and Statistical Libraries, Inc.

Johnson, K. D., 1987, Heat Transfer Calculations on Turbine Airfoils, MS Thesis, The University of Texas at Austin.

Jones, W. P., and Launder, B. E., February 1972, "The Prediction Of Laminarization With A Two-Equation Model Of Turbulence", International Journal of Heat and Mass Transfer, Vol. 15, No. 2, pp. 301 - 313.

Jones, W. P., and Launder, B. E., 1973, "The Calculation of Low-Reynolds-Number Phenomena with a Two-Equation Model of Turbulence", Journal of Heat and Mass Transfer, Vol. 16, pp. 1119 - 1130.

Kays, W. M., and Crawford, M. E., 1980, Convection Heat And Mass Transfer, second edition, McGraw Hill Book Company, New York.

Lakshminarayana, B., December 1986, "Turbulence Modeling for Complex Shear Flows", AIAA Journal, Vol. 24, No. 12, pp. 1900 - 1917.

Lam, C. K. G., and Bremhorst, K., September 1981, "A Modified Form of the k-ε Model for Predicting Wall Turbulence", Journal of Fluids Engineering, Vol. 103, pp. 456 - 460.

Launder, B. E., 1984, "Second-Moment Closure: Methodology and Practice", pp. 1 - 147, in Turbulence Models and Their Applications, Vol. 2, Editions Eyrolles, Paris.

Launder, B. E., and Sharma, B. I., 1974, "Application fo the Energy - Dissipation Model of Turbulence to the Calculation of Flow Near a Spinning Disc", Letters in Heat and Mass Transfer, Vol. 1, pp. 131 - 138.

Launder, B. E., and Spalding, D. B., 1974, "The Numerical Computation of Turbulent Flows", Computer Methods in Applied Mechanics and Engineering, Vol. 3, No. 2, pp. 269 - 289.

Markatos, N. C., 1987, "Computer Simulation Techniques for Turbulent Flows", Chapter 31, pp. 1221 - 1275, in Encyclopedia of Fluid Mechanics: Complex Flow Phenomena and Modeling, Vol. 6, N. P. Cheremisinoff (Ed.), Gulf Publishing Company, Houston.

McDonald, H., and Fish, R. W., 1973, "Practical Calculations of Transitional Boundary Layers", International Journal of Heat and Mass Transfer, Vol. 16, pp. 1729 - 1744.

Motulevich, V. P., Sergiyevskiy, E. D., Zhubrin, S. V., and Lukosiavicius, L. K.-J., July - August 1984, "Analysis of Skin Friction and Heat Transfer in the Boundary Layer of a Turbulent Flow", Heat Transfer - Soviet Research, Vol. 16, No. 4, pp. 99 - 105.

Nagano, Y., and Hishida, M., June 1987, "Improved form of the k-ε Model for Wall Turbulent Shear Flows", Journal of Fluids Engineering, Vol. 109, pp. 156 - 160.

Ng, K. H., November 1971, Prediction of Turbulent Boundary-Layer Development Using a Two Equation Model of Turbulence, Ph. D. Thesis, University of London, England.

Park, W., and Simon, T., March 1987, "Prediction of Convex - Curved Transitional Boundary Layer Heat Transfer Behavior Using MLH Models", Presented at the 2nd ASME/JSME Thermal Engineering Conference.

Patankar, S. V., and Spalding, D. B., 1970, Heat And Mass Transfer In Boundary Layers - A General Calculation Procedure, Intertext Books, London.

Patankar, S. V., 1980, Numerical Heat Transfer And Fluid Flow, Hemisphere Publishing Corporation, New York.

Patel, V. C., Rodi, W., and Scheuerer, G., September 1985, "Turbulence Models For Near-Wall And Low Reynolds Number Flows: A Review", AIAA Journal, Vol. 23, No. 9, pp. 1308 - 1319.

Pietrzyk, J. R., 1985, TEXSTAN Document Written for Dr. M. E. Crawford, Department of Mechanical Engineering, The University of Texas - Austin.

Pietrzyk, J. R., 1985, Numerical Investigation of Buoyancy-Affected Channel Flows, MS Thesis, The University of Texas at Austin.

Prandtl, L., 1925, "Bericht uber Untersuchungenzur ausgebildete Turbelenz", Z. Angew. Math. Mech., Vol. 5, pp. 136-139.

Priddin, C. H., 1975, The Behavior of Turbulent Boundary Layer on Curved Porous Walls", Ph.D. Thesis, Imperial College, London.

Reshotko, E., 1988, private conversation with Crawford, M., The University of Texas at Austin.

Reynolds, W. C., 1976, "Computation of Turbulent Flows", Annual Review of Fluid Mechanics, Vol. 8, pp. 183 - 208.

Riley, J. J., and Gad-el-Hak, M., 1985, "The Dynamics of Turbulent Spots", pp. 123 - 155, in Frontiers in Fluid Mechanics, S. H. Davies, and J. L. Lumley (Ed.), Springer-Verlag, Berlin.

Roberts,G., and Brown, A., 1984, "Boundary-Layer Transition Regions on Turbine Blade Suction Surfaces", ASME Paper 84-GT-284.

Rodi, W., 1976, "A New Algebraic Relation for Calculating Reynolds Stresses", Zeitschrift fuer Angewandte Mathematik und Mechanik, Vol. 56, pp. 219.

Rodi, W., 1980, Turbulence Models and Their Application in Hydraulics, Book Publication of the International Association for Hydraulic Research, Delft, the Netherlands.

Rodi, W., 1982, "Examples Of Turbulence Models For Incompressible Flows", AIAA Journal, Vol. 20, No. 7, pp. 872 - 879.

Rodi, W., and Scheuerer, G., 1985a, "Calculation of Laminar-Turbulent Boundary Layer Transition on Turbine Blades", Proceedings of the 65th AGARD - PEP Symposium on Heat Transfer and Cooling in Gas Turbines, Bergen, Norway, pp. 18-1 to 8-12.

Rodi, W., and Scheuerer, G., 1985b, "Calculation of Heat Transfer to Convection-Cooled Gas Turbine Blades", Journal of Engineering for Gas Turbines and Power, Vol., pp. 620 - 627.

Rued, K., and Wittig, S., 1985, "Free-Stream Turbulence and Pressure Gradient Effects on Heat Transfer and Boundary Layer Development on Highly Cooled Surfaces", Journal of Engineering for Gas Turbines and Power, Vol. 107, No. 1, pp. 54 - 59.

Saffman, P. G., 1970, "A Model for Inhomogeneous Turbulent Flows", Proceedings of the Royal Society, London, A317, pp.417.

Saffman, P. G. and Wilcox, D. C., April 1972, "Turbulence-Model Predictions for Turbulent Boundary Layers", AIAA Journal, Vol. 12, No. 4, pp. 541.

Schmidt, R. C., 1987, Two-Equation Low-Reynolds-Number Turbulence Modeling of Transitional Boundary Layer Flow Characteristic of Gas Turbine Blades, Ph.D. Thesis, University of Minnesota, Minnesota.

Schlichting, H., 1979, Boundary - Layer Theory, McGraw Hill, New York.

Sullivan, T. J., 1988, Simulating Transitional Flow and Heat Transfer Over Flat Plates and Circular Cylinders Using a k-ε Turbulence Model, MS Thesis, Cleveland State University.

Tani, I., 1969, "Boundary-Layer Transition", Annual Review of Fluid Mechanics, Vol. 1, pp. 169 - 196.

Tennekes, H. and Lumley, J. L., 1972, A First Course in Turbulence, The MIT Press, Cambridge.

Turner, A. B., 1971, "Local Heat Transfer Measurements on a Gas-Turbine Blade", Journal of Mechanical Engineering Science, Vol. 13, No. 1, pp. 1 - 12.

Wang, J. H., Jen, H. F., and Hartel, E. O., January 1985, "Airfoil Heat Transfer Calculation Using a Low Reynolds Number Version of a Two-Equation Turbulence Model", Journal of Engineering for Gas Turbines and Power, Vol. 107, pp. 60 - 67.

Wang, T., Simon, T. W., and Buddhavarapu, J., October 1985, "Heat Transfer and Fluid Mechanics Measurements in Transitional Boundary Layer Flows", Journal of Engineering for Gas Turbines and Power, Vol. 107, No. 4, pp. 1007 - 1015.

White, F. M., 1974, Viscous Fluid Flow, McGraw-Hill, New York.

Wilcox, D. C., February 1975, "Turbulence-Model Transition Predictions", AIAA Journal, Vol. 13, No. 2, pp. 241 - 243.

Wilcox, D. C., and Traci, R. M., July 1976, "A Complete Model of Turbulence", AIAA paper no. 76-351.

Wilcox, D. C., and Rubesin, M. W., 1980, "Progress in Turbulence Modeling for Complex Flow Fields Including Effects of Compressibility", NASA, TP 1517.

Wolfshtien, M., 1970, "On the Length-Scale of Turbulence Equation", Israel J. Technology, Vol. 8, pp. 87-99.

Zerkle, R. D. and Lounsbury, R. J., 1987, "Influence of Freestream Turbulence and Pressure Gradient on Heat Transfer to Gas Turbine Airfoils", AIAA paper 87 - 1917.

☆U.S. GOVERNMENT PRINTING OFFICE: 1990 - 748- 1 : 00226

NASA
National Aeronautics and Space Administration

Report Documentation Page

1. Report No.	2. Government Accession No.	3. Recipient's Catalog No.
NASA CR-185252		

4. Title and Subtitle

An Investigation into the Numerical Prediction of Boundary Layer Transition Using the K.Y. Chien Turbulence Model

5. Report Date

June 1990

6. Performing Organization Code

7. Author(s)

Craig A. Stephens and Michael E. Crawford

8. Performing Organization Report No.

89-3

10. Work Unit No.

505-62-21

9. Performing Organization Name and Address

The University of Texas at Austin
Mechanical Engineering Department
Austin, Texas 78712

11. Contract or Grant No.

NAG3-864

13. Type of Report and Period Covered

Contractor Report
Final

12. Sponsoring Agency Name and Address

National Aeronautics and Space Administration
Lewis Research Center
Cleveland, Ohio 44135-3191

14. Sponsoring Agency Code

15. Supplementary Notes

Project Manager, Frederick Simon, Internal Fluid Mechanics Division, NASA Lewis Research Center.

16. Abstract

The objective of this research was to assess the simulation capabilities of transition models developed at the University of Minnesota, as applied to the Launder-Sharma and Lam-Bremhorst two-equation turbulence models, and at The University of Texas at Austin, as applied to the K.Y. Chien two-equation turbulence model. In the course of this research, a major shortcoming in the use of the basic K.Y. Chien turbulence model for low-Reynolds number flows was identified. The problem with the Chien model involved premature start of "natural transition" and a "damped" response as the simulation moved to fully turbulent flow at the end of transition. This is in contrast to the other two-equation turbulence models at comparable freestream turbulence conditions. The "damping" of the transition response of the Chien turbulence model leads to an inaccurate estimate of the start and end of transition for freestream turbulence levels greater than 1.0% and to difficulty in calculating proper model constants for the transition model. The cause of the problem associated with the Chien turbulence model is linked to the form of the f_μ function. Specifying the f_μ function as only a function of y^+ leads to an increased production of TKE in the near-wall region of a laminar boundary layer, which in turn leads to an early start to transition. The resulting f_μ distribution also leads to a "damping" of the fully turbulent response. Thus, in the laminar and transition region of a developing boundary layer, the distribution of f_μ is not correct and will not be correct until the boundary layer becomes fully turbulent with the y^+ effect buried in the sublayer and log region.

17. Key Words (Suggested by Author(s))	18. Distribution Statement
By-pass transition Turbulence models Turbine blades	Unclassified – Unlimited Subject Category 34

19. Security Classif. (of this report)	20. Security Classif. (of this page)	21. No. of pages	22. Price*
Unclassified	Unclassified	190	A09

NASA FORM 1626 OCT 86

*For sale by the National Technical Information Service, Springfield, Virginia 22161